Paper 13

*Chapter appearing in the book*
*"Solid-State Photoemission and Related Methods: Theory and Experiment"*
*W. Schattke and M.A. Van Hove, Editors*
*Wiley-VCH Verlag, Berlin GmbH (2003), ISBN 3-527-40334-5*

# X. X-ray Optics, Standing Waves, and Interatomic Effects in Photoemission and X-ray Emission

**Charles S. Fadley[#@], See-Hun Yang[&], Bongjin Simon Mun [@%], J. Garcia de Abajo[+]**

---

**[#]Department of Physics, University of California Davis, Davis, CA 95616 USA**
**[@]Materials Sciences Division, Lawrence Berkeley National Laboratory, Berkeley CA 94720 USA**
**[&]IBM Almaden Research Center, San Jose, CA 95120 USA**
**[%]Advanced Light Source, Lawrence Berkeley National Laboratory, Berkeley, CA 94720 USA**
**[+]Centro Mixto CSIC-UPV/EHU, Aptdo. 1072, 20080 San Sebastian, Spain**

## X.1 Introduction

Optical effects in photoemission are discussed from a theoretical point of view elsewhere in this Handbook (Chapter 16, Section 16.8), but we here focus on the special case of soft x-rays in the energy range of approximately 200 eV to 1,500 eV incident on surfaces or other nanostructures so as to excite photoelectrons or secondary decay processes such as x-ray emission or x-ray inelastic scattering. The aim will be to consider ways in which these optical effects can be used at both non-resonant and resonant energies to more quantitatively probe surfaces, buried interfaces, and more complex nanoscale materials. We will begin with a brief review of the history of such studies, and then turn to recent examples of experimental results and theoretical simulations.

The theoretical calculations presented here will be mostly at the level of macroscopic optics, fundamentally based on the Fresnel equations as applied via a complex dielectric constant. However, at another extreme in discussing resonant interactions, a much more general and fully quantum mechanical picture will be used, with this one being reduceable to the first one in the limit of weak light-atom interaction, as is generally the case for soft x rays, even at resonant energies.

We begin by considering non-resonant effects; that is, where the x-ray energy is not close to any sort of core-level absorption edge in any of the atoms present in the sample. Then we consider resonant effects.

## X.2 Non-Resonant X-Ray Optical Effects in Photoemission

### X.2.1 Background and First Applications in the Total Reflection Geometry

The first discussions of x-ray optical effects on photoemission in the soft x-ray regime were by Henke [1]. In this seminal work, he pointed out that the penetration depths of x-rays in the 1 keV range are reduced to a few tens of Å when the incidence angle is lowered into the total

reflection regime. The complex index of refraction $n$ can be written as $n = \sqrt{\varepsilon} = 1 - \delta + i\beta$ [2] ,with $\varepsilon$ equal to the dielectric constant and $\delta$ and $\beta$ the small real and imaginary differences of $n$ from unity, both assumed in the soft x-ray regime to be <<1 in magnitude. In this description, the onset of significant reflectivity occurs at a critical incidence angle of $\theta_{inc}^{c} = \sqrt{2\delta}$ . Fig. 1 shows some of the results of this first study. In Fig. 1(a), the penetration depth, which we shall take to be the exponential decay length perpendicular to the surface, is shown for three x-ray energies in the soft x-ray regime as the incidence angle goes into the total reflection regime. It is clear that the penetration depths decrease to values comparable to, or even smaller than, the x-ray wavelength, and to typical photoelectron inelastic attenuation lengths, and this immediately suggests using total reflection geometries to enhance surface sensitivity in photoemission or other related spectroscopies excited by soft x-rays. Jumping to the present time, we note that calculations of such depths for non-resonant energies can be conveniently carried out with the aid of online computer programs [3]. Henke went beyond this to note that the combined effects of reflection and refraction at the surface caused an enhancement of photoelectron intensity as one enters the total reflection regime, as shown in Fig. 1(b). This enhancement could be quantitatively predicted from optical theory via the Fresnel equations and the experimental curve in fact used to determine the optical constants $\delta$ and $\beta$, as shown in Fig. 1(c).

This work stimulated immediate interest in using such surface enhancements to characterize overlayers, and Fig. 2 summarizes some of these early results due to Mehta and Fadley [4,5]. In Fig. 2(a), the sensitivity of the surface enhancement to even the small changes in photoelectron inelastic attenuation length from one kinetic energy to another are illustrated via the measurement of peak intensity ratios in photoemission from Au as the total reflection regime is approached. In Fig. 2(b), the ability to determine overlayer thicknesses is illustrated for an $SiO_2$ overlayer grown on a single-crystal Si substrate. Oscillatory scanned-angle x-ray photoelectron diffraction (XPD) effects are also evident in these data, due to photoelectron scattering in the substrate.

This work led sometime later to renewed interest in such effects as an adjunct in surface analytical studies, via work by Kawai and co-workers [6,7] and Chester and Jach [8,9]. In these studies, it was also pointed out that the concentration of x-ray flux near the surface for low incidence angles had the additional beneficial effect of significantly reducing the relative intensity of inelastically scattered electrons that underlies all photoelectron spectra. That is, since photoelectrons are preferentially created in a near-surface region of thickness comparable to their inelastic mean free paths, they will have less chance to inelastically scatter before escaping the surface. This effect is illustrated in Fig. 3 [10] for the case of a lightly oxidized Si surface. The overall benefits of being able to work in a total reflection geometry in laboratory XPS experiments has by now led to the availability of a commercial instrument specifically built for this purpose [10]. But beyond this, the inherently collimated nature of soft x-ray beams from any synchrotron radiation source and the ease with which most sample manipulators can vary the incidence angle through simple polar angle rotation make this type of experiment of obvious utility in many surface and interface studies.

### X.2.2 Standing Wave Effects for Probing Buried Interfaces and Nanostructures

It is well known that, as soon as any significant reflectivity occurs at a solid surface, a standing wave will be set up as an interference between the incident plane wave and the outgoing reflected plane wave. The fundamental process is illustrated in Fig. 4(a), together with some fundamental relationships between incidence angle (= reflected angle) and standing wave period. Such standing wave effects have been used for some time in the hard x-ray regime of about 10 keV for studying surface structures and overlayers [11,12,13]. Here, the standing wave formed by x-rays with wavelength of about 1 Å via Bragg reflection from various low-index planes can be

varied in position by rocking the incidence angle around the Bragg angle, thus yielding atomic positions with sub-Å accuracy [11,12], or by going into total reflection, a simple standing wave of the type indicated in Fig. 4(a), but of longer wavelength due to the small incidence angle may be established and used to determine distances above a surface [13].

We will here consider similar experiments with soft x-rays of approximately 10-60 Å (1-6 nm) in wavelength, as this is the range most relevant to exciting typical photoemission or soft x-ray emission/inelastic scattering spectra. In this case, the use of grazing angles below the critical angle is always possible, but the standing wave in this case will have a very long wavelength, since from Figs. 1(a) and 4(a) the relationship $\lambda_{SW} = \lambda_x / 2 sin\Theta_{inc}$ yields a standing wave period of roughly 3-10 times the x-ray wavelength, too large to probe on the nanometer scale that is most attractive. It has thus been proposed to use a synthetic multilayer mirror of suitable period to Bragg reflect soft x-rays so as to generate a strong standing wave with $\lambda_{SW}$ of a few nanometers, and then to utilize the standing wave profile above the surface in both photoemission [14,15,16,17] and x-ray absorption spectroscopy [18]. This type of reflection is illustrated in Fig. 4(b), from which it is clear that the standing wave period in first-order Bragg reflection is simply the periodicity of the multilayer $d_{ML}$. Present synthetic methods permit making such mirrors with periods down to about 3 nm, and with top-surface rms roughnesses of only 0.5 nm. Thus, they can be used as substrates of reasonably high quality on which to grow various types of samples for study. The multilayer mirror is in this context simply used as a standing wave generator (SWG).

Note also from Fig. 4(b) that, in the region of space above the surface in which the incident and reflected waves overlap and interfere to form the standing wave, the modulation strength of the standing wave goes roughly as the square root of the x-ray reflectivity $R_x$. Adding the incident and reflected waves in a more accurate mathematical way in fact shows that the maximum amplitude of the modulations in the standing wave should be $\pm 2\sqrt{R_x}$, or a full normalized modulation around a unit incident intensity of $4\sqrt{R_x}$. Thus, even a reflectivity of 5% can give a standing-wave modulation of something like 40%, provided the phase shift between incident and scattered waves is not too large (as is in fact found in realistic numerical calculations [19]). With the correct choice of materials, in particular one of lower electron density and x-ray scattering power (e.g. $B_4C$) and the other of higher density (e.g. W), 1st order Bragg reflection can thus yield x-ray reflectivities $R_x$ of 5-30% corresponding to standing wave modulation strengths of roughly 40-100% as measured relative to the incident wave, through the reasoning mentioned above.

Before considering some first experimental results of this type in photoemission, we briefly introduce the theoretical modeling of such non-resonant x-ray optical processes, as included in a computer program written by Yang [19]. The various ingredients necessary are illustrated in Fig. 5, here shown for a general multilayer system. Each layer is described by some index of refraction $n_i$. Interfaces can have graded dielectric properties, with single and multiple reflection and refractive transmission at each interface gradation being included. Once the optical calculation is taken to convergence, the squared strength of the electric field appropriate to the excitation of photoemission is calculated at each depth $z$. $|E(z)|^2$ is then used to modulate the appropriate product of atomic density and photoelectric subshell cross section and inelastic attenuation factor on passing to the surface, with the end result being both the distribution of photoelectron intensity as a function of depth, and the total intensity as well by integration over depth. Refraction of the photoelectrons on crossing the barrier of the inner potential is also included. The same program can also be used to calculate soft x-ray emission intensities as a function of depth, with the only difference being the final inclusion of a different attenuation length due to absorption.

Some results from these calculations for a $B_4C$/W multilayer [19] are shown in Fig. 6. Note the strong standing wave modulation for incidence at the Bragg angle, and the change in the depth distributions of C 1s and W 4f photoelectron intensities on going from the situation with no standing wave at the right to the Bragg condition at left. The C 1s emission has its maximum in the center of the first $B_4C$ layer with the standing wave, whereas it is a maximum at the surface without

the standing wave. The W 4f distribution shows the opposite effect, being compressed nearer the $B_4C$/W interface with the standing wave. These results thus qualitatively indicate the kind of depth distribution modification that can be affected by using a soft x-ray standing wave for excitation.

As a recent first example of the application of this approach, we consider a study by Yang et al. [16] and by Mun [17] of the buried interface between Fe and Cr, a prototypical pair of ferromagnetic and non-magnetic metals, respectively, that has been much studied in connection with the giant magnetoresistance (GMR) effect. The basic configuration of the experiment is shown in Fig. 7. The sample to be studied, an Fe/Cr bilayer, was grown on top of a multilayer mirror consisting of 40 periods of $B_4C$/W bilayers, with a period of 4 nm each. Thus, the standing wave above the multilayer will have a period also of 4 nm (cf. Fig. 4(b)). Beyond working with x-ray incidence angles near the first-order reflection of the $B_4C$/W multilayer mirror, the Cr layer underneath a constant-thickness Fe overlayer was grown in a wedge form. As one key part of the experimental procedure, the variation of the wedge thickness from 38 Å to 116 Å over a sample width along the x direction in Fig. 7 of about 10 mm, together with the small x-ray spot size of 0.2 mm, permitted carrying out the experiment for a range of positions of the standing wave with respect to the buried interface. That is, as the sample is scanned along x, the standing wave is effectively scanned vertically with respect to the interface, provided that the Fe/Cr bilayer does not influence the position of the standing wave. For a choice of photon energy that avoids any resonances in Fe or Cr, the desired "pinning" of the standing wave position by the multilayer mirror has been verified by direct calculations, as illustrated in Fig. 8. Even though the reflectivity is attenuated from about 9% to about 4% over the wedge, the Bragg position remains very constant at 11.15°, and this change in reflectivity would only change the estimated standing wave modulation (via the $4\sqrt{R}_x$ estimate mentioned above) from about 60% to about 40%.

As in prior standing wave studies, it is also possible in such SWG+wedge experiments to scan the incidence angle around the Bragg angle, which is well known to both vary the position of the standing wave and to reduce its amplitude for angles away from the Bragg angle [18]. This provides a second method for varying the position of the standing wave with respect to the interface, which, together with scanning the sample in *x* (cf. Fig. 7), should yield an overdetermined set of data that can be analyzed in terms of models for composition and magnetization variation through the interface. We illustrate this complementarity of measurement schemes for the Fe/Cr case in Fig. 9, where the Cr3p/Fe3p intensity ratio is shown as a function of both incidence angle for various choices of Cr thickness (Fig. 9(a)) and Cr thickness for various choices of incidence angle. These results have been analyzed in terms of the simple model shown at left in Fig. 10(a) and they lead to a determination of the onset of the Fe/Cr interface at 12.8 ± 2 Å depth and an overall interface mixing or roughness of 6.8 ± 2 Å in thickness. The center of the interface is thus measured in this way to be at 12.8 +3.4 = 16.2 Å, in excellent agreement with the 15 Å expected from the quartz crystal thickness monitor used to deposit this layer.

One can also measure magnetic circular dichroism for this Fe/Cr example by exciting core level Fe 2p and 3p and Cr 2p and 3p spectra with circularly polarized radiation. The nature of the MCD measurement means that ferromagnetic order will be detected only along the y direction in Fig. 7 that is nearly parallel to the light incidence direction due to the low Bragg angle of about 11º. Some of this data for 2p emission and two Cr thicknesses denoted Positions B (standing wave a maximum at the Fe/Cr interface) and C (standing wave a minimum at the interface) is shown in Fig. 11. The right-circular-polarized (RCP) and left-circular-polarized (LCP) spectra are shown for both Fe and Cr, together with the difference as the magnetic circular dichroism (MCD) in %. Although the Cr dichroism is much smaller than that of Fe (a few % for Cr versus 10-15% for Fe) there is nonetheless clear evidence for some ferromagnetic ordering of Cr, even though it is normally not ordered in this way, but rather weakly antiferromagnetically ordered (with a transition temperature of 311 K near that at which these measurements were carried out), in which case the MCD should be zero.

The fact that the sign of the Cr dichroism is opposite to that of Fe also immediately indicates that the Cr ferromagnetic ordering induced by the Fe is opposite in direction to that of Fe, as qualitatively indicated in Fig. 10(a). It is also clear that varying the position of the standing wave (e.g. from Position B to Position C) affects the relative magnitudes of the MCD signal, with that of Fe increasing at C and that of Cr decreasing. Similar results were obtained for 3p emission from both Fe and Cr, and the overall experimental data are shown in Fig. 10(b), together with best-fit curves based on x-ray optical calculations in which the two parameters for each of the four sets of MCD data shown at right in Fig. 10(a) were varied. At right in Fig. 10(a) are also summarized the best-fit numbers, and it is interesting that the onset of reduction of the Fe ferromagnetism in approaching the interface occurs just where the Fe3p/Cr3p ratio analysis yields a reduction in the Fe atomic fraction. The Fe ferromagnetism also is found to go to zero at the point in the interface at which its atomic fraction drops to 0.5. The Cr by contrast shows its slight ferromagnetic ordering over only a narrow layer about one atomic layer in thickness, and about one atomic layer below the interface mixing region.

Further details concerning this standing wave study of the Fe/Cr interface can be found elsewhere [16,17].

Although these are at present the only published experimental data of their kind, they suggest some exciting future possibilities for selectively studying buried interfaces or other vertically heterogeneous nanostructures with photoemission or other soft x-ray excited spectroscopies such as soft x-ray emission. Soft x-ray emission (at least at non-resonant energies) has an advantage over photoemission in probing more deeply, thus being more sensitive to the standing wave modulation below the surface, and we return to consider it more specifically in a later section. Beyond studying multilayer structures of relevance to magnetism and semiconductor device technology, one can suggest looking at self-assembled monolayers or other nanocrystalline objects grown or somehow deposited on the top surface of a suitable SWG. Combining spectromicroscopy using soft x-rays, which at present yields two-dimensional in-plane information, with standing wave excitation by again growing the sample on an SWG, could yield information on the third dimension perpendicular to the sample surface plane, a topic to which we return below also.

## X.3 Resonant X-Ray Optical Effects and Multi-Atom Resonant Photoemission

### X.3.1 General Considerations

On passing through a core-level absorption edge or resonance, the absorption coefficient can increase dramatically, and this will be reflected also in the index of refraction via an increase in $\beta$ and concomitant changes in $\delta$ that are derivable via a Kramers-Kronig analysis [3(b)]. As an example of this, we show in Fig. 12 the variation of $\beta$ and $\delta$ which arise in crossing the Mn $L_{2,3}$ = Mn $2p_{1/2,3/2}$ absorption edges in MnO. Since x-ray absorption at the 2p resonances of the 3d transitions metals is much studied, especially in magnetism-related work with dichroism, this type of data is of high relevance. We can see that both $\beta$ and $\delta$ increase by at least an order of magnitude in crossing these resonances, although they are still in magnitude always much less than unity, and in fact do not exceed 1% in magnitude, a fact which we will use later in making some simplifications in the optical analysis.

What effect will such resonant phenomena have on photoemission or other soft x-ray excited spectroscopies? In order to calculate this for a homogeneous, semi-infinite solid, we first follow the x-ray optical analysis of Yang [19] and Kay et al. [20], and then discuss the same phenomena in terms of a microscopic theory of multi-atom resonant photoemission [20,21,22].

### X.3.2 Resonant X-Ray Optical Theory

The resonant x-ray optical (RXRO) approach proceeds via the same basic ideas illustrated for a multilayer system in Fig. 5, except that we simplify to the homogeneous, semi-infinite solid with index of refraction *n* and a sharp vacuum-solid interface. The effect of the resonance is assumed to influence only the local electric field *E* at some depth *z* below the surface of the sample, with the associated differential photoelectric cross section $d\sigma/d\Omega$ varying only slowly through the resonance, as described by the usual one-electron theory [23]. The variation of photoemission intensity with photon energy $I(h\nu)$ is then obtained by integrating over the coordinate *z* perpendicular to the surface the product of the electric field strength $|E(h\nu,z)|^2$ at depths *z* relevant for photoemission, the energy-dependent differential photoelectron cross section $d\sigma/d\Omega$ appropriate to the experimental geometry (which may also in the experimental data include the effects of photoelectron diffraction (PD) that result in modulations beyond the simple atomic cross section [24], as seen already in the scanned-angle data of Fig. 2(b)) and the kinetic-energy-dependent inelastic attenuation length for electrons $\Lambda_e$, as

$$I(h\nu) \propto \frac{d\sigma(\hat{E},h\nu)}{d\Omega} \int_0^\infty |\vec{E}(h\nu,z)|^2 \exp(-\frac{z}{\Lambda_e(E_{kin})\sin\theta_e'})dz\,, \qquad (1)$$

where $\hat{E}$ is a unit vector along $\vec{E}$ and accounts for the polarization dependence in the cross section, and we have not included factors of atomic density and the solid angle acceptance of the analyzer that will be constant over an energy scan. In scanning photon energy through a resonance, it is also possible that *scanned-energy* photoelectron diffraction effects will cause intensity modulations [24], and these we will in fact see below.

Via an analysis based on the Fresnel equations [19,20], it can finally be shown that the integral in Eq. (1) reduces to

$$I(h\nu) \propto \frac{d\sigma}{d\Omega}(\hat{E},h\nu)\frac{|t(h\nu)|^2}{\frac{Im\{4\pi n(h\nu)\sin\theta_{inc}'(h\nu)\}}{\lambda_x(h\nu)}+\frac{1}{\Lambda_e(E_{kin})\sin\theta_e'}}\,, \qquad (2)$$

where the quantity *t* for p-polarized radiation incident on a planar surface from vacuum with $n_v = 1$, and for a conducting or non-conducting, but non-magnetic, reflective medium, is given by

$$t \equiv \frac{2\sin\theta_{inc}}{\sin\theta_{inc}' + n_r \sin\theta_{inc}}\,, \qquad (3)$$

with $\theta_{inc}'$ equal to the complex angle of propagation below the surface, again measured relative to the surface, $\theta_e'$ the real angle of propagation of the electron below the surface before allowing for possible refraction effects in crossing the inner potential barrier $V_0$, and $\lambda_x$ the wavelength of the radiation. $\theta_{inc}'$ is further related to $\theta_{inc}$ via Snell's Law: $\cos\theta_{inc} = n_r\cos\theta_{inc}'$, with $\theta_{inc}$ real. Eqs. 2 and 3 are completely general formulas for calculating photoemission, with all dependences on energy explicitly indicated. Beyond optical constants such as those in Fig. 12, the only other inputs needed are radial matrix elements and phase shifts for calculating $d\sigma/d\Omega$ [23] and the electron inelastic attenuation length $\Lambda_e$, which we have evaluated for the O 1s photoelectrons leaving MnO using a well-established semi-empirical formula [25]. Henke [1] has carried out the same analysis using a somewhat different formalism, with simplifications going beyond the equivalents of Eqs. 2 and 3 that are reasonable in view of his dealing with non-resonant cases.

Fig. 13 now presents results from using Eqs. 2 and 3 for the case of MnO with the optical constants of Fig. 12. The assumed experimental geometry is indicated in Fig. 13(a). In Fig. 13(b), it is obvious that the penetration depth is drastically decreased on going through the Mn 2p absorption resonances. In fact, its maximum for an energy just at the Mn $2p_{3/2}$ resonance is only approximately 130 Å for normal incidence, as illustrated in more detail by the solid curve in Fig. 14(a). On going to lower angles of incidence comparable to or below the critical angle at the Mn $2p_{3/2}$ resonance of $\sqrt{2\delta} \approx 7°$, this decrease is even more dramatic, with x-ray penetration depths of

only about 20 Å that are comparable to electron inelastic attenuation lengths [25]. Thus, the surface sensitivity of any soft x-ray spectroscopic measurement can be significantly affected in passing over such resonances. For comparison, we also show as the dashed curve in Fig. 14(a) a calculation from the Berkeley Center for X-ray Optics (CXRO) web program [3(a)], which makes use of standard tabulations of the optical constants that do not fully include edge resonance effects [3(b)]. There is a dramatic difference between these two curves, making it clear that a proper allowance for the exact form of the absorption features is essential for properly estimating x-ray penetration depths. As a test of the accuracy of our calculation method, we compare our results off-resonance with those from the CXRO program off-resonance, and with the same optical constants, and the two curves are identical. Fig. 13(d) also shows that reflectivity is significantly enhanced on passing through these resonances, which from our previous discussion of course also implies an enhanced standing wave above the surface.

More interestingly from a spectroscopic point of view is the variation of the O 1s intensity on passing through these resonances, which is shown in Fig. 13(c). These calculations predict strong variations of photoelectron intensity as the x-ray incidence angle is decreased toward the total reflection regime, but which nonetheless persist to some degree up to incidence angles of 30-40° with respect to the surface. Such effects have in fact been observed for MnO, as illustrated in Fig. 15(a) and 15(b). Fig. 15(a) first shows a broad scan of the O 1s intensity over an energy region including the Mn 2p resonances, for an incidence angle of 20°. The most obvious feature here is a strong modulation of the intensity due to scanned-energy photoelectron diffraction effects [24], but on top of this at the position of the strongest $2p_{3/2}$ resonance at 640 eV is a modulation that is about 25% of the overall PD effect. Fig. 15(b) shows similar data at an incidence angle of 10° and over a narrower energy window, and the resonance effects, measured as the overall + and - excursion are now considerably larger, being for example about 25% of the intensity just below the resonance, which has been set equal to unity in both Figs. 15(a) and 15(b). This marked increase is consistent with Fig. 13(c) in that the effects seen there also increase strongly on going to lower incidence angles, and we note that the 10° of Fig. 15(b) is furthermore not too far from the previously-estimated critical angle on the Mn $2p_{3/2}$ resonance of 7°. Also shown in Fig. 15(b) are the results of an x-ray optical calculation based on Eqs. 2 and 3 and, if allowance is made for the general curve in the experimental data due to PD effects, there is in general excellent agreement as to both the % effects (which have not been adjusted between experiment and theory) and the fine structure in the resonance-induced modulations for both the $2p_{3/2}$ and $2p_{1/2}$ features. Fig. 15(c) shows the variation of the overall excursion with incidence angle, and compares the experimental data points with XRO calculations. Again, there is in general excellent agreement, together with a prediction that there will be effects of at least a few % even for normal x-ray incidence. Finally, in Fig. 15(d) we show similar results for O 1s emission from a NiO(001) surface [26], but at an even lower 5° incidence angle, and here the experimental and theoretical curves are nearly identical, with both leading to a modulation of about 86%. These data in fact show that an earlier search for such resonant effects in NiO [27] was done at too high an incidence angle and with insufficient statistical accuracy to resolve them.

As a final comment on the systematics of effects such as those seen in Figs. 15(c) and 15(d), it has been pointed out by Kay et al. [20] that the modulation of photoelectron intensity has a form very similar to the optical constant $\delta$, and that, with certain simplifications reasonable in view of the small magnitudes of both $\delta$ and $\beta$, Eqs. 2 and 3 lead to a photoelectron intensity that is overall proportional to $1+\delta$, at least within the range of incidence angles under consideration here.

In summary up to this point, significant x-ray optical effects occur on passing through absorption resonances, especially for incidence angles close to the critical angle, but in fact also leading to a complex modulation of photoelectron intensities which in the low-incidence-angle limit are similar in form to the variation of $\delta$.

### X.3.3 An Alternative Viewpoint: Multiatom Resonant Photoemission (MARPE)

We now look at resonant effects from a different viewpoint, treating them in a more general way as interatomic multiatom resonant photoemission (MARPE) [20,21,22]. This viewpoint is thus different from normal resonant photoemission, which involves only orbitals on a single atom [28,29], and which can be termed single-atom resonant photoemission (SARPE) by comparison. This topic has also been introduced in Chap. 16 of this book (cf. Fig. 16.13), but we will amplify on it here.

The basic process envisioned is shown in Fig. 16(a). A single photon absorption process involves both direct excitation of a photoelectron from the atom at left and a resonant excitation via a strong bound-to-bound absorption resonance on the atom at right. If the absorption resonance were on the atom at left, we would have normal SARPE, but for the case shown if Fig. 16(a), the resonances can occur on various atoms around a given emitter, and hence this becomes both interatomic and multiatom. We will also implicity consider that both of the excited levels involved are core in character, although similar effects can in principle occur between more weakly bound electronic levels situated on two different atoms, as we discuss below.

The theory of MARPE has been explored in detail elsewhere [20,22], and for the case of O 1s emission from MnO dealt with in Figs. 13(c) and 15(a),(b),(c), the energy levels and basic matrix elements involved are as illustrated in Fig. 16(b). In brief summary, if the system is initially prepared in its many-body ground state $|g\rangle$, the contribution of the direct or unscattered wave function (that is, neglecting any sort of photoelectron diffraction effect) to the photoelectron intensity can be written

$$I(\vec{k}_e) \propto |\varphi_k^0(r)|^2 \propto \left| \sum_{l\mu} Y_{l\mu}(\hat{k}_e) i^l h_l^{(+)}(kr) M_{El\mu} \right|^2 , \qquad (4)$$

where $\vec{k}_e$ is the photoelectron wave vector, $\phi_{\mathbf{k}}^0(\mathbf{r})$ is the wave function at the detector, $Y_{l\mu}$ is a spherical harmonic, $\hat{k}_e$ is a unit vector along $\vec{k}_e$, $h_l^{(+)}(kr)$ is a spherical Hankel function, and

$$M_{El\mu} = \langle El\mu, \underline{O1s}| \; T \; |g\rangle \qquad (5)$$

is the matrix element describing the transition to the final state with a photoelectron $|El\mu\rangle$ of energy $E = \hbar^2 k^2 / 2m$ and an O 1s hole. Final-state photoelectron diffraction effects can also be incorporated in this model by using $M_{El\mu}$ as input for self-consistent multiple-electron-scattering equations. If we keep only terms up to second order in in the perturbing potential $V$ that is involved in $T$, it reduces to the well-known Kramers-Heisenberg formula for resonant photoemission [28,29]

$$T = V_{rad}^0 + \sum_{j,m} V_{AI}^j \frac{|m,j\rangle\langle m,j|}{\hbar\omega + E_g - E_m + i\Gamma_m/2} V_{rad}^j , \qquad (6)$$

where $V_{rad}^0$ is the interaction of the radiation with the emitter, $V_{\mathrm{rad}}^j$ is the interaction with the resonating atom $j$, $V_{\mathrm{AI}}^j$ is the autoionizing Coulomb interaction (cf. Fig. 16(b)) between the emitter and atom $j$, $E_g$ is the ground state energy, and the sums are over both Mn atoms $j$ and their intermediate many-body states $|m,j\rangle$ of energy $E_m$ and width $\Gamma_m$. A fully general theory of MARPE should also include exchange effects in the matrix elements above, but we expect them to be negligible for the cases we are treating. There is also a formal connection between MARPE and interatomic Auger electron emission, since the same sorts of matrix elements are embedded in the expressions describing both. However, the overall processes are fundamentally different, since the interatomic Auger process can be viewed as a two-step phenomenon: creation of the initial hole on

a neighbor atom, and then decay of this hole so as to eject an electron from the central atom. A related process is interatomic excitation transfer following the formation of an inner valence hole (compared to a core hole in typical interatomic Auger or MARPE), as recently discussed by Cederbaum and co-workers for atomic and molecular clusters, referred to as interatomic coulomb decay (ICD) [30] and for which experimental evidence has recently been published [31].

We now note two special points that have been considered previously and which make the theory of MARPE in the soft x-ray regime different from other processes occurring at lower excitation energies:

--the shorter wavelengths for soft x-ray excitation imply that retardation effects must be considered in the interaction with the external radiation and in the autoionization interaction, and

--the interatomic autoionization interaction must be generalized to the fully-relativistic Møller formula used previously in high-energy Auger theory [32].

In particular, retardation and relativistic effects lead to a dependence of the interatomic interaction on interatomic distance $r_{12}$ as $k^2/r_{12}$ (see Eq. (15.8) below). Here $k$ is the momentum of the exchanged photon (dotted orange line in Fig. 15.16), which is sufficiently large in core-level MARPE to make this leading term significant (actually, it is dominant at large separations in the MnO example discussed below). This is not the case in ICD [30,31], where the exchanged photon energy is small, so that the leading term in the interactomic interaction is provided by the non-retarded dipole-dipole expression, which behaves like $1/r_{12}^3$. A similar behavior in interactomic interactions at low-energy transfers is known as the Forster effect [33]. The transfer rate in the Forster effect is ruled by the square of the interatomic interaction, and therefore, it has been observed to decay like $1/r_{12}^6$ [33b]. A more detailed discussion of the differences between MARPE and the Forster effect appears elsewhere [34].

At the level of MARPE theory introduced here, the treatment should be capable of describing all many-electron interactions up to second order in the perturbation via Eq. (6), or up to arbitrary order via Eq. (5), including those for nearest-neighbors with the greatest overlap and thus enhanced many-electron interactions with the emitting atom.

The near-neighbor autoionization interaction can now be conveniently expanded in multipoles, and, with the further neglect of multipoles higher than dipoles, the effective interaction can be reduced to:

$$V_{AI}^{j} \approx e^2 r_1 r_2 \sum_{\mu_1\mu_2} F_{\mu_1\mu_2}^{R_j} Y_{1\mu_1}\left(\hat{r}_1\right) Y_{1\mu_2}^{*}\left(\hat{r}_2\right), \tag{7}$$

where

$$F_{\mu_1\mu_2}^{R} = \frac{-4\pi\, k^3}{3}\left[\frac{\delta_{\mu_1\mu_2}}{2\pi} h_0^{(+)}(kR) + h_2^{(+)}(kR)\; Y_{2\mu_2-\mu_1}\left(\hat{R}\right)\left\langle Y_{1\mu_2}\middle| Y_{2\mu_2-\mu_1} Y_{1\mu_1}\right\rangle\right] \tag{8}$$

and the bracket represents a Gaunt integral with standard normalization. Eq. (8) is actually the retarded dipole-dipole interaction, which is retrieved from the Møller formula [32] under the assumption that the relevant electronic states have a spatial extension much smaller than both the wavelength and the inter-atomic separation. This is fully justified for the Mn2p and O1s states of our case.

Putting these results into a single expression now yields

$$M_{El\mu} = A\left\langle E1\middle|r\middle|O1s\right\rangle\; \delta_{l,1}\sum_{\lambda}\varepsilon_{\lambda}^{eff}\left\langle Y_{1\mu}\middle| Y_{1\lambda}Y_{00}\right\rangle = A\left\langle E1\middle|r\middle|O1s\right\rangle\; \delta_{l,1}\,\varepsilon_{\mu}^{eff}\Big/\sqrt{4\pi}\,, \tag{9}$$

where $A$ is a light-intensity normalization constant,

$$\varepsilon_{\lambda}^{eff} = \varepsilon_{\lambda} - \sum_{\lambda'\mu_2} F_{\lambda\mu_2}\alpha_{\mu_2\lambda'}\varepsilon_{\lambda'} \tag{10}$$

is now the effective polarization vector that includes the effect of resonant x-ray scattering at the Mn sites, and the magnitude of the resonance is controlled by a product of a structure-factor type of sum over Mn sites

$$F_{\lambda\mu_2} = \sum_j F_{\lambda\mu_2}^{R_j} e^{ik_{inc}\cdot R_j}, \tag{11}$$

and the $Mn^{2+}$ polarizability tensor,

$$\alpha_{\mu_2\lambda'} = -\frac{4\pi e^2}{3} \sum_m \frac{\langle g | rY_{1\mu_2}^* | m \rangle \langle m | rY_{1\lambda'} | g \rangle}{\hbar\omega + E_g - E_m + i\Gamma_m/2}. \tag{12}$$

The form for the polarizability given here makes it clear that it is directly related to the usual description of resonant photoemission [29].

For the particular case of O 1s emission from MnO, this theoretical development predicts both the optical constants $\beta$ and $\delta$, and the O 1s intensity variation with reasonable accuracy, as seen in Figs. 12 and 15(b), respectively. It has furthermore been found by Garcia de Abajo et al. [20,22] that higher-order terms in the MARPE matrix elements, which can be considered to be multiple scattering of the radiation when resonantly scattered from one of the neighbors to the emitter, must be included in order to quantitatively describe these effects, as illustrated by two of the curves in Fig. 15(b). These higher-order contributions can be obtained by replacing epsilon in Eq. (15.10) by the self-consistent polarization vector derived from multiple scattering of the incoming photons at the Mn atoms of the crystal. The latter has been in turn derived from a layer-KKR description of photon scattering at the atomic planes parallel to the surface, yielding an equation similar to (15.10), but involving a dependence of the self-consistent polarization on atomic layer [20].

Although this quantum-mechanical treatment of MARPE effects is much more complex to deal with than the more macroscopic and empirically-linked resonant XRO picture, both have been shown to represent the same physical processes [20]. However, the proper MARPE theory outlined here obviously provides more insight into the nature of these interesting effects and it will also permit treating systems that go beyond what can be dealt with by RXRO, such as nanostructures localized in 1, 2, or 3 dimensions, or free molecules. We also note other treatments of such interatomic resonant photoemission processes, by Forster and later workers [33] and by Cederbaum et al. [30], with very low excitation energies assumed and by Fujikawa and Arai with direct relevance to the theoretical model discussed here [35].

As additional examples of experimental observations of related interatomic resonance effects in photoemission, we note that core-core MARPE effects analogous to those discussed here for MnO [20] and NiO [26,27] have also been seen in CuO [27]. Similar core-core MARPE effects have also been seen in adsorbates on metals, specifically O on Ni(001) [36] and $N_2$ on Ru(111) [37]; for these cases also, it appears that the RXRO approach provides at least a semi-quantitative description of the phenomena. In addition, a few other groups have reported the enhancement of valence photoemission intensities primarily associated with emission from a certain atom upon tuning the photon energy through more weakly bound core-level or inner-valence absorption edges of a nearby atom, with this work including measurements near solid-solid interfaces [38,39], on a free molecule [40] and on a free cluster, where the effect has been referred to as interatomic coulomb deday [31]. More recently, Guilleumin et al. appear to have seen core-core MARPE effects in free molecules through a more subtle avenue, specifically, the non-dipole parameter in a photoelectron angular distribution [41].

It is thus clear that such interatomic resonant effects will be seen in other systems in the future, and that they will not all be simply describable using an x-ray optical approach, which in any case does not provide a microscopic understanding of them. Effects going beyond a simple optical picture could provide interesting new information on the precise nature of x-ray interactions, including via the interatomic character, a method for uniquely identifying near-neighbor atoms in a complex sample, as originally proposed [21]. The microscopic theory outlined here, as well as other recent work [30,35] should provide a sound basis for understanding and using these phenomena in surface and interfaces studies, nanostructure characterization, and molecular

and cluster research. We also note the discussion of related optical effects in Chapter 16, Section 8 of this book, in which such phenomena are viewed in terms of screening and local fields.

## X.3 X-ray Optical Effects in X-Ray Emission and Resonant Inelastic Scattering

The two theoretical approaches outlined here, XRO calculations and microscopic MARPE theory, as well as the use of standing waves, can also be applied to soft x-ray emission (XES) and its close relative resonant inelastic x-ray scattering (RIXS), more bulk sensitive spectroscopic probes that are now coming into wider use [42] and which complement photoemission in the study of almost any system. As to bulk versus surface sensitivity, we point out again via Figs. 13(b) and 14(a) that, for the case of RIXS in which the incident energy is tuned to various points along an absorption curve like that in Fig. 12(a), the degree of bulk sensitivity may vary greatly from one energy to another.

The x-ray optical model can be simply modified to describe the overall intensity in such XES or RIXS experiments more quantitatively. For the case of a homogeneous flat surface, an emitted photon energy that is far from any resonance and with emission at an exit angle $\theta_{em}$ that is large enough to minimize refraction and reflection at the surface, this would involve replacing $\Lambda_e sin\theta_e^{'}$ with $\Lambda_{em} sin\theta_{em}' \approx \Lambda_{em} sin\theta_{em}$ in Eq. 2, with $\Lambda_{em}$ equal to the fluorescent x-ray attenuation length along path length or $\lambda_{em}/[4\pi\beta(h\nu_{em})]$ in obvious notation. With this replacement, Eq. 2 becomes

$$I(h\nu_{inc}, h\nu_{em}) \propto \left| M_{em}(\hat{E}, h\nu_{inc}, h\nu_{em}, \vec{k}_{em}) \right|^2 \frac{|t(h\nu_{inc})|^2}{\frac{Im\{4\pi n(h\nu_{inc}) sin\theta_{inc}^{'}(h\nu_{inc})\}}{\lambda_x(h\nu_{inc})} + \frac{1}{\Lambda_{em}(h\nu_{em}) sin\theta_{em}^{'}}} \qquad (13)$$

where the matrix element $M_{em}$ now allows for the precise x-ray transition involved, including the formation of the initial hole and subsequent decay processes, and $t$ is evaluated again from Eq. 3, still at the incident wavelength. Eq. 13 thus represents an accurate method for handling what essentially reduces to the well-known self-absorption effects in x-ray fluorescence that have been discussed previously in connection with MARPE [43,44]. In fact, viewed in this light, MARPE in x-ray emission can be viewed as having self absorption as a key ingredient, but perhaps via specific near-neighbor effects described in the microscopic theory, not necessarily the only ingredient. This connection has not been recognized in some prior papers on MARPE in x-ray emission [44]. The microscopic model could also be similarly extended to predict fluorescence intensities, but we will not present these details here.

From the point of view of using standing waves to probe buried interfaces (cf. Figs. 6-11), the greater penetration depths of soft x-rays as compared to photoelectrons represents a significant advantage, since the depth-dependent distribution of intensity will much more closely follow the the standing wave strength $\left|\vec{E}\right|^2$, permitting the study of deeper interfaces and a simpler analysis of the data. This is illustrated by comparing Fig. 6 for photoelectron emission and Fig. 17 for x-ray emission, both based on calculations using the methodology introduced in Fig. 5 [19]. Note that the depth profile of x-ray emission from each layer almost exactly follows the standing wave strength, and that deeper layers can be probed if desired. Future experiments of this type using the SWG+wedge method should thus be very interesting.

## X.4 Concluding Remarks and Future Directions

In conclusion, soft x-ray optical effects, whether at non-resonant or resonant energies, can strongly influence photoemission intensities. Among these effects are marked decreases in x-ray

penetration depth as the total reflection regime is approached, and significant decreases in the secondary electron background underlying photoemission spectra, both of which can be very useful for surface and interface studies. When incident energies are tuned to strong absorption resonances and the total reflection region is approached, these penetration depths can in fact be of the same magnitude as electron inelastic attenuation lengths, thus increasing surface sensitivity markedly.

There can also be significant negative and positive changes in intensity when the absorption edges of an atom neighboring the emitter are crossed, and this can be viewed as multiatom resonant photoemission (MARPE), with potential utility in identifying near-neighbor atoms in complex systems. Both x-ray optical theory and a microscopic theory of interatomic resonant photoemission have been succesfully used to describe these effects, which we expect to be observed in other systems beyond those discussed here in the future, including nanostructures, free molecules, and clusters.

The standing waves created due to reflection from a multilayer mirror can also be used to create a standing wave in the sample with period equal to the multilayer period, e.g. in the few-nanometer range. Photoemission excited by this standing wave can be used to non-destructively and selectively probe a buried interface, include magnetic order via circular dichroism. The multilayer mirror-plus-wedge sample technique discussed here should be applicable to a wide variety of studies of buried interfaces, including multilayer samples and other nanoscale objects that can be grown or deposited on top of a multilayer mirror. Future studies involving x-ray emission or inelastic scattering excited by such standing waves also look very promising. A final interesting potential application of such standing waves is in soft x-ray spectromicroscopy [45,46,47], which presently provides imaging only in the two dimensions lying in the sample surface plane, with some depth sensitivity in the third dimension perpendicular to the surface through element- and chemical state-specific x-ray absorption processes. Being able to work at sufficiently low angles of incidence in microscopes making use of secondary electrons and an electron optical system for imaging [45] or in an x-ray reflection, rather than transmission, geometry for another type of microscope making use of Fresnel zone plates for imaging [46,47], in combination with samples grown on a multilayer mirror, could add much more quantitative information on the perpendicular coordinate.

In summary, being able to thus "tailor" the radiation field in soft x-ray spectroscopic measurements should add considerably to the information derivable from photoemission and related techniques in the future.

## Figure captions:

Figure 1-- Results from the first study of non-resonant soft x-ray optical effects in photoemission by Henke. (a) The calculated variation of the exponential x-ray decay length (penetration depth) below the surface of Au for three different photon energies. (b) The variation in Au 4f photoelectron intensity as a function of x-ray incidence angle for a thick Au film deposited on glass. Note the increase in intensity in passing over the critical angle. (c) Comparison of experiment and x-ray optical theory for the intensity enhancement noted in (b). [From ref. 1.]

Figure 2-- Some first applications of non-resonant x-ray optical effects. (a) Observation of the difference in inelastic attenuation lengths for different core-level photoelectron peaks from Au through the dependence of intensity ratios as a function of x-ray incidence angle. The observed change in these intensity ratios is due to the fact that the x-ray penetration depth decreases to values comparable to the electron inelastic attenuation lengths. Two different choices of attenuation lengths are shown for the theoretical simulations to indicate the sensitivity of these ratios to this parameter. [From ref. 4.] (b) Observation of the change in the ratio of two chemically-shifted peaks from an oxidized

Si sample as x-ray incidence angle is decreased. Also evident are oscillatory scanned-angle photoelectron diffraction effects. [From ref. 5.]

Figure 3-- Reduction of inelastic background in XPS spectra with total reflection, from a slightly oxidized Si sample with a C-containing contaminant overlayer. [From ref. 10.]

Figure 4-- Basic geometry of standing wave formation. (a) General picture of standing wave formation, regardless of reflection type. (b) Standing wave formation in reflection from a multilayer mirror. Various key quantities and relationships are indicated in both panels.

Figure 5-- Calculation of x-ray optical effects on photoemission and soft x-ray emission. Various key ingredients are labelled. [From ref. 19.]

Figure 6-- X-ray optical calculations of standing wave effects on the depth distributions of electric field strength and photoelectron intensity from a multilayer mirror composed of alternating layers of $B_4C$ and W. The right panels show the depth distributions when the incidence angle is far from the multilayer Bragg angle, and the left panels the distributions at the Bragg angle. Note the strong standing wave created at the Bragg condition, and the influence on both the C 1s and W 4f depth distributions. [From ref. 19.]

Figure 7-- Basic geometry of an experiment combining soft x-ray excitation of photoemission with a wedge-shaped bilayer sample grown on a multilayer-mirror standing wave generator (SWG) so as to selectively study the buried interface between Fe and Cr. Scanning the sample position along the x axis effectively scans the standing wave through the interface. [From ref. 16.]

Figure 8-- Calculated reflectivity for the sample geometry of Fig. 7: a wedge-shaped Fe/Cr bilayer on top of a 40-period multilayer mirror composed of bilayers of $B_4C$ and W. Note that, although the reflectivity is attenuated by thicker Cr layers, the position of maximum reflectivity is pinned at the same angular position by reflection from the multilayer. [From refs. 16, 17, and 19.]

Figure 9-- Experimental results for the Cr3p/Fe3p intensity ratio from the sample of Fig. 7 as a function of both (a) x-ray incidence angles centered on the Bragg angle (rocking curves) and (b) the thickness of the Cr layer. These data can be analyzed to determine the composition variation through the interface, via the simple two-parameter linear model at left in Fig. 10(a) and x-ray optical calculations of photoemission intensities as outlined in Fig. 5 and accompanying text, with the solid curves in (a) and (b) representing the final best fits. [From ref. 16.]

Figure 10--Non-destructive depth-resolved determination of composition and magnetization profiles via standing-wave excited photoemission. (a) Sample geometry together with the models used to fit both the Cr3p/Fe3p intensity ratio of Fig. 9 (left side--linear model) and the Fe 2p and 3p and Cr 2p and 3p magnetic circular dichroism (MCD) data of Fig. 11 (right side--gaussian or half-gaussian models) are shown, together with the final best fits to the MCD data. Note that only two parameters are used in the x-ray optical calculations for each set of data: a position and a width, and that the five sets of data (Cr3p/Fe3p, Fe 2p MCD, Fe 3p MCD, Cr 2p MCD, and Cr 3p MCD) have been analyzed independently. (b) Summary of the Fe 2p and 3p and Cr 2p and 3p MCD data,

together with the best fits to experiment, and curves indicating how much the calculated curves change for 3 Å changes in the two parameters involved in each fit. [From ref. 16.]

Figure 11-- Magnetic circular dichroism measurements for Fe 2p and Cr 3p emission from the bilayer of Fig. 7, at two choices of Cr thickness that lead to having a standing wave maximum and a standing wave minimum at the buried interface (Positions B and C, respectively at left). [From ref. 16.]

Figure 12-- The optical constants $\beta$ and $\delta$ of MnO as the Mn 2p absorption resonances are crossed, The solid experimental curves were derived from an experimental determination of the absorption coefficient and subsequent Kramers-Kronig transformation of the results. Also shown are dashed theoretical curves based on the microscopic theory of multiatom resonant photoemission (MARPE). [From refs. 20 and 22.]

Figure 13-- Resonant x-ray optical calculation for the experimental geometry in (a) of: (b) the x-ray penetration depth = exponential decay length $\Lambda_x$, (c) the O 1s photoelectron intensity, and (d) the reflectivity $R_x$. These calculations were carried out for p-polarized radiation incident on a flat MnO surface and photon energies were scanned through the Mn 2p absorption resonances. The plots in (a), (b), and (c) are all shown as a function of both photon energy and incidence angle. [From ref. 19.]

Figure 14-- X-ray penetration depth in MnO as a function of incidence angle, for a photon energy (a) on the Mn $2p_{3/2}$ resonance of Fig. 12, and (b) below this resonance. The curve labelled CXRO is calculated using tabulated optical constants that do not allow for the full effect of the Mn $2p_{3/2}$ resonance [3(a)]. In (b), the two identical curves are from ref. 3(a) and this work, and used identical optical constants. [From refs. 3(a) and 19.]

Figure 15-- Resonant soft x-ray effects on O 1s emission from MnO and NiO on crossing the relevant transition-metal 2p absorption edges. (a) O 1s emission at a 10° exit angle from an MnO single crystal with (001) surface orientation, with photon energy scanned over a broad range which also reveals strong photoelectron diffraction (PD) effects. The dashed curve is as measured, and the solid curve is after correction for detector non-linearity. (b) As (a), but for a smaller energy range and with a 5° exit angle. Also shown are theoretical curves from the x-ray optical model and the microscopic MARPE theory with and without consideration of multiple scattering in the matrix elements. (c) The calculated variation of the overall ± excursion of the resonant effect in crossing the Mn $2p_{3/2}$ absorption edge as a function of x-ray incidence angle is compared to experimental data at four points. (d) As (b), but for O 1s emission from NiO(001) and with experiment corrected via the removal of a smooth PD curve and both curves renormalized to agree at the left and right ends. Note that the % variations in both experiment and theory have not been adjusted in any of the panels here. [From refs. 20 and 26.]

Figure 16----(a) Illustration of the basic process occurring in multiatom resonant photoemission (MARPE). (b) Additional diagram of the electronic transitions involved in the MARPE process, for the specific case of O 1s emission from MnO and with the photon energy passing over the Mn $2p_{3/2}$ absorption resonance. [After refs. 20 and 22.]

Figure 17-- X-ray optical calculations of standing wave effects on the depth distributions of electric field strength and soft x-ray emission intensity from an MnO thin-film sample grown on a multilayer $B_4C$/W mirror. The right panels show the depth distributions when the incidence angle is far from the multilayer Bragg angle, and the left panels the distributions at the Bragg angle. Note the strong standing wave created at the Bragg condition, and the influence on the O K$\alpha$, C K$\alpha$, and Fe L$\alpha$ x-ray depth distributions, whose intensity profiles with depth follow very closely the standing wave profile. To be compared with Fig. 6 for photoelectron emission. [From ref. 19.]

Acknowledgements and references:

This work was supported by the Director, Office of Science, Office of Basic Energy Sciences, Materials Science and Engineering Division, U.S. Department of Energy under Contract No. DE-AC03-76SF00098.

---

1 B.L. Henke, Phys. Rev. A 6, 94 (1972)

2 There are several conventions for the signs of $\delta$ and $\beta$, and we here use one that differs from that of Henke, which was $n = \sqrt{\varepsilon} = 1 - \delta - i\beta$ .

3 (a) One such program is that written by E.M. Gullikson, Center for X-Ray Optics, Lawrence Berkeley National Laboratory, and available at: http://www.cxro.lbl.gov/optical_constants/, with related input data compilations in published form at (b) B.L. Henke, E.M. Gullikson, and J.C. Davis. Atomic Data and Nuclear Data Tables 54, 181 (1993)

4 M. Mehta and C.S. Fadley, Physics Lett. 55A, 59 (1975)

5 M. Mehta and C.S. Fadley, Chem. Phys. Lett. 46, 225 (1977)

6 J. Kawai, M. Takami, M. Fujinami, Y. Hashiguchi, S. Hayakawa, Y. Gohshi, Spectrochim. Acta Part B 47, 983 (1992)

7 J. Kawai, S. Hayakawa, Y. Kitajima, and Y. Gohshi, Anal. Sci. 11, 519 (1995)

8 M.J. Chester and T. Jach, J. Vac. Sci. Technol. B 11,1609 (1993)

9 M.J. Chester and T. Jach, Phys. Rev. B 48, 17262 (1993)

10 Information on a commercial XPS system making use of total reflection is available under "XPS" at http://www.jeoleuro.com/

11 D.P. Woodruff, Prog. in Surf. Sci. 57, 1 (1998)

12 T. Jach and M.J. Bedzyk, Phys. Rev. B 42, 5399 (1990)

13 M.J. Bedzyk, D.H. Bilderback, G.M Bommarito, M. Caffrey, J.S. Schildkraut, Science 241, 1788, (1988)

14 K. Hayashi, S. Kawato, T. Horiuchi, K. Matsushige, Y. Kitajima, and Jun Kawai, Appl. Phys. Letters 68, 1921 (1996)

15 S.H. Yang, B.S. Mun, A.W. Kay, S-K. Kim, J.B. Kortright, J.H. Underwood, Z. Hussain, and C.S. Fadley, Surf. Sci. 461, L557 (2000)

16 S.H. Yang, B.S. Mun, N. Mannella, S-K. Kim, J.B. Kortright, J. Underwood, F. Salmassi, E. Arenholz, A. Young, Z. Hussain, M.A. Van Hove, and C.S. Fadley, J. Phys.-Cond. Matt. 14, L407 (2002)

17 B.S. Mun, Ph.D. thesis, University of California Davis, 2002.

18 S.K. Kim, J.B. Kortright, Phys. Rev. Lett. 86, 1347 (1999)

19 S-H. Yang, to be published.

20A.W. Kay, F.J. Garcia de Abajo, S.-H. Yang, E. Arenholz, B.S. Mun, N. Mannella, Z. Hussain, M.A. Van Hove, and C.S. Fadley, Phys. Rev. B 63, 115119 (2001)

21 A. Kay, E. Arenholz, S. Mun, J. Garcia de Abajo, C.S. Fadley, R. Denecke, Z. Hussain, and M.A. Van Hove, Science 281**,** 679 (1998)
22 F.J. Garcia de Abajo, C.S. Fadley, and M.A. Van Hove, Phys. Rev. Letters 82, 4126 (1999)
23 S. M. Goldberg, C. S. Fadley, and S. Kono, Solid State Commun. 28, 459 (1978); Y. Yeh and I. Lindau, At. and Nuc. Data Tables 32, 1 (1985)
24 C. S. Fadley in Synchrotron Radiation Research: Advances in Surface and Interface Science, R. Z. Bachrach, Ed. (Plenum Press, New York, 1992)
25 S. Tanuma, C.J. Powell, and D.R. Penn, Surf. and Interf. Anal. 35, 268 (2003)
26 N. Mannella et al., to be published, and N. Mannella, Ph.D. thesis, University of California Davis, 2003
27 M. Finazzi, G. Ghiringhelli, O. Tjernberg, L. Duo, A. Tagliaferri, P. Ohresser, and N.B. Brookes, Phys. Rev. B 62, R16215 (2000)
28 M. Grioni, P. Weibel, M. Hengsberger, and Y. Baer, J. Electron Spectrosc. 103, 713 (1999); S.L. Sorenson, and S. Svensson, J. Electron Spectrosc. 114:1, (2001)
29 A. Tanaka and T. Jo, J. Phys. Soc. Jpn. **63**, 2788 (1994)
30 L. S. Cederbaum, J. Zobeley, and F. Tarantelli, Phys. Rev. Lett. 79, 4778 (1997); R. Santra , J. Zobeley , L.S. Cederbaum , F. Tarantelli, Journal of Electron Spectroscopy and Related Phenomena 114–116, 41 (2001); R. Santra, J. Zobeley, and L. S. Cederbaum, Phys. Rev. B 64, 245104 (2001)
31 S. Marburger, O. Kugeler, U. Hergenhahn, and T. Moller, Phys. Rev. Letters 90, 203401 (2003)
32 J. P. Desclaux, in *Relativistic Effects in Atoms, Molecules, and Solids*, edited by G. L. Malli ( Plenum Press, New York, 1981) pp. 115–143
33 (a) T. Forster, Naturwissenschaften 6, 166 (1946); Ann. Phys. (Leipzig) 2, 55 (1948); (b) L. Stryer and R. P. Haugland, Proc. Natl. Acad. Sci. USA 58, 719 (1967)
34 C.S. Fadley, E. Arenholz, A.W. Kay, J. Garcia de Abajo, B.S. Mun, S.-H. Yang, Z. Hussain, and M.A. Van Hove, in X-ray and Inner Shell Processes, AIP Conference Proceedings No. 506. R.W. Dunford et al., Eds. (AIP, New York, 2000), p. 251.
35 T. Fujikawa and H. Arai, J. Electron Spectrosc. 123, 19 (2002).
36 D. Nordlund, M. G. Garnier, N. Witowsky, R. Denecke, A. Nilsson, M. Nagasono, N. Martensson, and A.Fohlisch, Phys. Rev. B 63, 121402 (2001)
37 P. Feulner, M. Ecker, P. Jakob, K. Kostov, R. Romberg, R. Weimar, and D. Menzel, S.-H. Yang, C.S. Fadley, R. Larciprete, S. Lizzit, A. Föhlisch, W. Wurth, to be published
38 K.L.I. Kobayashi, N. Watanabe, H. Nakashima, M. Kubota, H. Daimon, and Y. Murata, Phys. Rev. Lett. 52, 160 (1984)
39 P. Pervan, M. Milun, and D.P. Woodruff, Phys. Rev. Lett. 81, 4995 (1999)
40 Y.F. Hu, G.M. Bancroft, and K.H. Tan, Inorganic Chemistry 39, 1255-1264 (2000).
41. R. Guillemin, D. Rolles, S.W. Yu, A. Wolska, I. Tran, A. Hudson, J. Baker, O. Hemmers and D.W. Lindle, to be published.
42 J. Nordgren, Ed., special issue on soft x-ray emission spectroscopy, J. Electron Spectrosc. 110, nos. 1-3 (2000); E.Z. Kurmaev, A. Moewes, D.L. Ederer, X-Ray Spectrometry, 31, 219 (2002)
43 E. Arenholz, A.W. Kay, C.S. Fadley, M. Grush, T.A. Callcott, D.L. Ederer, C. Heske, and Z. Hussain, Phys. Rev. B 61, 7183 (2000)
44 A. Moewes, E.Z. Kurmaev, D.L. Ederer, T.A. Phys. Rev. B 62, 15427 (2000); A. Moewes and E. Kurmaev, Nucl. Inst. & Meth. in Phys. Res. A 467 (Pt. 2):1529 (2001)
45 A. Scholl, H. Ohldag, F. Nolting, J. Stohr, H.A. Padmore, Rev. Sci. Inst. 73, 1362 (2002)
46 G. Denbeaux, P. Fischer, G. Kusinski, M. Le Gros, A. Pearson, D. Attwood, IEEE Trans. on Magnetics 37, 2761 (2001)
47 A.P. Hitchcock, C. Morin, T. Tyliszczak, I.N. Koprinarov, H. Ikeura-Sekiguchi, Surf. Rev. and Lett. 9, 193 (2002)

1

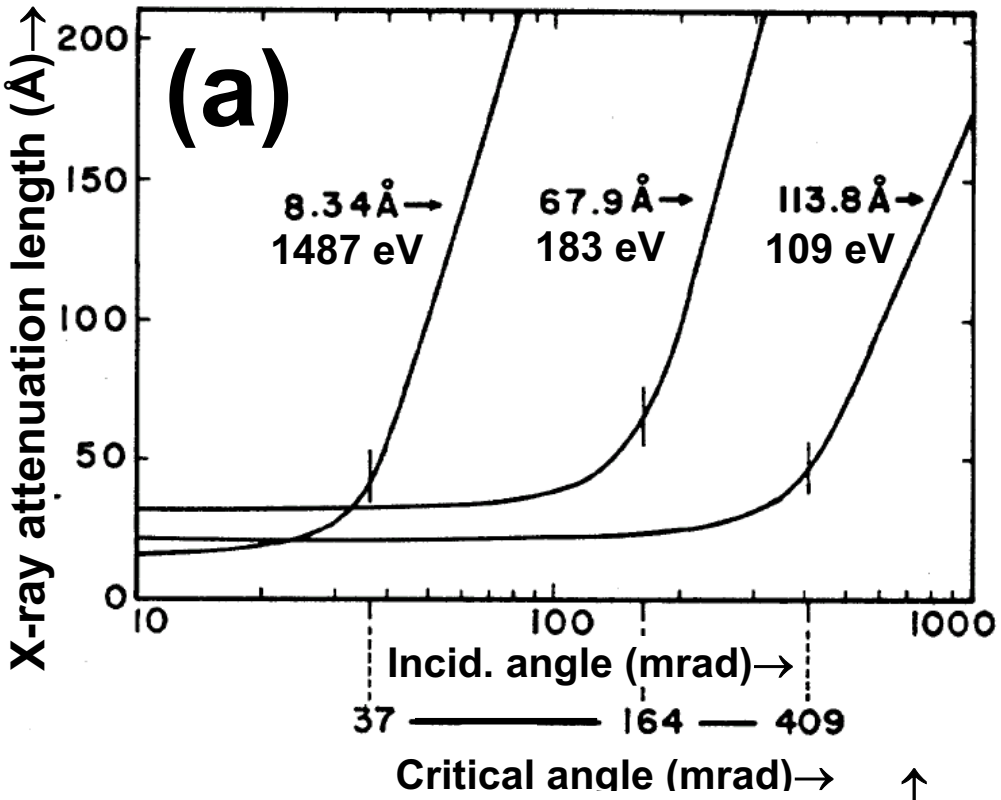
(a)
X-ray attenuation length (Å)→
200
150
100
50
0
8.34Å→
1487 eV
67.9Å→
183 eV
113.8Å→
109 eV
10
100
1000
Incid. angle (mrad)→
37
164
409
Critical angle (mrad)→

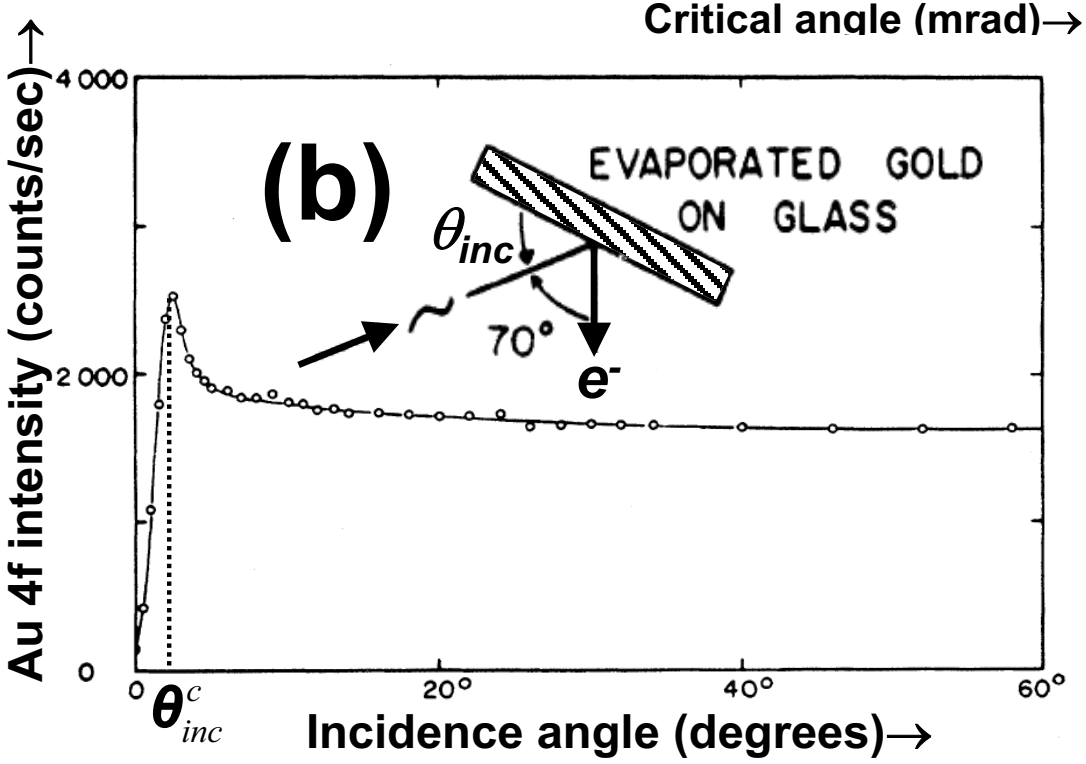
(b)
EVAPORATED GOLD
ON GLASS
θinc
70°
e-
Au 4f intensity (counts/sec)→
4 000
2 000
0
0
θc inc
20°
40°
60°
Incidence angle (degrees)→

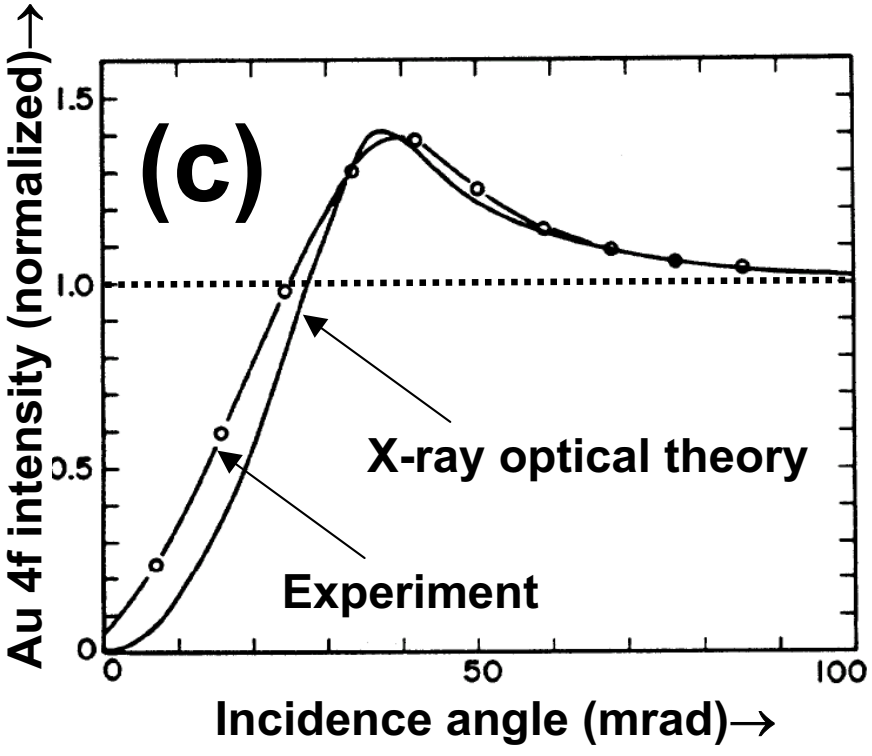
(c)
Au 4f intensity (normalized)→
1.5
1.0
0.5
0
X-ray optical theory
Experiment
0
50
100
Incidence angle (mrad)→

2

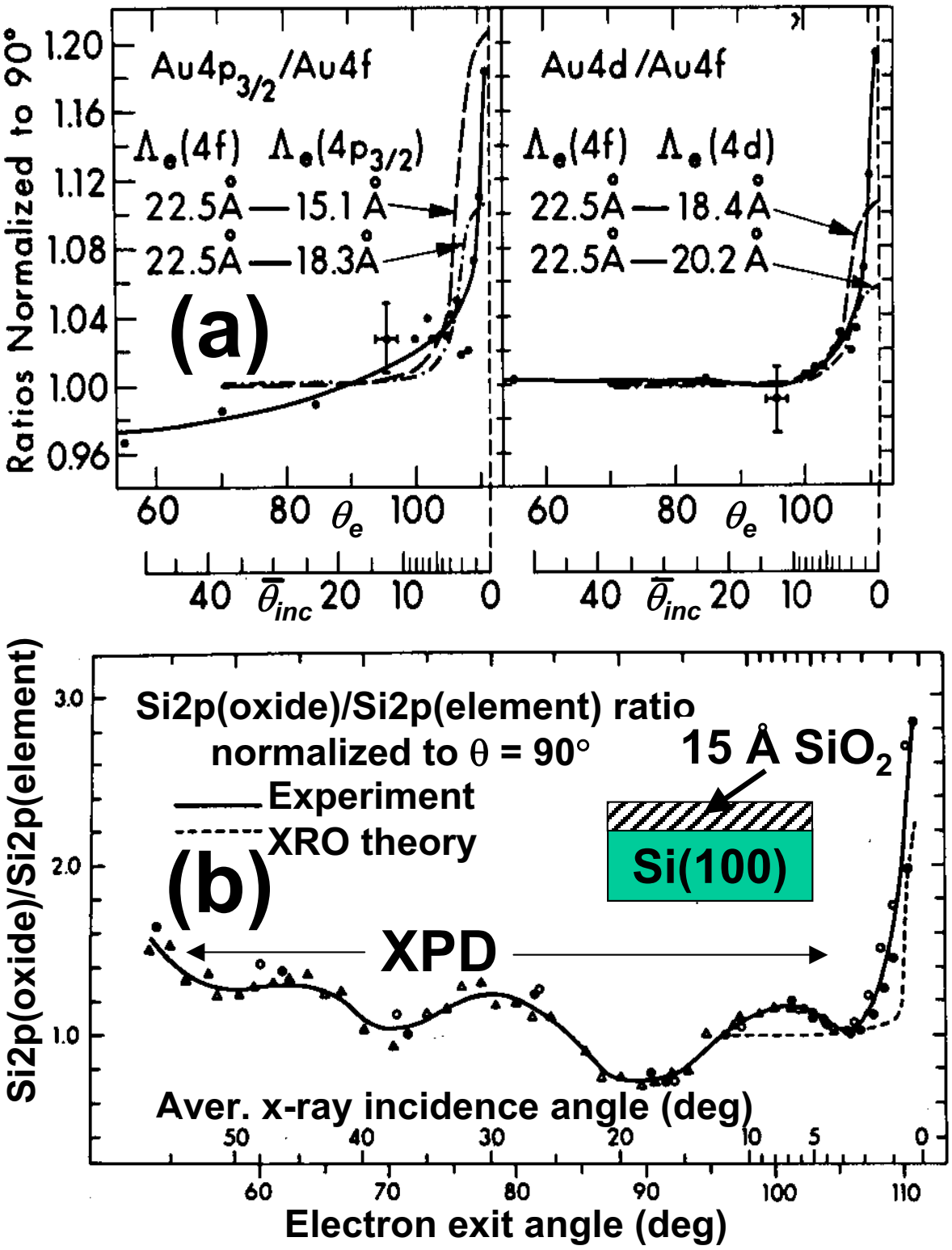
Au4p3/2/Au4f
Λe(4f) Λe(4p3/2)
22.5Å — 15.1 Å
22.5Å — 18.3Å
(a)
Au4d/Au4f
Λe(4f) Λe(4d)
22.5Å — 18.4Å
22.5Å — 20.2 Å
Ratios Normalized to 90°
1.20
1.16
1.12
1.08
1.04
1.00
0.96
60 80 θe 100
40 θinc 20 10 0
Si2p(oxide)/Si2p(element) ratio
normalized to θ = 90°
Experiment
XRO theory
(b)
15 Å SiO2
Si(100)
XPD
Aver. x-ray incidence angle (deg)
50 40 30 20 10 5 0
Si2p(oxide)/Si2p(element)
3.0
2.0
1.0
60 70 80 90 100 110
Electron exit angle (deg)

3

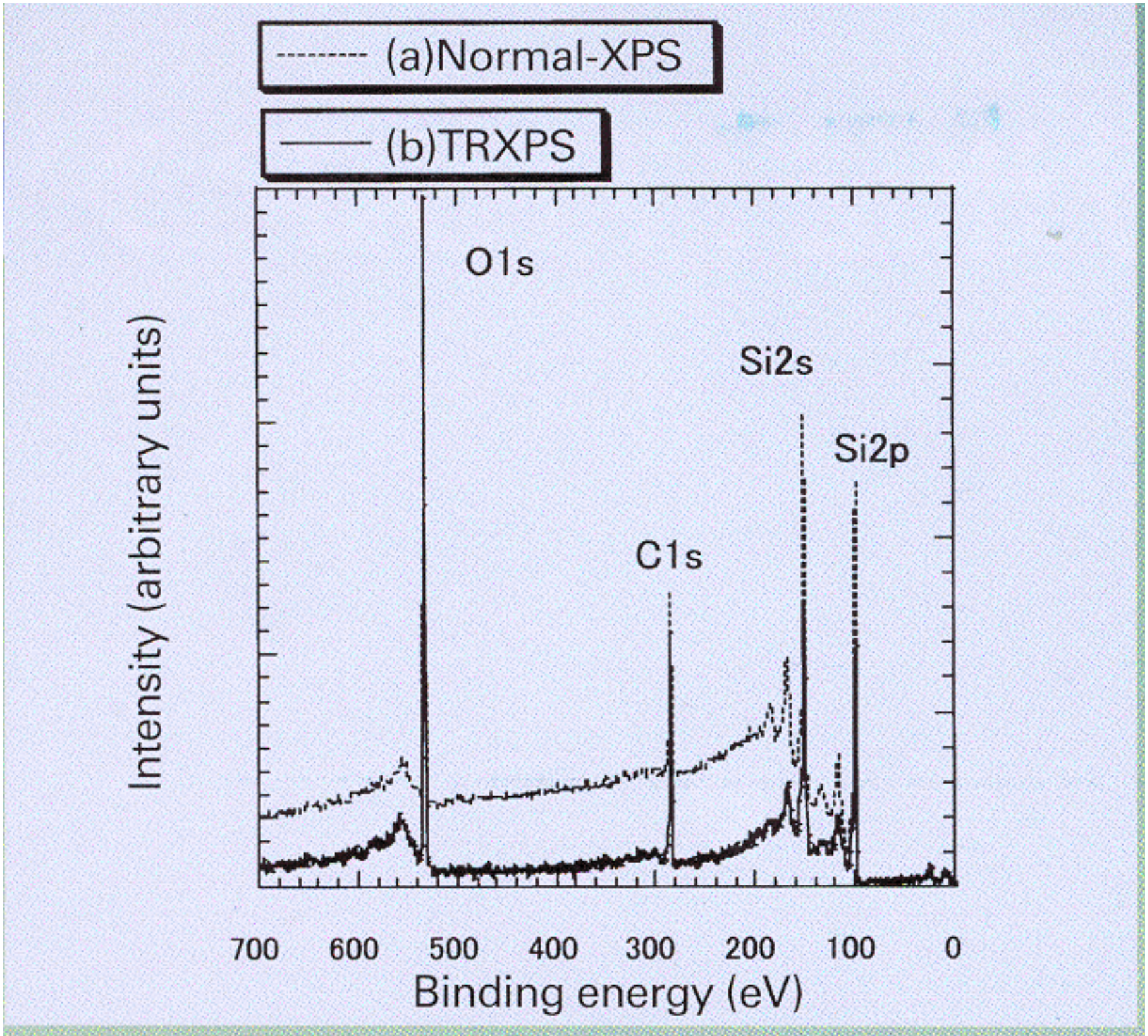
(a)Normal-XPS
(b)TRXPS
O1s
Si2s
Si2p
C1s
Intensity (arbitrary units)
700
600
500
400
300
200
100
0
Binding energy (eV)

# 4 Standing wave formation:

$I_{SW}(|E^2|) \propto |\phi_{inc} + \phi_{refl}|^2$
$= |\phi_{inc}|^2 + \underbrace{\phi_{inc}\phi_{refl}^* + \phi_{inc}^*\phi_{refl}}_{\text{SW modulation}}$
$+ |\phi_{refl}|^2$

(a)

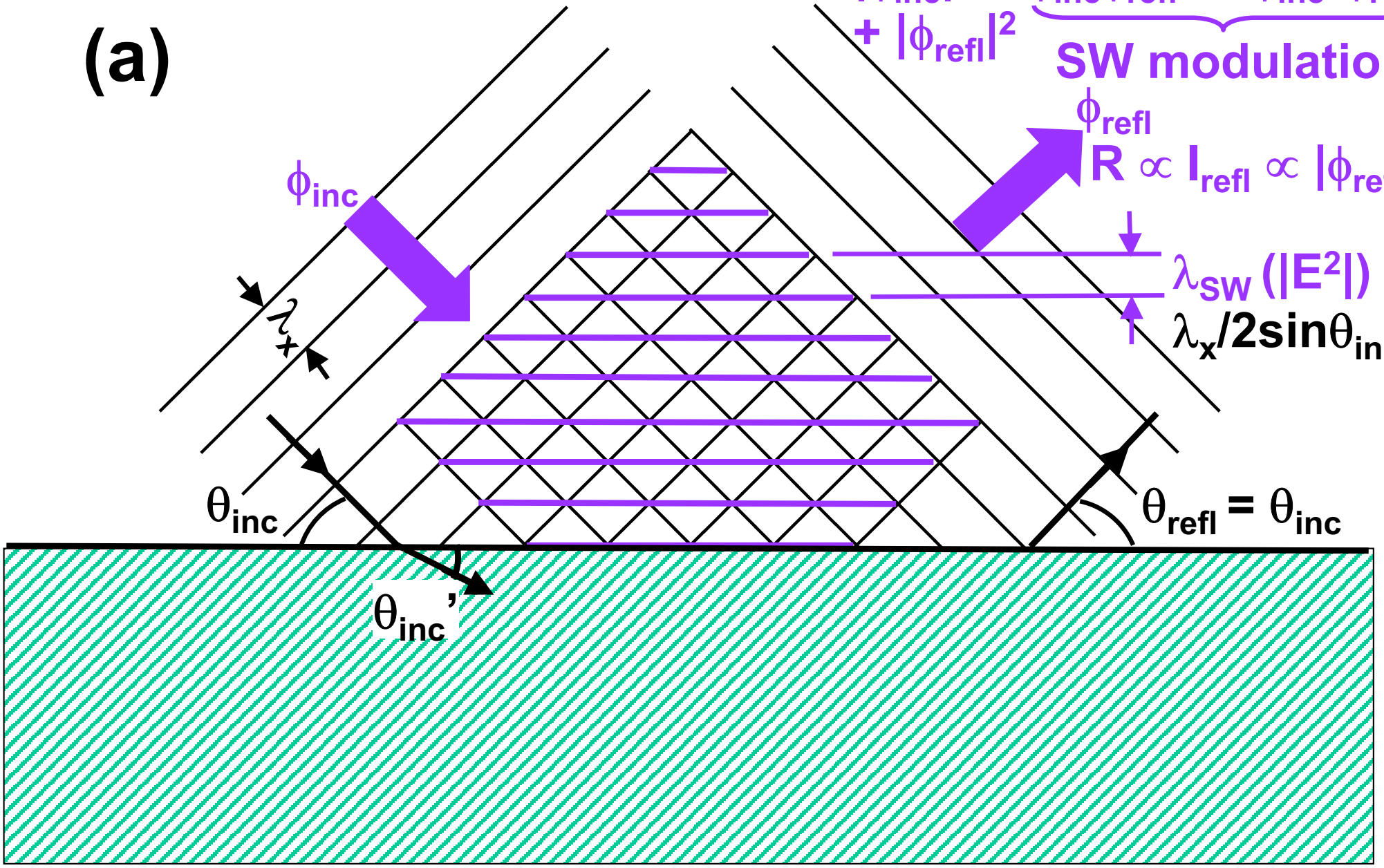

# Standing wave formation with a multilayer mirror:

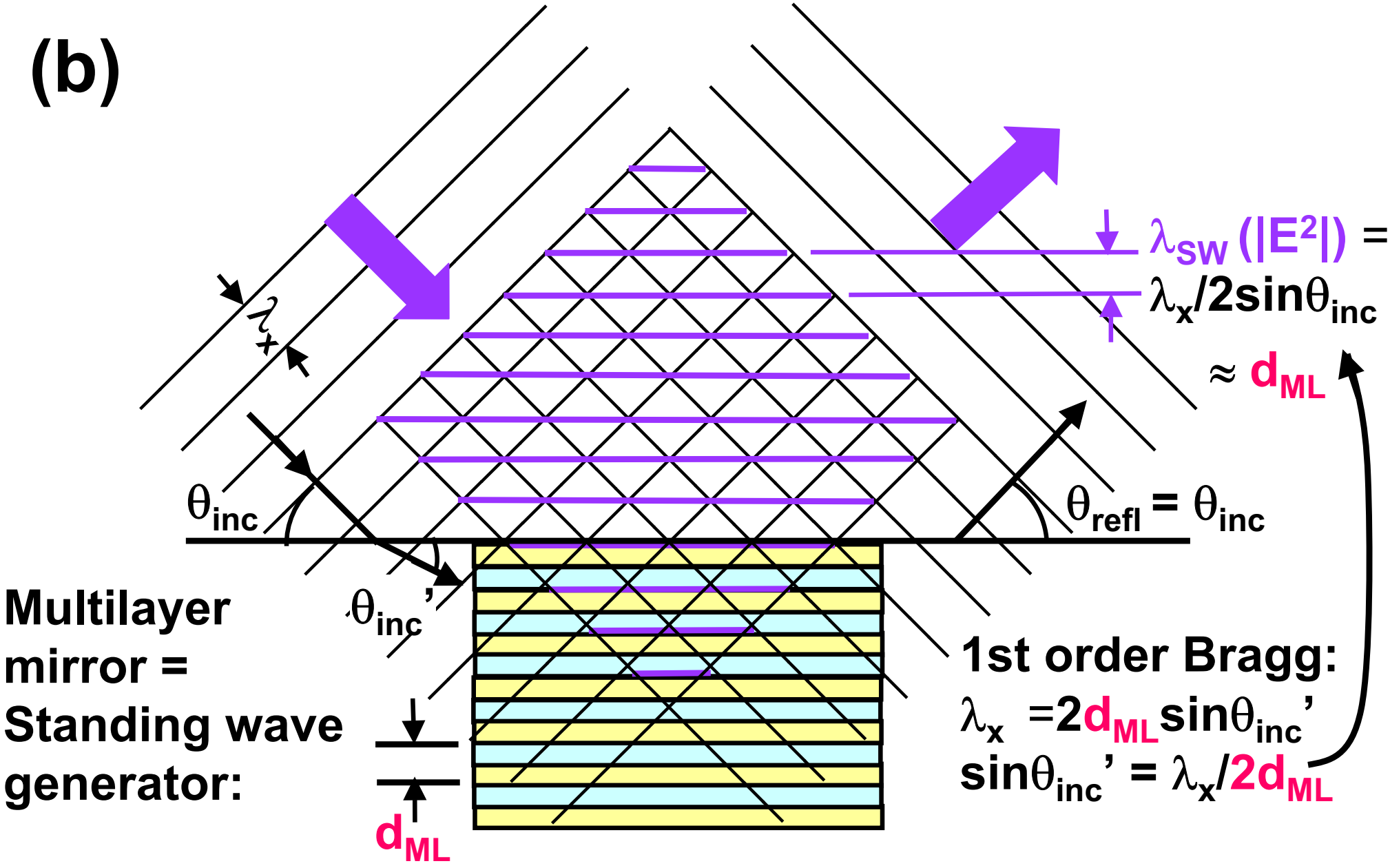

*X-ray Optical Calculations :*

# Calculating XRO effects on spectroscopy

- *n (hν) =*
  *1 -δ (hν) + iβ(hν)*

-*variable polarization*

-*multiple reflection/ refraction*

-*exact treatment of interlayer intermixing a/o roughness*

-*electric field at i-th layer:*

$$I_i(z) = |E_i^+(z) + E_i^-(z)|^2$$

***Photoemission:***

-differential cross section

-inelastic attenuation

-surface refraction

***X-ray emission:***

-fluorescence yield

-excitation matrix element

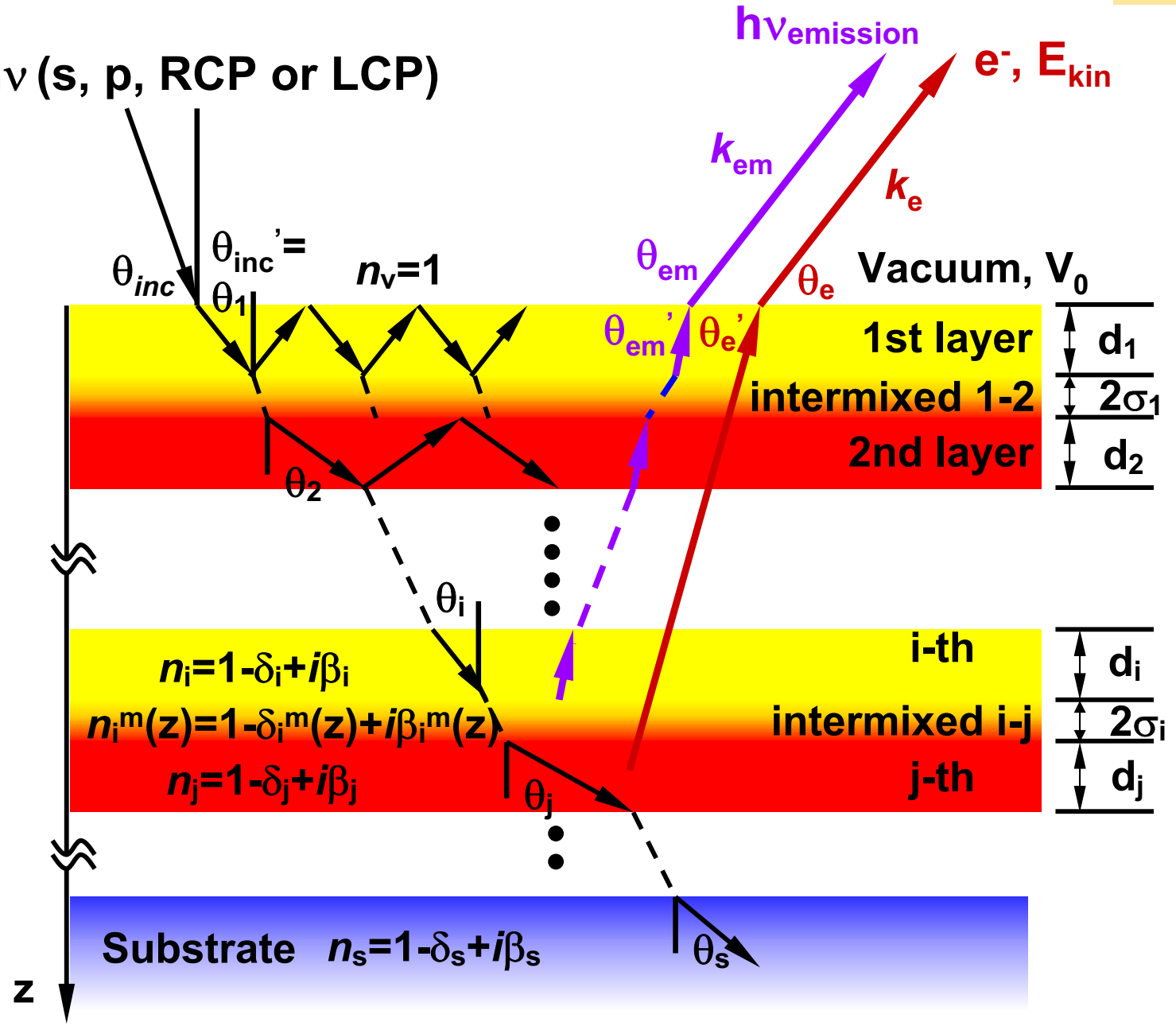

# CALCULATED PHOTOEMISSION FROM A MULTILAYER STANDING WAVE GENERATOR (SWG)-- $[B_4C\ (20\ Å)/W\ (20\ Å)]_{20}/Si$

6

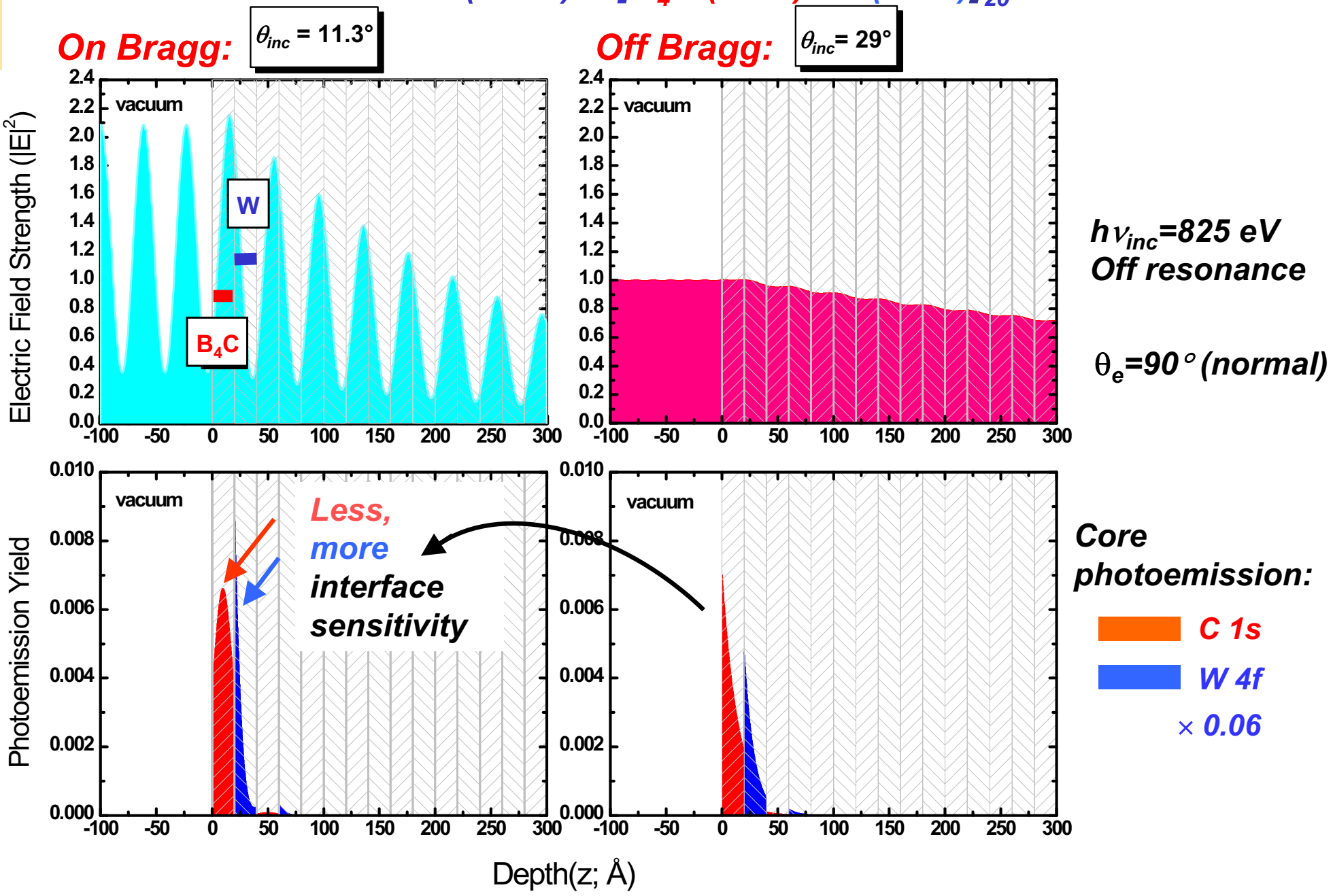

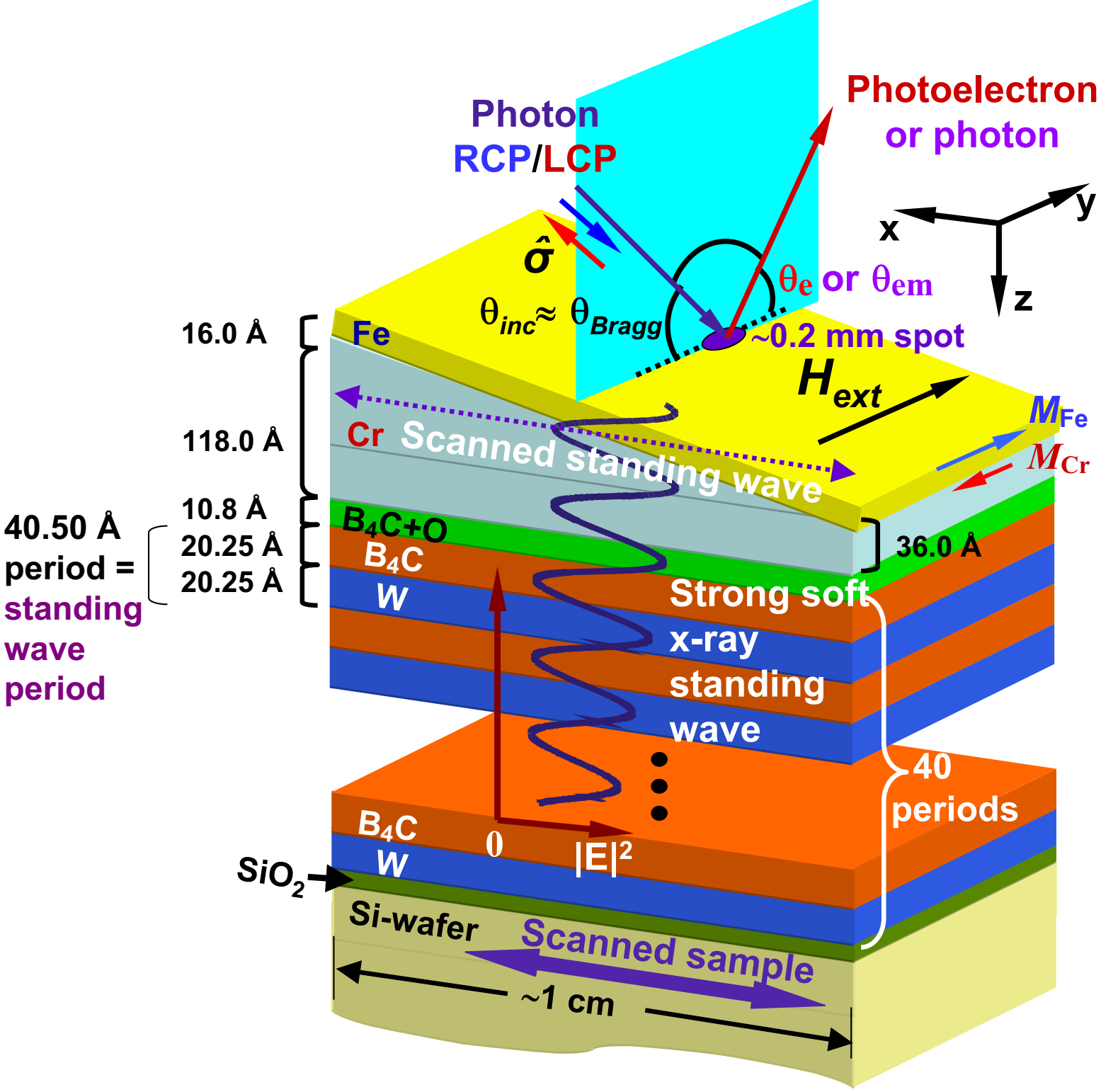
Photon
RCP/LCP
Photoelectron
or photon
x
y
z
$\hat{\sigma}$
$\theta_{inc} \approx \theta_{Bragg}$
$\theta_e$ or $\theta_{em}$
~0.2 mm spot
$H_{ext}$
$M_{Fe}$
$M_{Cr}$
16.0 Å
Fe
118.0 Å
Cr
Scanned standing wave
40.50 Å
period =
standing
wave
period
10.8 Å
20.25 Å
20.25 Å
$B_4C$+O
$B_4C$
W
36.0 Å
Strong soft
x-ray
standing
wave
40
periods
$B_4C$
W
0
$|E|^2$
$SiO_2$
Si-wafer
Scanned sample
~1 cm

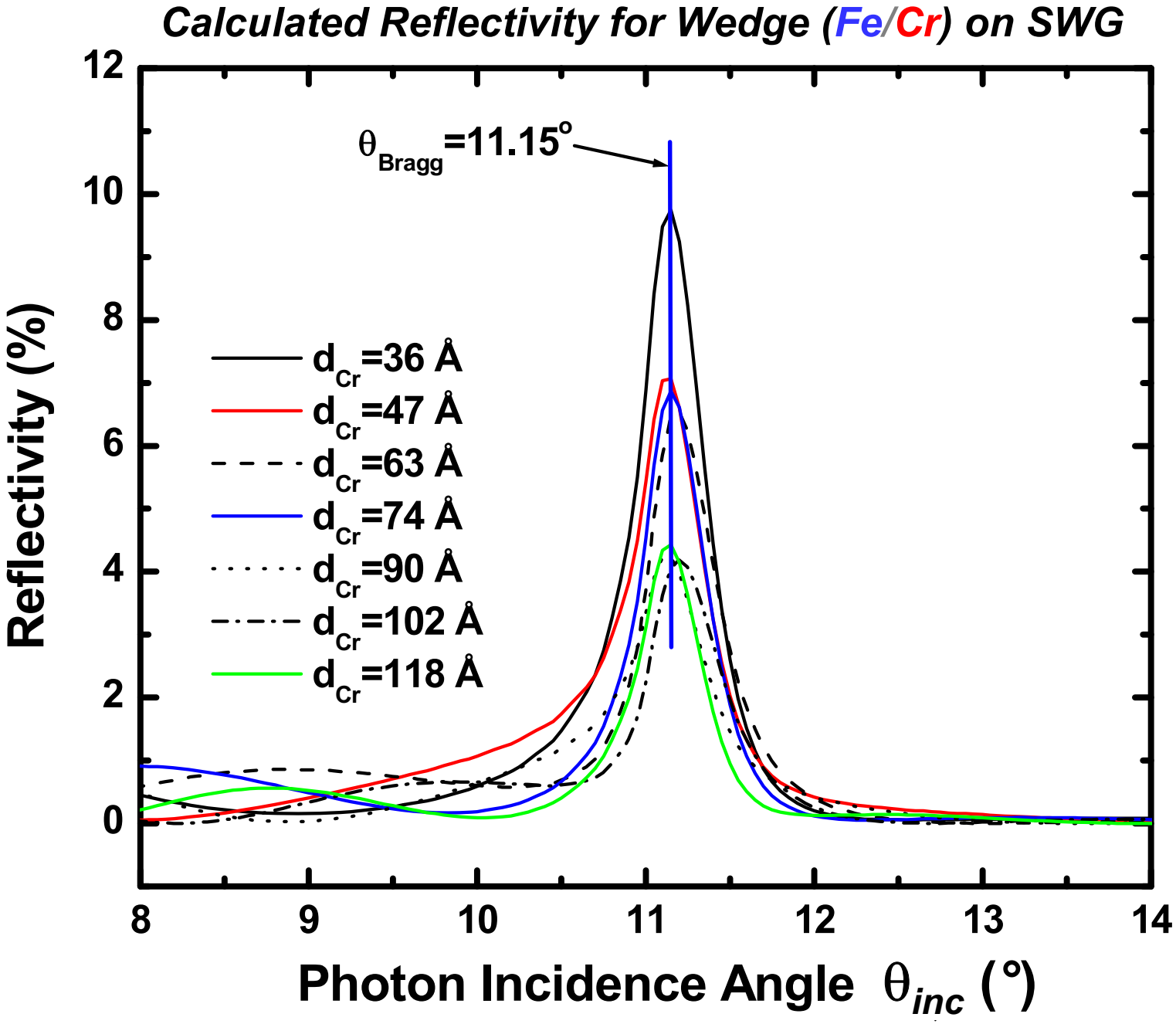
Calculated Reflectivity for Wedge (Fe/Cr) on SWG
θBragg=11.15°
dCr=36 Å
dCr=47 Å
dCr=63 Å
dCr=74 Å
dCr=90 Å
dCr=102 Å
dCr=118 Å
Reflectivity (%)
Photon Incidence Angle θinc (°)
0
2
4
6
8
10
12
8
9
10
11
12
13
14

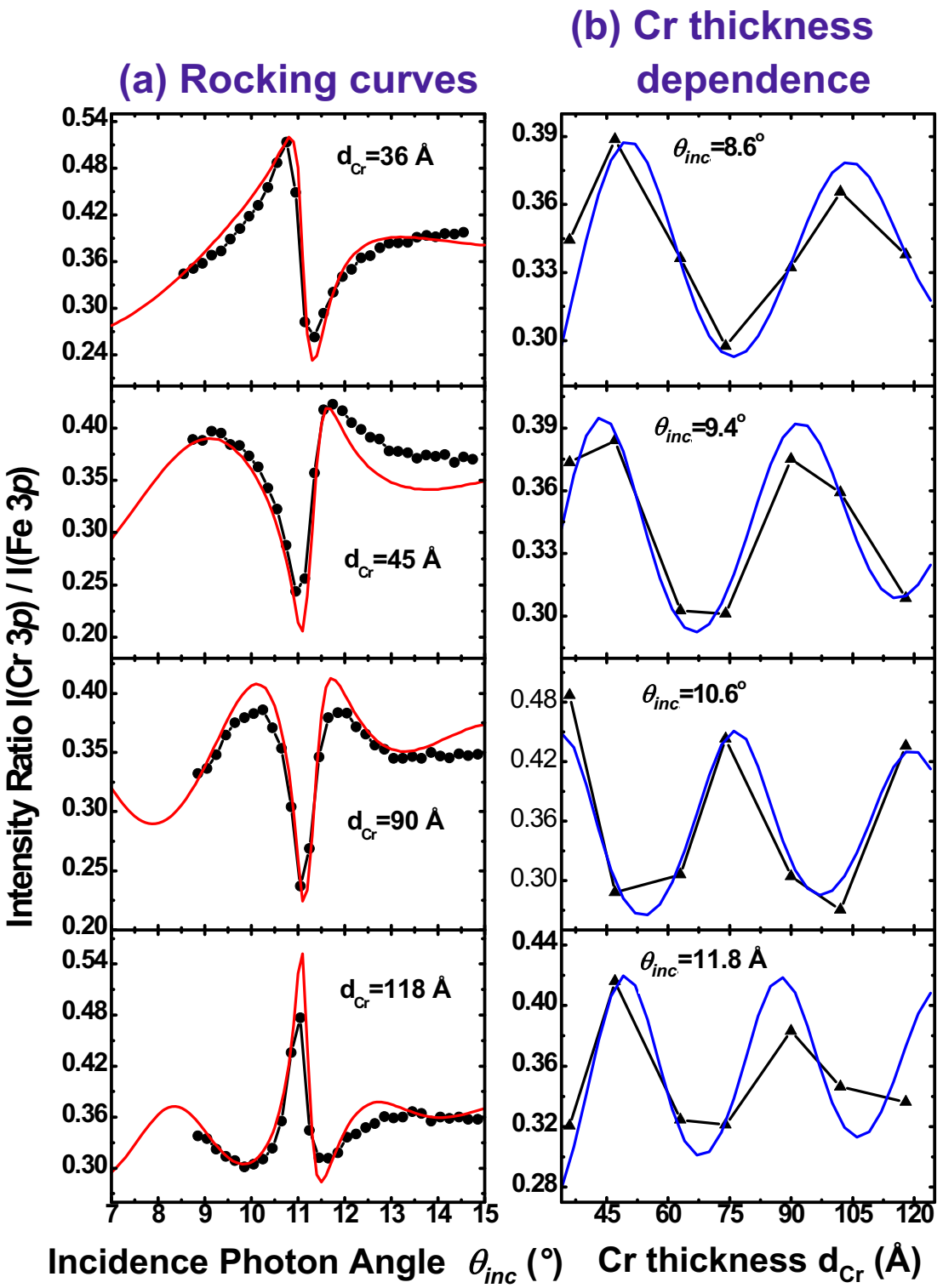
(a) Rocking curves
(b) Cr thickness dependence
Intensity Ratio I(Cr 3p) / I(Fe 3p)
d_Cr=36 Å
d_Cr=45 Å
d_Cr=90 Å
d_Cr=118 Å
θ_inc=8.6°
θ_inc=9.4°
θ_inc=10.6°
θ_inc=11.8 Å
Incidence Photon Angle θ_inc (°)
Cr thickness d_Cr (Å)

10

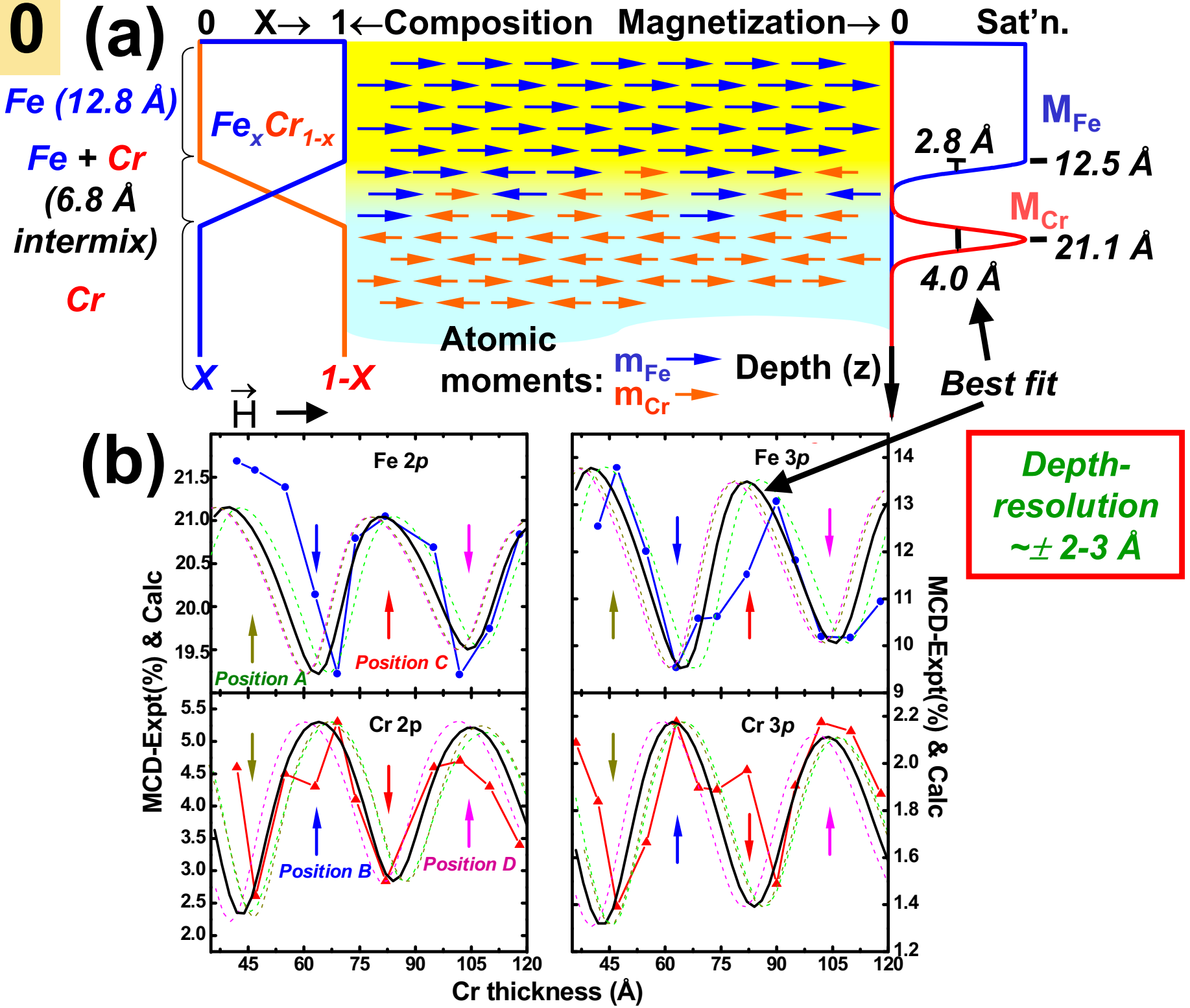
(a)
0 X→ 1←Composition Magnetization→ 0 Sat'n.
Fe (12.8 Å)
Fe + Cr
(6.8 Å
intermix)
Cr
$Fe_xCr_{1-x}$
X
1-X
$\vec{H}$
Atomic
moments:
$m_{Fe}$
$m_{Cr}$
Depth (z)
$M_{Fe}$
2.8 Å
12.5 Å
$M_{Cr}$
21.1 Å
4.0 Å
Best fit
(b)
Fe 2p
Fe 3p
Cr 2p
Cr 3p
Position A
Position B
Position C
Position D
MCD-Expt(%) & Calc
MCD-Expt(%) & Calc
Cr thickness (Å)
Depth-
resolution
~± 2-3 Å

## *Fe & Cr 2p MCD Data from wedge (Fe/Cr)+SWG*

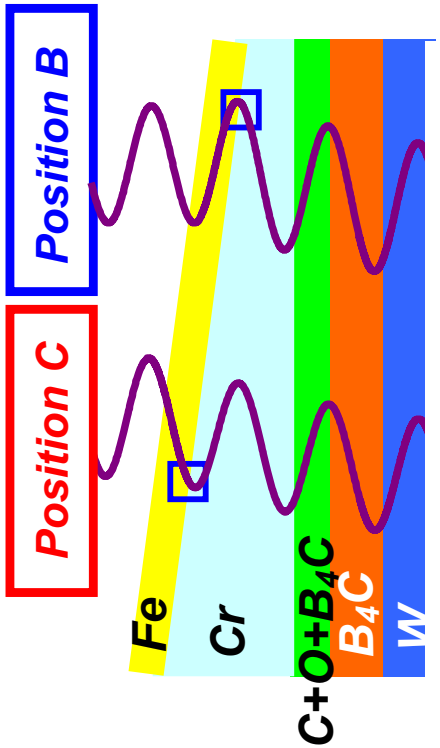


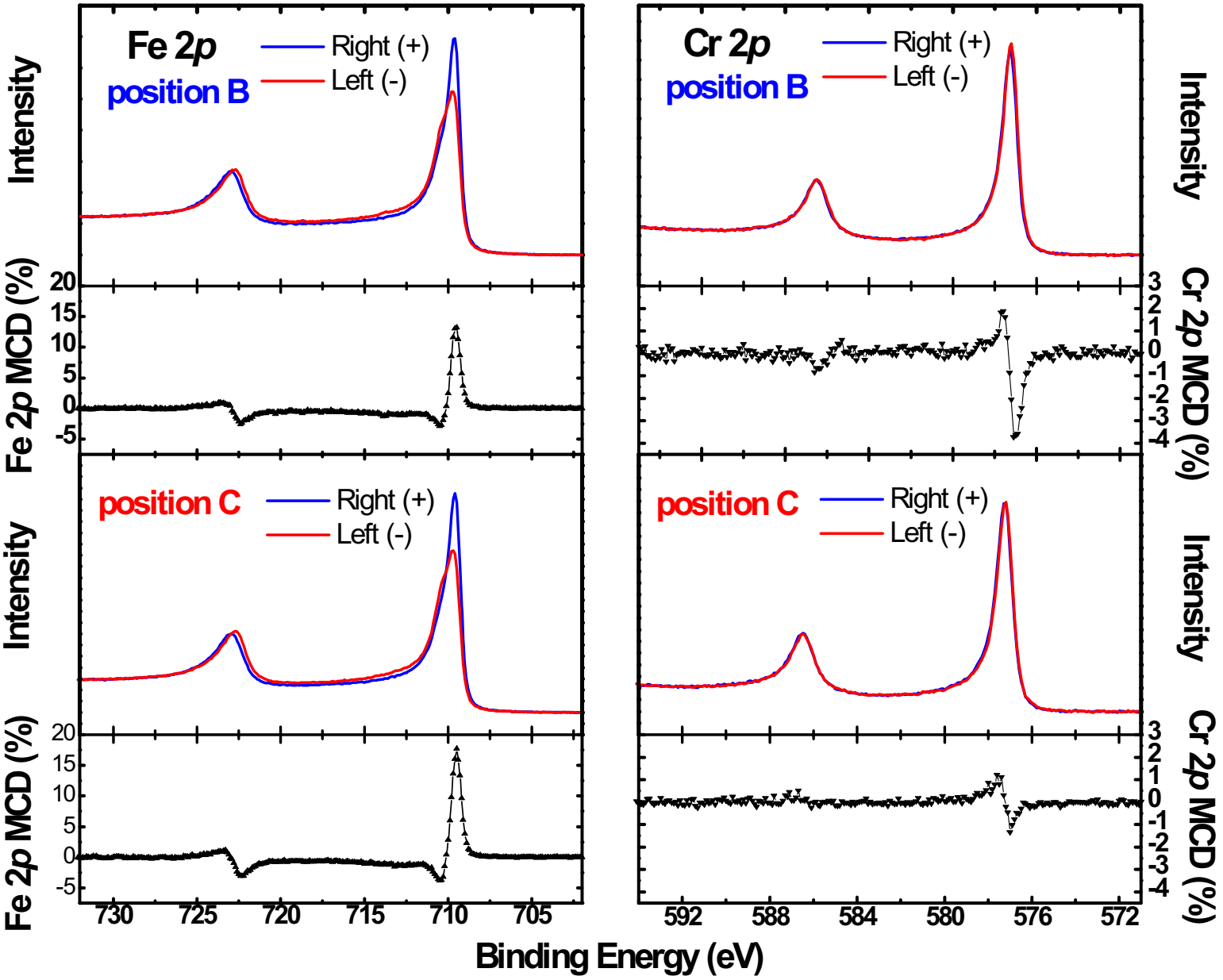

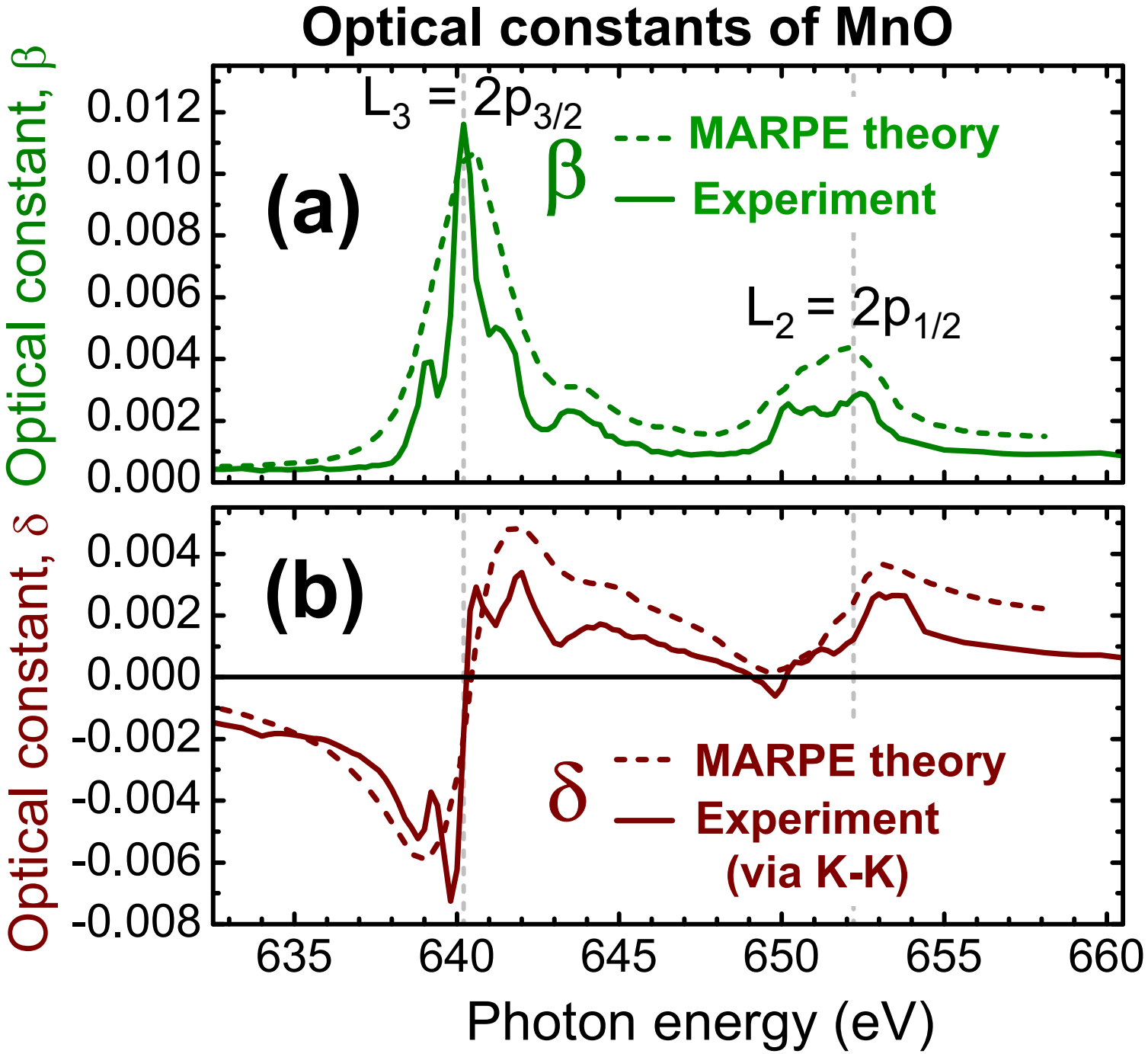
Optical constants of MnO
Optical constant, β
Optical constant, δ
(a)
(b)
L3 = 2p3/2
L2 = 2p1/2
β
δ
MARPE theory
Experiment
MARPE theory
Experiment
(via K-K)
0.012
0.010
0.008
0.006
0.004
0.002
0.000
0.004
0.002
0.000
-0.002
-0.004
-0.006
-0.008
635
640
645
650
655
660
Photon energy (eV)

# X-ray optical effects through core resonances:



(a)

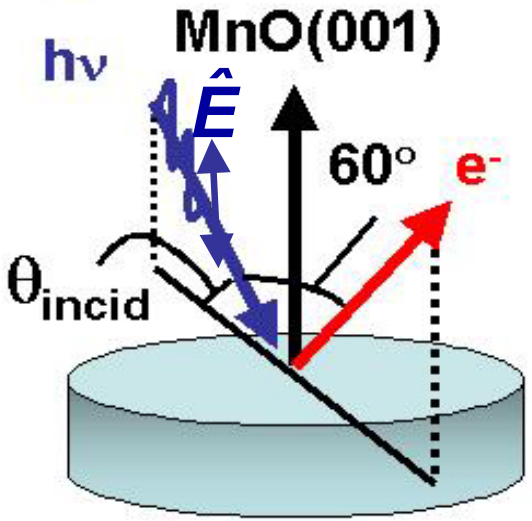


(b)

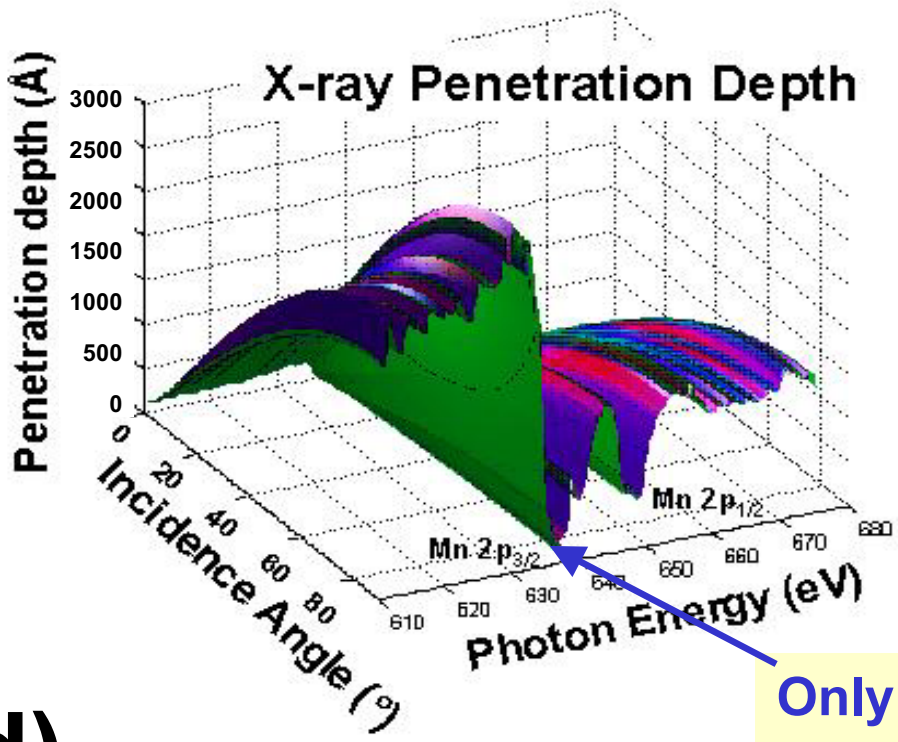


Only approx. 130 Å at normal incidence

(c)

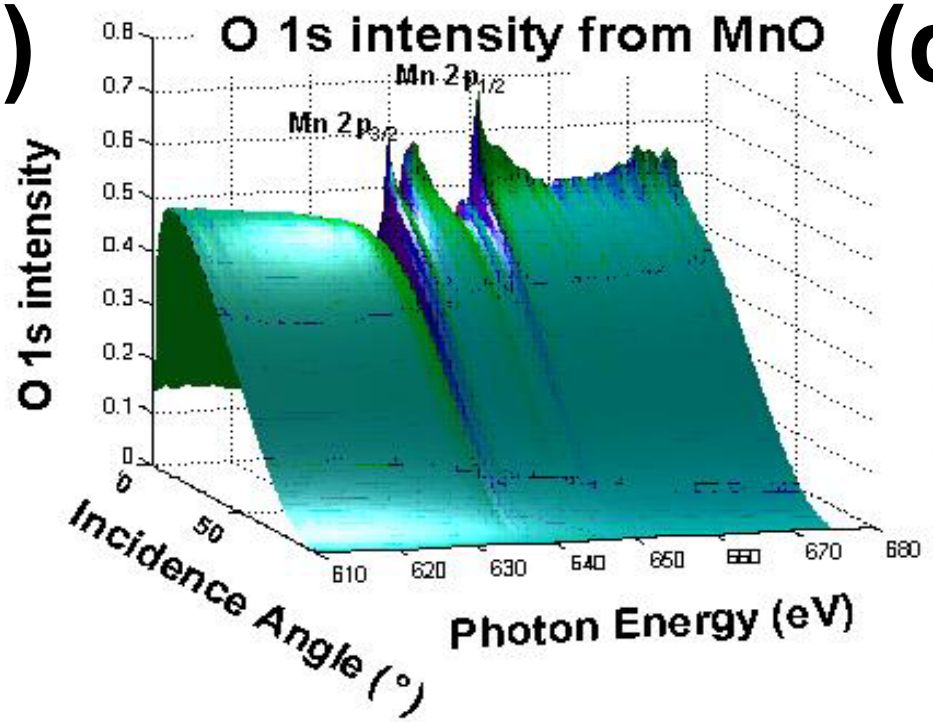


(d)

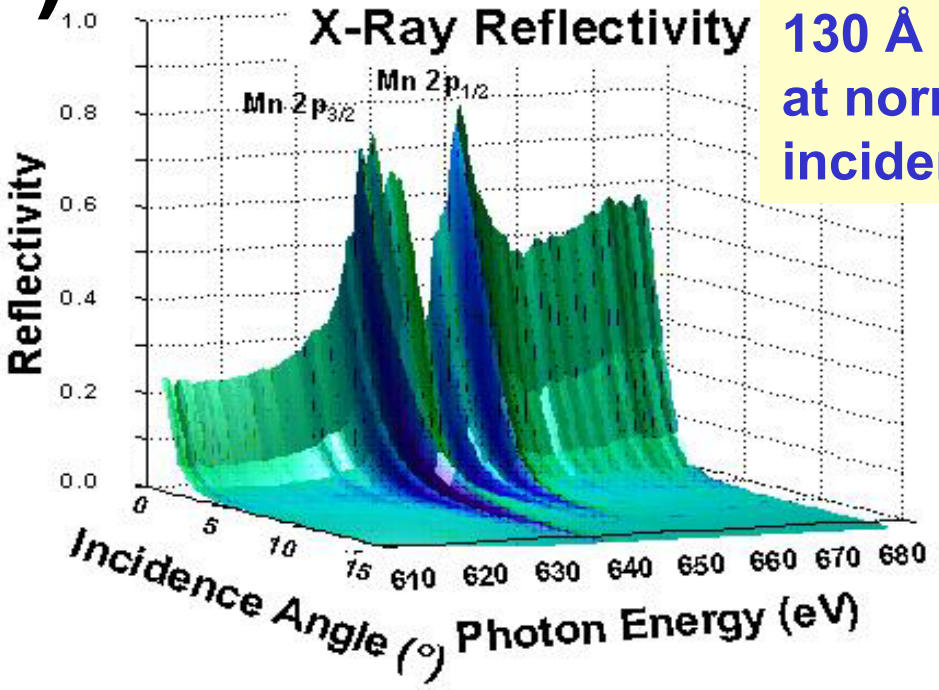

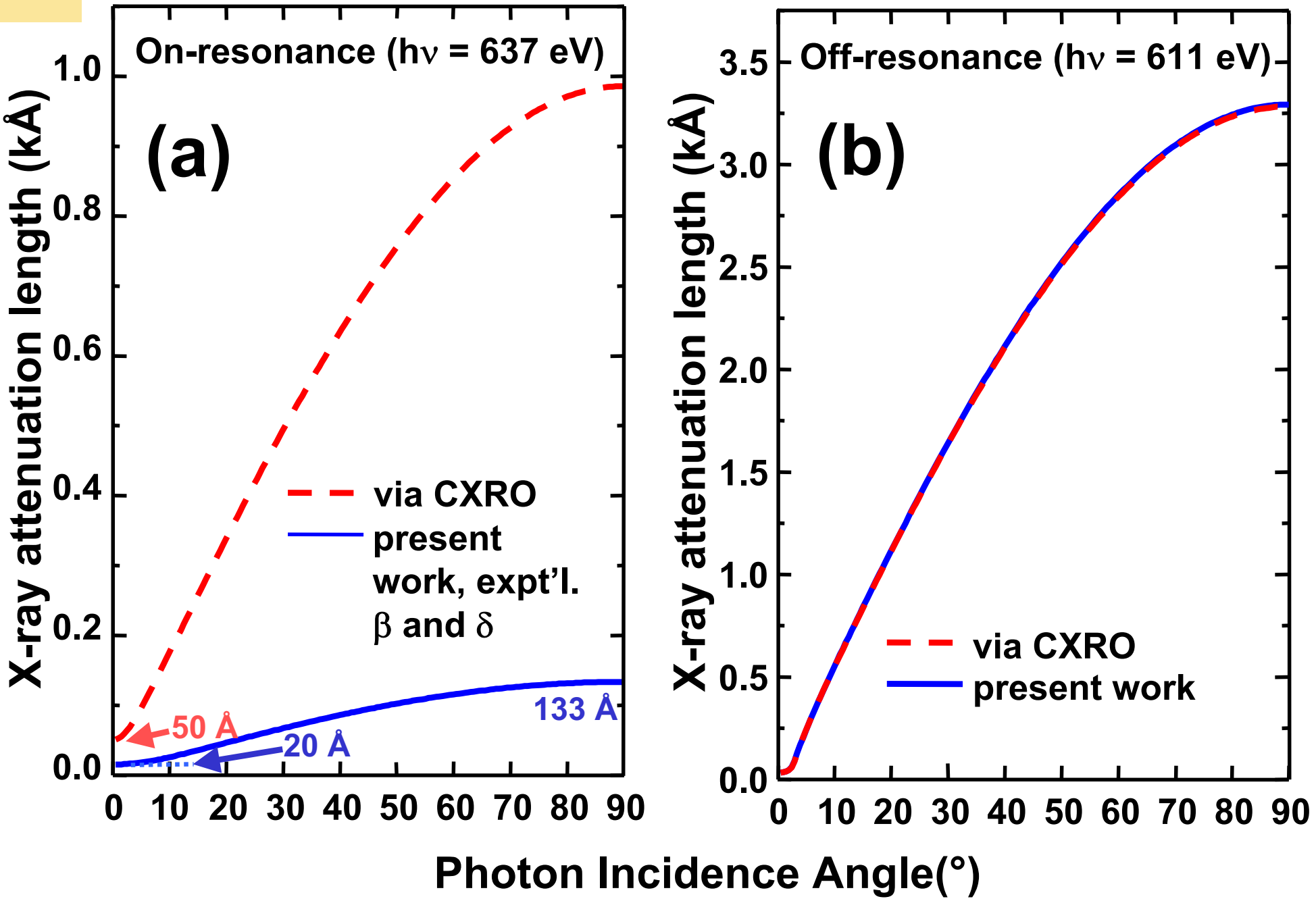
On-resonance (hν = 637 eV)
(a)
X-ray attenuation length (kÅ)
1.0
0.8
0.6
0.4
0.2
0.0
via CXRO
present work, expt'l. β and δ
50 Å
20 Å
133 Å
0 10 20 30 40 50 60 70 80 90
Off-resonance (hν = 611 eV)
(b)
X-ray attenuation length (kÅ)
3.5
3.0
2.5
2.0
1.5
1.0
0.5
0.0
via CXRO
present work
0 10 20 30 40 50 60 70 80 90
Photon Incidence Angle(°)

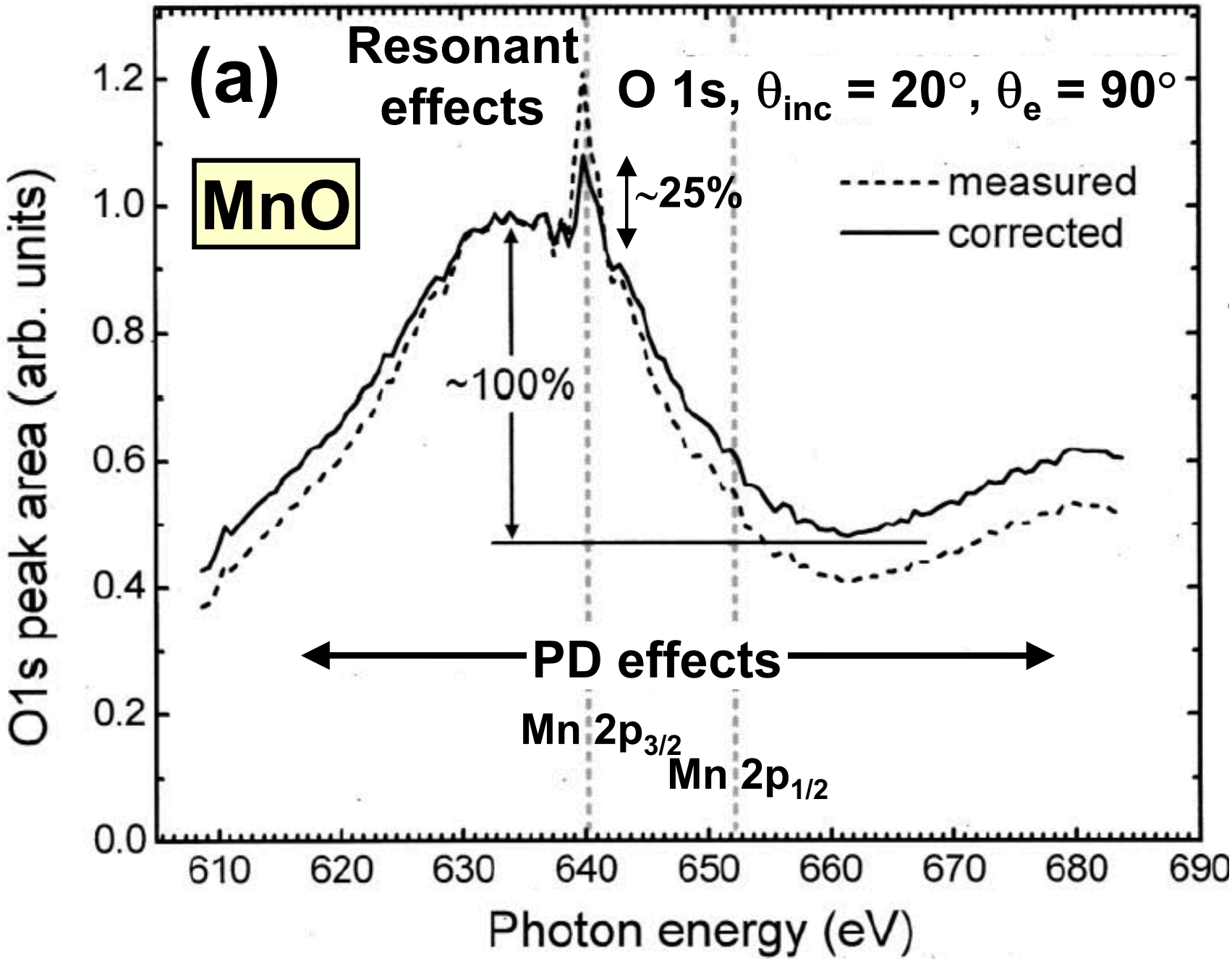
(a)
Resonant effects
O 1s, θinc = 20°, θe = 90°
MnO
~25%
measured
corrected
~100%
PD effects
Mn 2p3/2
Mn 2p1/2
O1s peak area (arb. units)
Photon energy (eV)
0.0
0.2
0.4
0.6
0.8
1.0
1.2
610
620
630
640
650
660
670
680
690

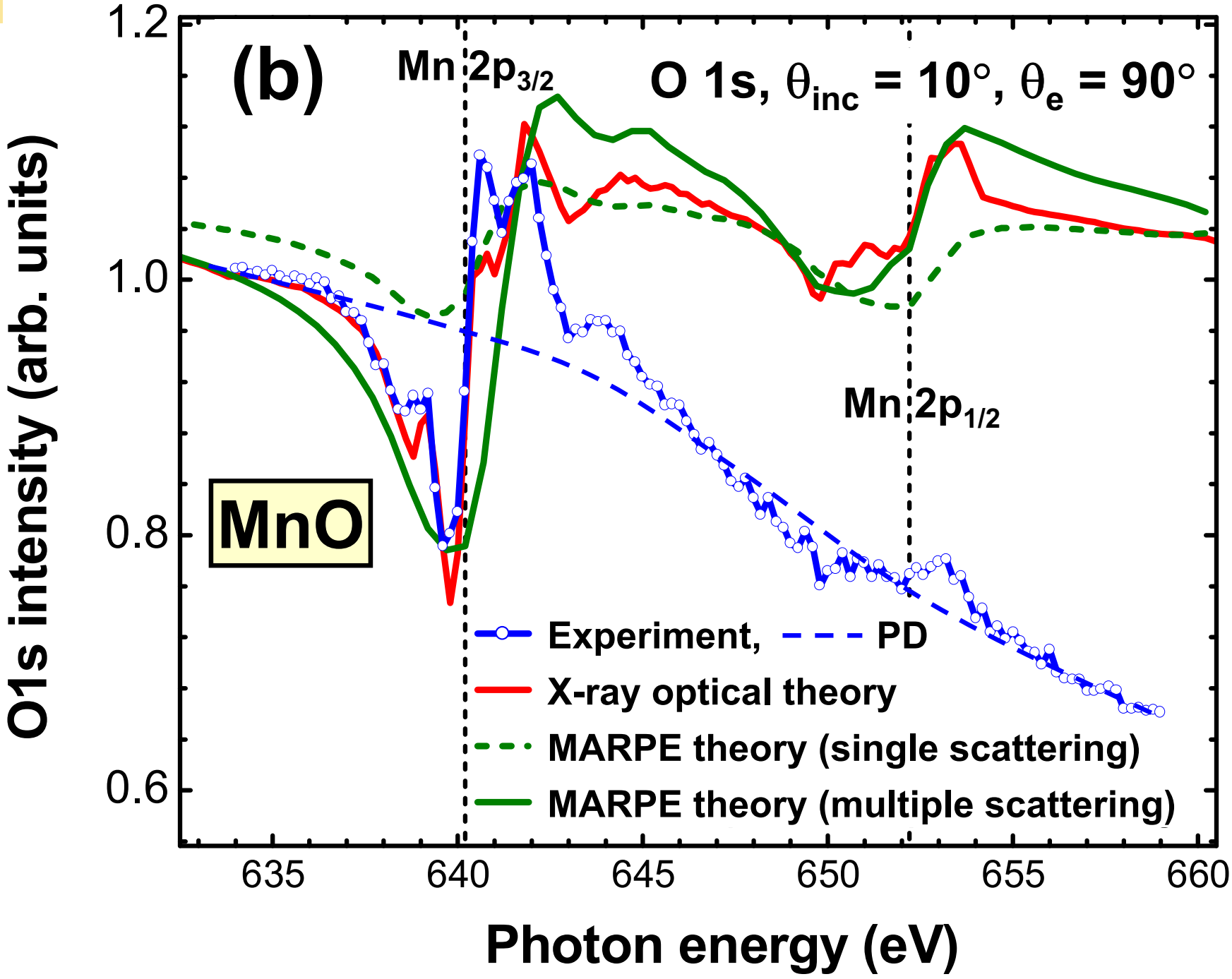
(b)
Mn 2p3/2
O 1s, θinc = 10°, θe = 90°
Mn 2p1/2
MnO
Experiment,
PD
X-ray optical theory
MARPE theory (single scattering)
MARPE theory (multiple scattering)
O1s intensity (arb. units)
Photon energy (eV)
1.2
1.0
0.8
0.6
635
640
645
650
655
660

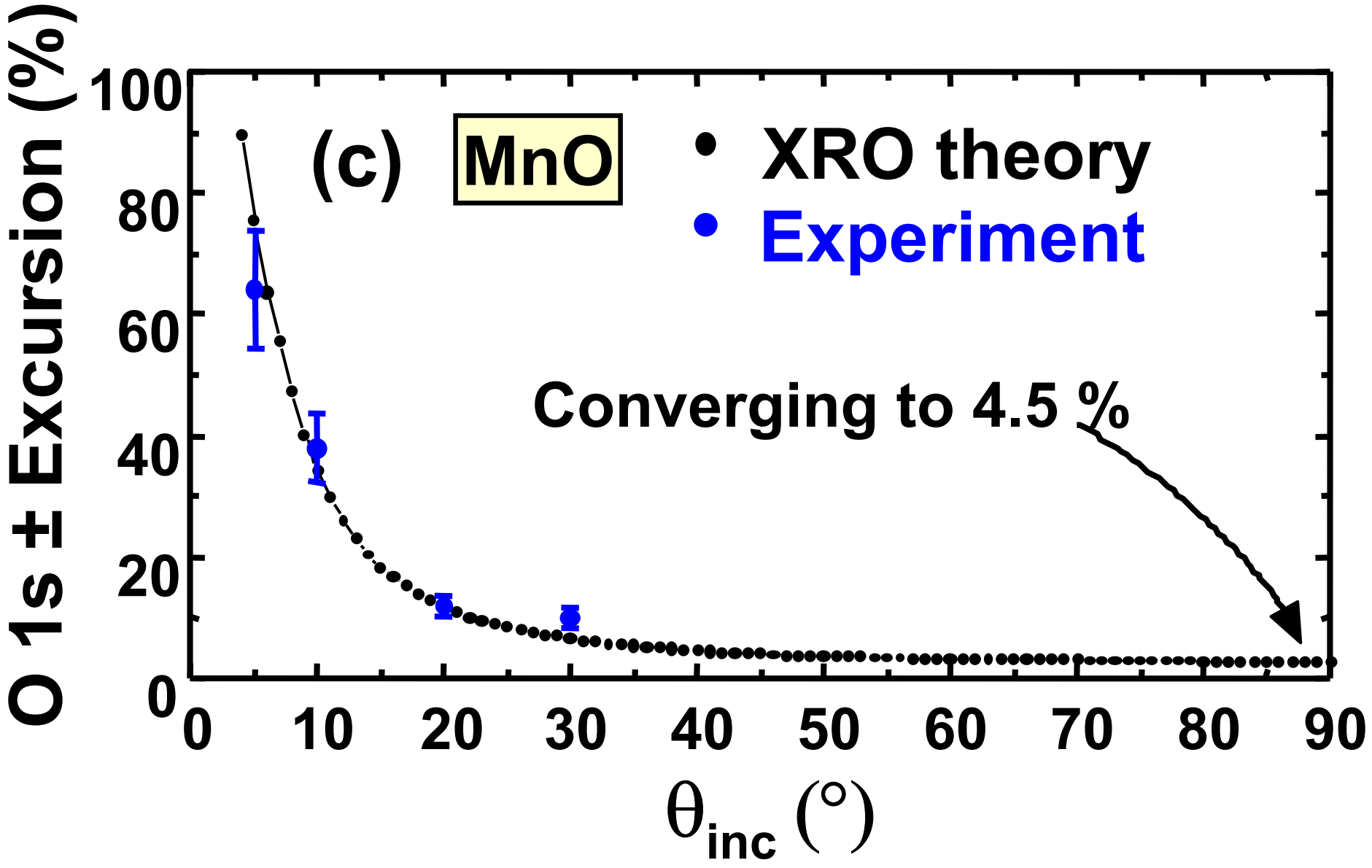
(c) MnO
XRO theory
Experiment
Converging to 4.5 %
O 1s ± Excursion (%)
θinc (°)
0
20
40
60
80
100
0
10
20
30
40
50
60
70
80
90

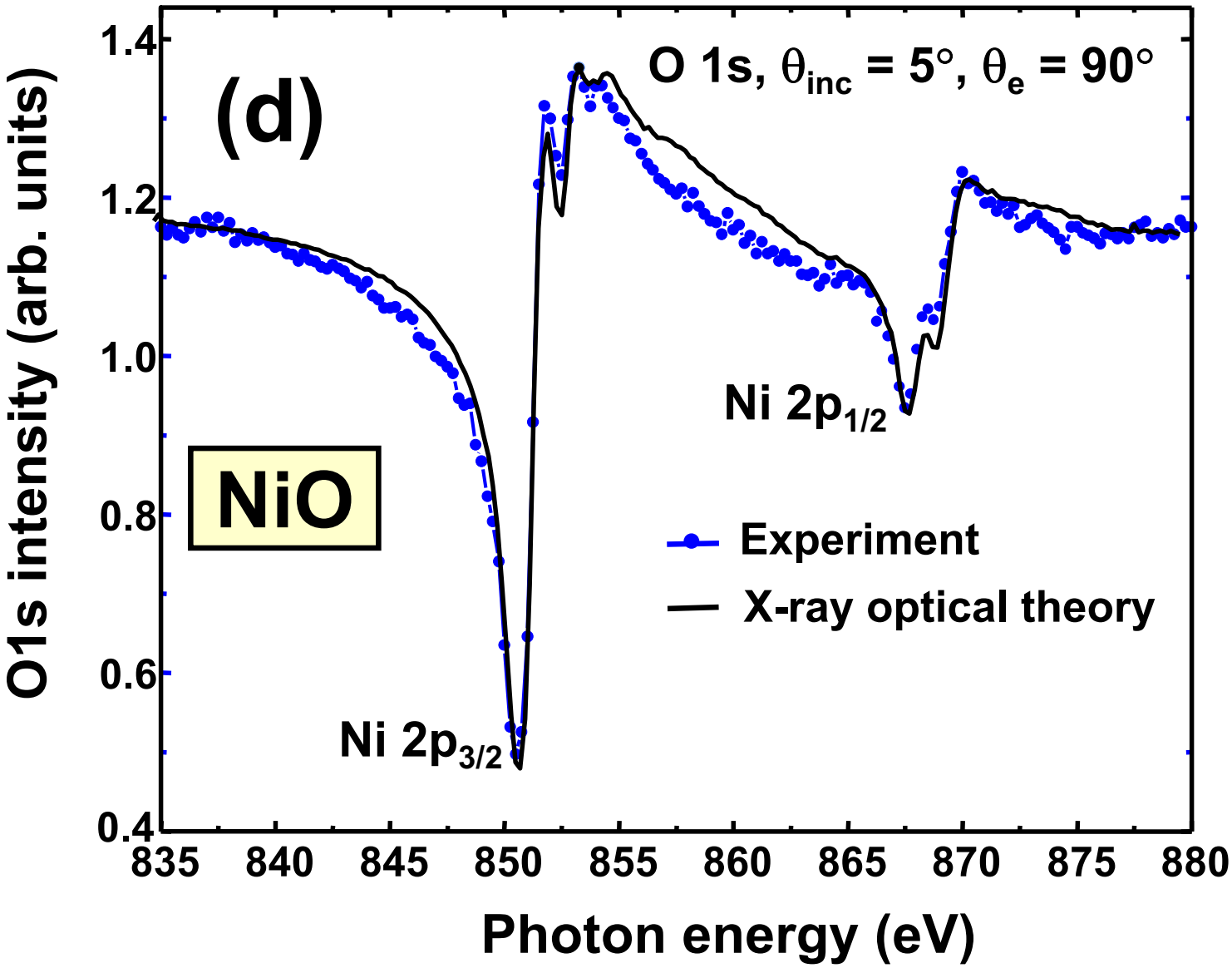
(d)
O 1s, θinc = 5°, θe = 90°
NiO
Ni 2p1/2
Ni 2p3/2
Experiment
X-ray optical theory
O1s intensity (arb. units)
Photon energy (eV)
1.4
1.2
1.0
0.8
0.6
0.4
835
840
845
850
855
860
865
870
875
880

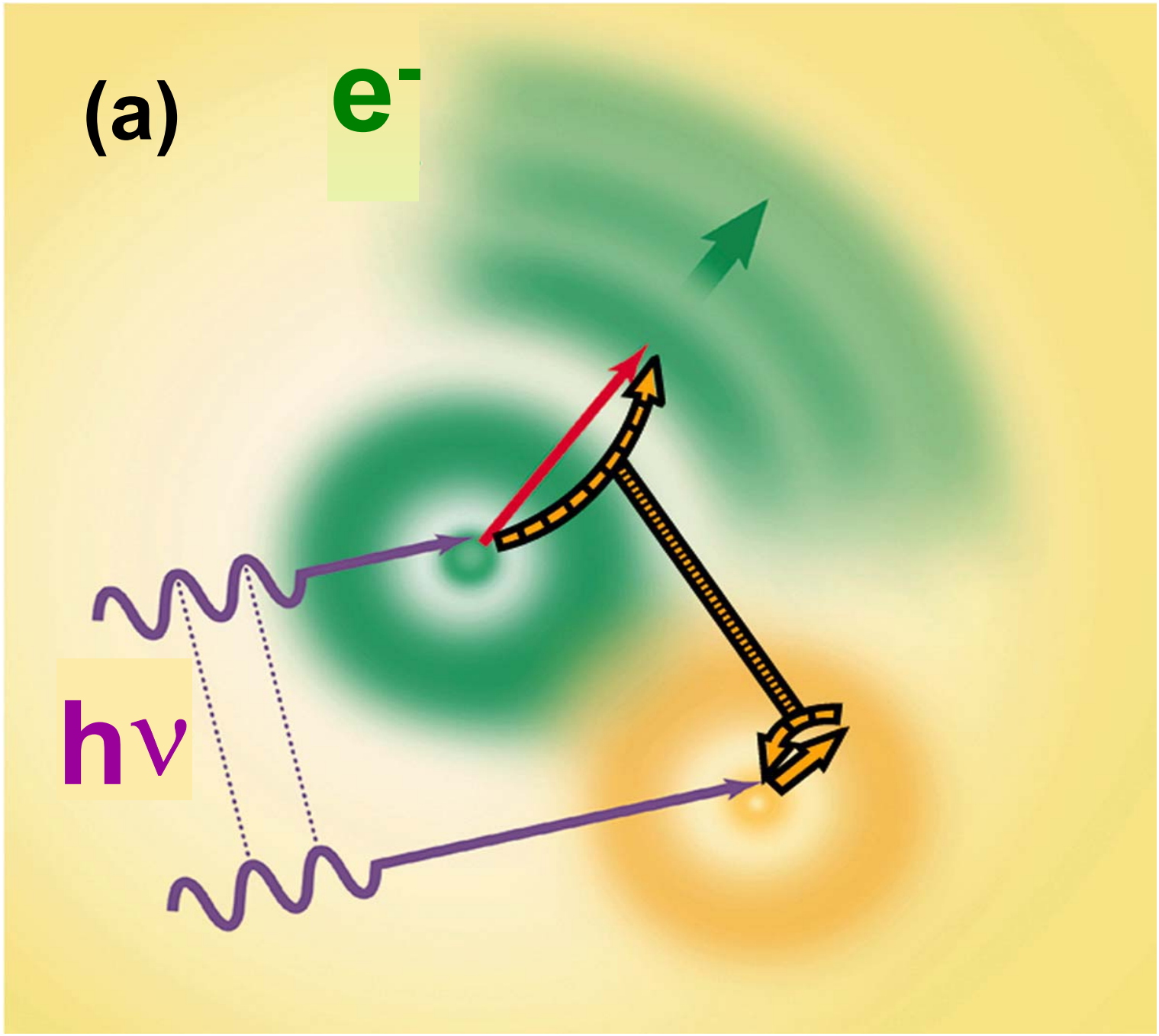
(a)
e-
hν

# (b) Multiatom Resonant Photoemission

Ex. – MnO(001): O1s emission, resonance with $Mn2p_{3/2}$

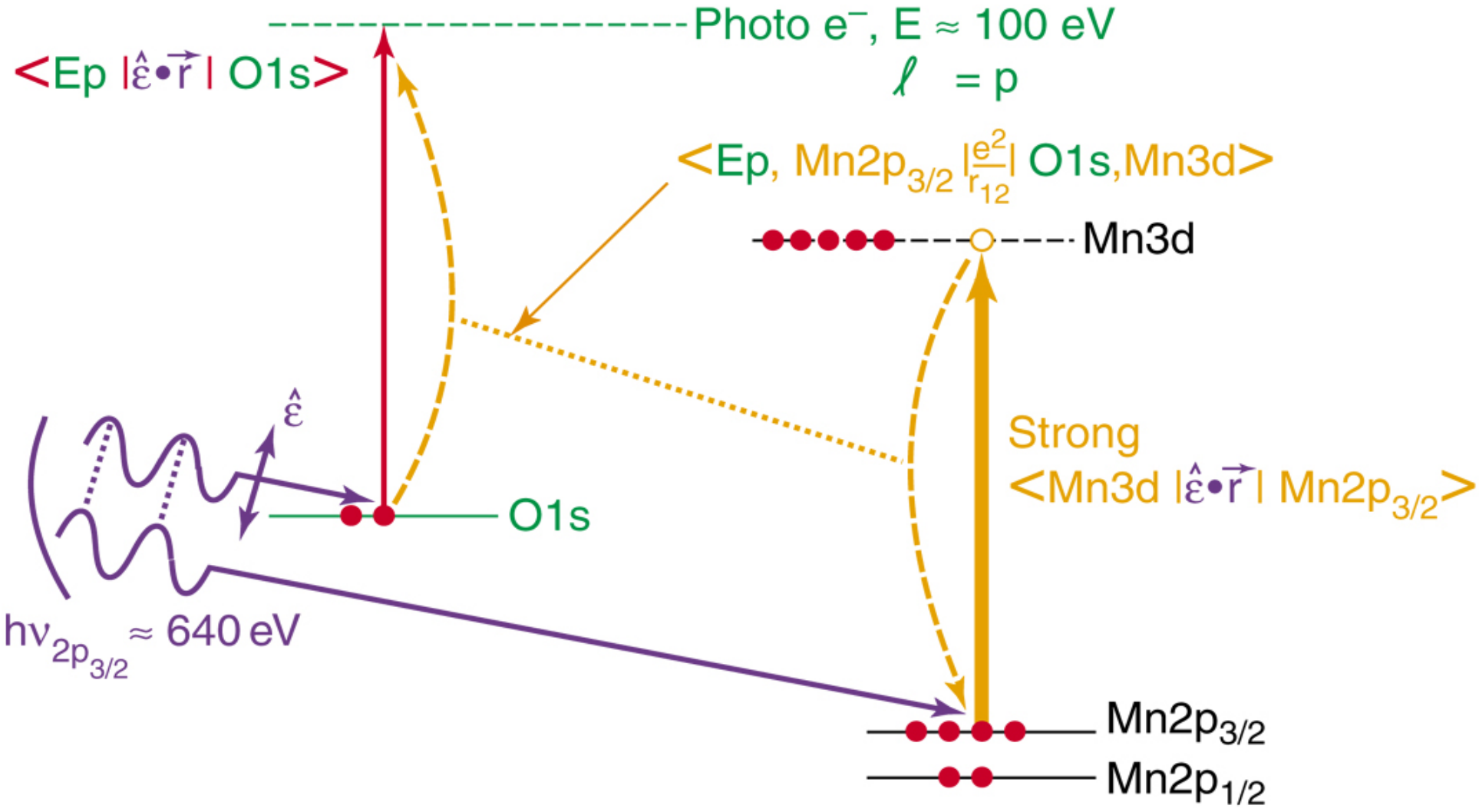

# CALCULATED SOFT X-RAY EMISSION FROM A MULTILAYER STANDING WAVE GENERATOR (SWG)-- MnO(70Å) /[$B_4C$ (30 Å) /Fe (40 Å)]$_{20}$/Si

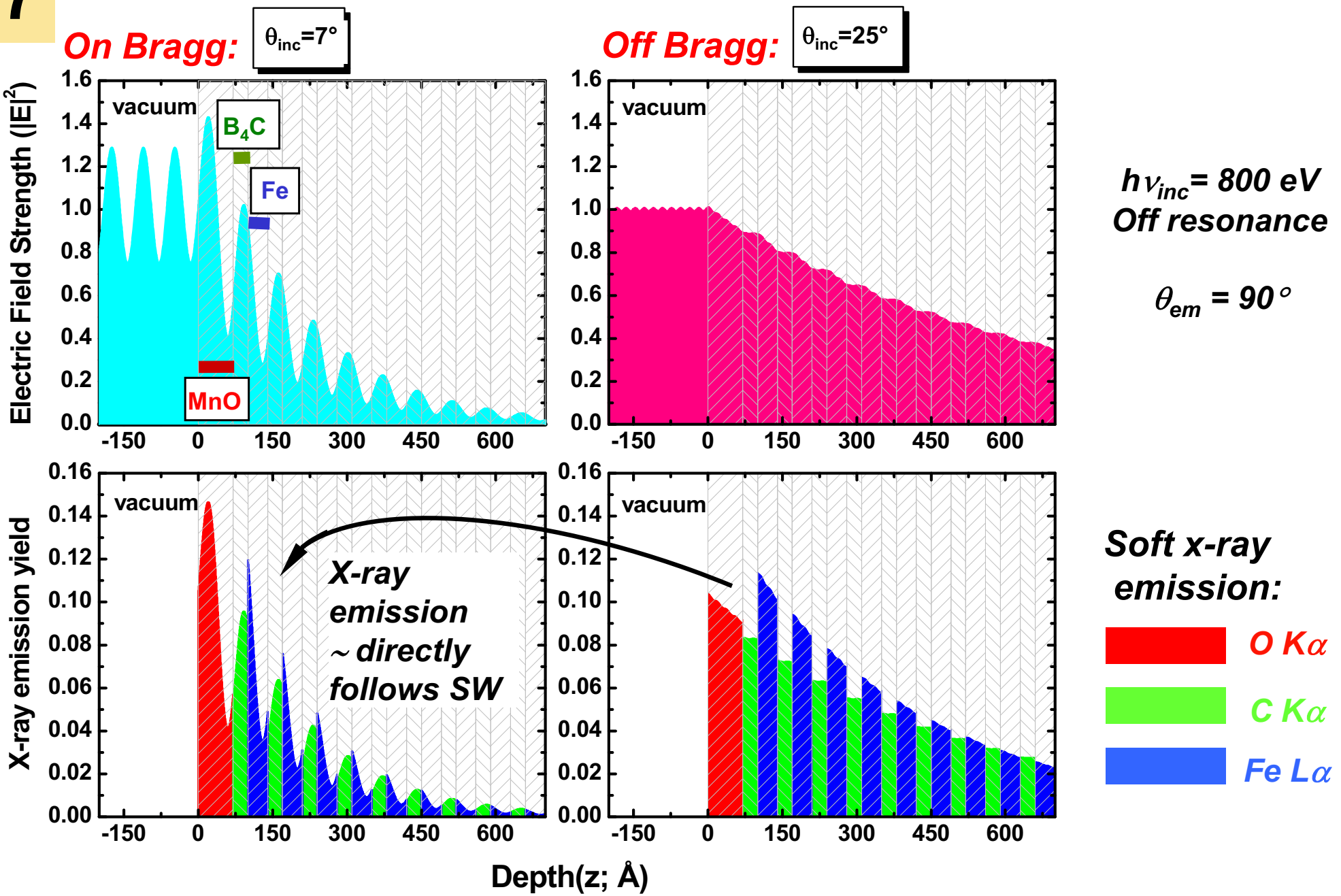

Available online at www.sciencedirect.com
SCIENCE DIRECT®
Nuclear Instruments and Methods in Physics Research A 547 (2005) 24–41
NUCLEAR INSTRUMENTS & METHODS IN PHYSICS RESEARCH Section A
www.elsevier.com/locate/nima

# X-ray photoelectron spectroscopy and diffraction in the hard X-ray regime: Fundamental considerations and future possibilities

Charles S. Fadley[a,b,*]

[a]*Department of Physics, University of California Davis, Davis, CA 95616 USA*
[b]*Materials Sciences Division, Lawrence Berkeley National Laboratory, Berkeley, CA 94720, USA*

Available online 13 June 2005

**Abstract**

The prospects for extending X-ray photoelectron spectroscopy (XPS) and X-ray photoelectron diffraction (XPD) measurements into the hard X-ray regime of 5–15 keV excitation energies are discussed from a fundamental point of view, in some cases using prior results obtained in the 1–2 keV range as starting points of discussion, together with theoretical estimates of behavior at higher energies. Subjects treated are: the instrumentation improvements needed to optimize peak intensities; the tuning of experimental conditions to achieve bulk or surface sensitivity; the use of grazing incidence to suppress spectral backgrounds; the use of standing waves created by Bragg reflection from crystal planes or synthetic multilayers to achieve position-sensitive densities of states, compositions, and magnetizations; photoelectron diffraction and Kikuchi-band effects as element-specific local structure probes; and valence-level measurements, including the role of non-dipole effects and mechanisms leading to complete Brillouin zone averaging and density-of-states like spectra. Several distinct advantages are found for such high-energy extensions of the XPS and XPD techniques.


*PACS:* 68.49.Uv; 79.60.−i; 61.14.Qp; 73.20.−r; 71.20.−b

*Keywords:* Photoelectron spectroscopy; Photoelectron diffraction; Electronic structure; Hard X-rays; Synchrotron radiation

## 1. Introduction

X-ray photoelectron spectroscopy (XPS or ESCA) is by now a very widely used technique for characterizing the surface and bulk properties of a broad variety of materials. Although the first measurements of this kind by Siegbahn et al. in the mid-1950s were actually carried out with photon

*Department of Physics, University of California Davis; Materials Sciences Division, Lawrence Berkeley National Laboratory, 1 Shields Ave., Davis, CA 95616 USA. Tel.: +1 530 7521500; +1 530 7524717.
*E-mail address:* fadley@physics.ucdavis.edu.

0168-9002/$ - see front matter © 2005 Published by Elsevier B.V.
doi:10.1016/j.nima.2005.05.009

energies in the 5–8 keV range [1], the desire for higher-energy resolution led immediately to a focus on excitation sources such as Mg Kα (1253.6 eV) and Al Kα (1486.7 eV), sometimes together with a crystal monochromator [1]. The development of synchrotron radiation (SR) sources over the past few decades has extended the energy range downward, erasing the distinction between ultraviolet photoelectron spectroscopy (UPS) and XPS and has by now provided energy resolutions below 0.1 eV, with corresponding enhancements in the ability to study chemical shifts, multiplets splittings, and other fine structure in both core and valence spectra. Along the way, however, it was suggested by Pianetta and Lindau in 1974 that high-resolution XPS could be profitably carried out in the 5–15 keV range with SR [2], an idea that has only recently been revived by several groups and demonstrated experimentally [3], as discussed in other articles in this issue.

In this article, I will discuss some fundamental considerations of carrying out XPS and the closely related technique of X-ray Photoelectron (XPD) in the hard X-ray regime, including instrumental considerations, what additional types of information might be gained from such measurements in the future, and certain limitations and special characteristics. In several instances, I will use data obtained at current typical excitation energies of about 1.5 keV to illustrate effects that should be useful when obtained with excitation in the 5–15 keV regime, together with theoretical estimates of how these effects will manifest themselves at these higher energies.

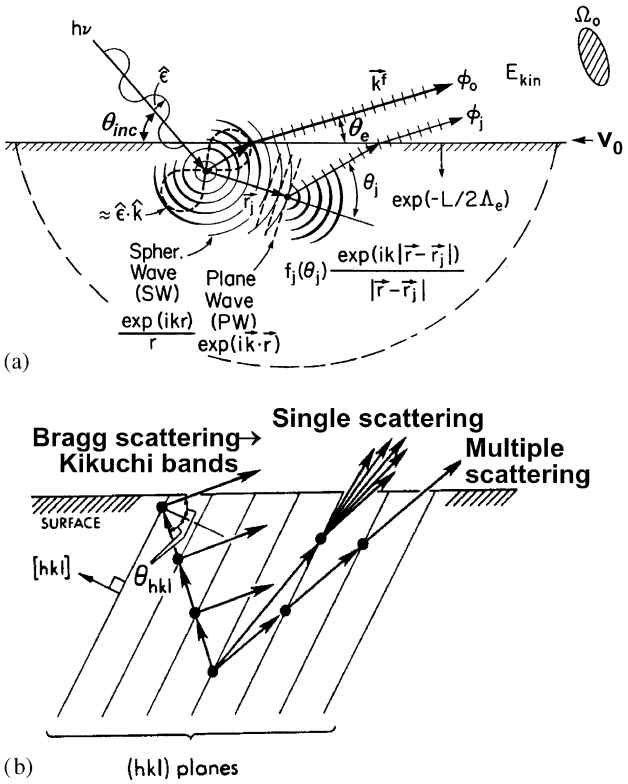


Fig. 1. (a) The basic physical process in X-ray photoelectron excitation by radiation with polarization $\hat{\varepsilon}$, including elastic scattering in either the plane-wave, or more accurate spherical wave, approximations; inelastic scattering through an attenuation length $\Lambda_e$; escape across the surface barrier (inner potential) $V_0$, and entry into the final acceptance solid angle of the spectrometer $\Omega_0$. For $s$ subshells and in the dipole approximation, the initial outgoing wave has an angular form proportional to $\hat{\varepsilon}\cdot\hat{k}$, with $\hat{k}$ a unit vector in the direction of propagation. (b) Illustration of additional Bragg-like scattering processes which arise for higher energies of excitation, leading to Kikuchi-band behavior. Multiple scattering must also be considered in accurately modeling all elastic scattering effects.

## 2. Photoelectron intensities

A primary reason for which hard X-ray photoelectron spectroscopy (HXPS) has not been more widely practiced to date is the general conclusion that intensities would be too low. Thus, a brief overview on this point is worthwhile. Although the argument will be presented for core-level intensities, the basic ideas also apply to valence levels. Fig. 1(a) illustrates the basic physical process involved, including the effects of both inelastic scattering and elastic scattering.

The intensity of a photoelectron peak from a given spin–orbit-split level $n\ell j$ associated with an atom $Q$ in a homogeneous polycrystalline sample will in general be given by [4]

$$
\begin{aligned}
I(Qn\ell j) &= (\text{incident X}-\text{ray flux}) \\
&\times (\text{area of illuminated sample seen by analyzer}) \\
&(Qn\ell j \text{ differential photoelectric cross section}) \\
&\times (\text{solid angle accepted by analyzer}) \\
&\times (\text{density of atoms } Q) \\
&\times (\text{mean photoelectron escape depth}) \\
&\times (\text{overall detection efficiency}) \qquad (1)
\end{aligned}
$$

or in obvious notation,

$$I(Qnlj) = I_0(h\nu) \times A_0 \times (\mathrm{d}\sigma_{Qnlj}(h\nu)/\mathrm{d}\Omega) \times \Omega_0 \times \rho_Q \times \Lambda_{\mathrm{MED}}(E_{\mathrm{kin}}) \times D_0. \quad (2)$$

Here, we have emphasized the functional dependencies on photon energy or electron kinetic energy, as well as the optical properties of the electron energy analyzer, since the selective tuning of the latter is crucial to the future success of HXPS. The mean photoelectron escape depth $\Lambda_{\mathrm{MED}}(E_{\mathrm{kin}})$ in general must allow for both inelastic and elastic electron scattering, as updated recently by Jablonski and Powell [5], a point to which we return below. More approximately, $\Lambda_{\mathrm{MED}}(E_{\mathrm{kin}})$ can be replaced simply by the inelastic attenuation length $\Lambda_{\mathrm{e}}(E_{\mathrm{kin}})$.

Considering the factors here in order, we first note that third-generation SR undulators, combined with suitable hard X-ray monochromators, can provide highly intense ($\sim 10^{11}$–$10^{12}$ photons/s) and monochromatic ($\Delta(h\nu) \leqslant 0.1$ eV) beams for HXPS. These can in turn be focused into a very small spot size of the order of tens of microns that can be well matched to the acceptance areas $A_0$ of current high-throughput and high-resolution analyzers. The key point here is that light which falls outside of the analyzer view is wasted. Of course, photoelectric cross-sections fall continuously as the energy is tuned above a given binding energy threshold, with approximate variations in a high-energy asymptotic, yet non-relativistic, approximation theoretically expected to be: $\sigma_{Qnlj}(h\nu) \propto (E_{\mathrm{kin}})^{-7/2}$ for s subshells and $\propto (E_{\mathrm{kin}})^{-9/2}$ for p, d, and f subshells [6(a)], and numerical tabulations of more accurate relativistic calculations of *total* subshell cross-sections $\sigma_{Qn\ell j}(h\nu)/\mathrm{d}\Omega$ for the entire period table and for photon energies from 1–100 keV have been published by Scofield [6(b)]. For several energies from 100–5000 eV and for heavier elements with $Z = 50-100$, Nefedov et al. have also calculated both relativistic cross-sections and the angular distribution_parameters that are essential for deriving the *differential* photoelectric cross-section $\mathrm{d}\sigma_{Qn\ell j}(h\nu)/\mathrm{d}\Omega$ [7].

The solid angle $\Omega_0$ accepted by the analyzer is a property of the particular electron optical system, which usually includes some kind of retarding lens that magnifies the image $A_0$ by some factor $M$ to an area at the entrance to the analyzer of $A' = MA_0$. A typical analyzer system is shown in Fig. 2, with the actual energy analysis section here being illustrated for the much-used hemispherical electrostatic configuration. The key tradeoffs in the retarding lens and the final energy analysis stage are governed by the Liouville Theorem, which dictates that source brightness before retardation $B_0$ and that after retardation $B'$ must be related by

$$\frac{B'}{B_0} = \frac{E_{\mathrm{pass}}}{E_{\mathrm{kin}}} \quad (3)$$

where $E_{\mathrm{kin}}$ is the kinetic energy on leaving the sample and $E_{\mathrm{pass}}$ is the final energy of analysis.

Combining this with the conservation of electron flux on traversing the complete electron optical system finally yields via the Lagrange–Helmholtz relation to the form most convenient for this analysis:

$$A'\Omega'/A_0\Omega_0 = M\Omega'/\Omega_0 = E_{\mathrm{kin}}/E_{\mathrm{pass}} \equiv R, \quad (4)$$

where $\Omega'$ is the solid angle of acceptance after retardation and at the entry to the final energy analysis element, and $R$ is the retardation ratio, which will generally be $\gg 1$ for HXPS measurements. This

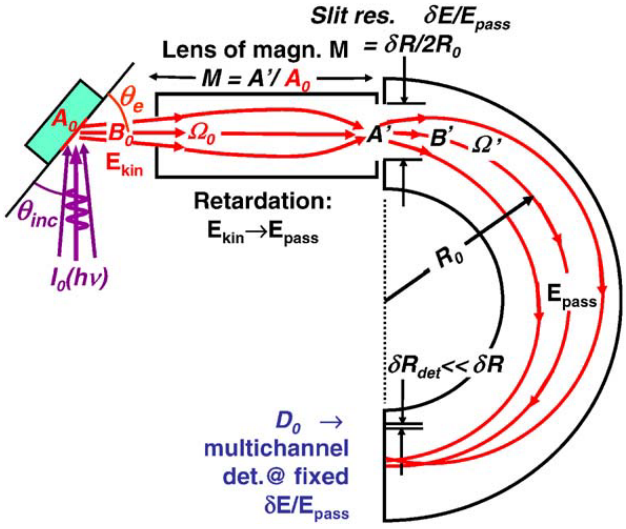


Fig. 2. The fundamental parameters controlling the final photoelectron intensity, here illustrated for the case of a hemispherical electrostatic analyzer with a retarding, imaging lens between it and the sample. Relevant symbols are defined in the text.

relationship of course only applies to those electron trajectories that pass through the entire electron optical system, allowing for the effects of any slits or collimators that may limit trajectories. A final important consideration is that the energy resolution of the final analysis stage $\delta E/E_{\mathrm{pass}}$ can be connected to Eq. (4) by

$$A'\Omega' \approx CR_0^2\,(\delta E/E_{\mathrm{pass}})^{1.5-2.0} \quad (5)$$

where we have assumed a hemispherical electrostatic analyzer as the final element, $C$ is a constant characteristic of the type of analyzer, and $R_0$ is the radius of the central trajectory in the analyzer section. From Eqs. (4) and (5), we can see that, if $A_0$ is sufficiently small (as permitted by the highly focused SR beam), and $R$ and $M$ are sufficiently large, $\Omega_0$ can be very large, while at the same time, via Eq. (5), $A'$ and $\Omega'$ together can be maintained sufficiently small to obtain the desired final absolute energy resolution. Roughly speaking, retardation permits larger $A'\Omega'$ for a given desired energy resolution $\delta E/E_{\mathrm{kin}}$, and high magnification permits reducing $\Omega'$, again consistent with this resolution. Thus, the highly focused spot in a SR beamline, and carefully designed retarding electron optics with magnifications of 25 or higher, are crucial for the practical realization of HXPS, as discussed elsewhere [3].

Finally, being able to detect multiple energies in the final focal plane of the analyzer (cf. Fig. 2) is also crucial, as this effectively increases the factor $D_0$, with several approaches available for this: multiple channeltrons, microchannel plates (MCPs) coupled with resistive anodes or CCD detectors, and a newer approach based on MCPs with custom-designed integrated circuits [8]. Ideally, the width of each detector channel $\delta R_{\mathrm{det}}$ should be much smaller than the other contributions to resolution, as for example, that due to the entrance slit size $\delta R$ in Fig. 2. Other articles in this issue will discuss more concrete examples of experimental systems based on these principles, but it is easy to estimate that intense core levels (e.g. Au 4f) will generate $10^4$–$10^5$ electrons/s over the full spectrum, and even weaker valence bands have been successfully studied by now [3].

Thus, although cross-section dependence on photon energy as one goes into the hard X-ray regime is a serious handicap to HXPS, the availability of brighter SR sources, together with electron analyzer systems designed to take advantage of the small spot sizes involved and energy retardation before energy analysis, can compensate this so as to yield adequate data acquisition rates, as demonstrated in recent work.

## 3. Surface vs. bulk sensitivity

Certainly a primary attraction of HXPS is in increasing the ability to more accurately measure true bulk properties, and this is connected to the well-known energy variation of the electron inelastic mean free path $\Lambda_{\mathrm{e}}(E_{\mathrm{kin}})$, which at higher energies is expected to vary as $(E_{\mathrm{kin}})^{0.50-0.75}$ [5(b),9]. Simple geometric considerations then show that, if the electron exit angle with respect to the surface is $\theta_{\mathrm{e}}$ (cf Fig. 1(a)), then the mean sensing depth of the measurement will go as $\Lambda_{\mathrm{e}}\sin\theta_{\mathrm{e}}$, thus providing a simple way of estimating, and varying, the degree of surface sensitivity. Thus, HXPS at roughly 10 keV should certainly be more bulk sensitive than measurements at 1 keV, with measurement depths 3–5 times larger. Again, for the example of metallic Au, $\Lambda_{\mathrm{e}}(E_{\mathrm{kin}})$ can be estimated to be about 70 Å at $E_{\mathrm{kin}} = 10$ keV [9].

An accurate estimate of true measurement depths also needs to include the effects of elastic scattering, especially at lower kinetic energies [5]. This is because elastic scattering can cause electrons initially emitted at angles nearer to the surface normal to be scattered into angles further from the normal, and it is why the more accurate $\Lambda_{\mathrm{MED}}(E_{\mathrm{kin}})$ is included in Eqs. (1) and (2). Such effects have been discussed in detail previously [5], and they reduce the degree of surface sensitivity enhancement possible by going to lower electron exit angles relative to the surface. Such effects also complicate the interpretation of such data. However, an additional advantage of HXPS is that elastic scattering will be strongly peaked in the forward direction for 5–15 keV electrons, as will be discussed in more detail below, thus making the linear trajectory model that is involved in arriving at the $\Lambda_{\mathrm{e}}\sin\theta_{\mathrm{e}}$. estimate above a more accurate approximation [10].

A final effect to be considered in analyzing measurements with variable electron emission angles is the inner potential $V_0$ at the sample surface (cf. Fig. 1(a)). This has a value in the range 5–25 eV, and can significantly refract photoelectrons as they leave the surface [11], with this effect being worse for the grazing emission angles that are of greatest interest for enhancing surface sensitivity. However, going to hard X-ray excitation energies will much reduce this effect, making the interpretation of variable-angle HXPS data more straightforward in yet a second respect.

HXPS thus should not only be more bulk sensitive, but it should also permit more quantitative analyses of variable electron emission angle measurements so as to more quantitatively sort out bulk and surface effects. As a final word of caution, however, the expected mean emission depths in HXPS are still only ca. 50–100 Å, and small enough that consideration still must be given to surface contamination or surface reaction effects, especially for more reactive samples.

## 4. X-ray optical effects and total reflection

The effects of the onset of total X-ray reflection on photoelectron intensities were first discussed by Henke [12], and they eventually have led to the intentional use of total reflection geometries as a convenient tool for reducing the inelastic scattering background in XPS spectra [13]. As a recent example of the use of what has been termed total reflection XPS (TRXPS) or grazing-incidence XPS (GIXPS), I show in Fig. 3 broad-scan spectra obtained with Al Kα excitation from an HF-etched Si wafer with a high angle of incidence (10°, labeled Normal XPS) and with a low angle of incidence below the critical angle (1.1°, labeled TRXPS) [14]. The suppression of the inelastic background in the TRXPS spectrum is significant. Although all prior work of this type has been done in the typical XPS energy regime of about 1 keV, making use of total reflection to reduce what will probably be more significant inelastic backgrounds in spectra at 5–15 keV excitation energies appears to be very desirable, provided that the sample surface is flat enough to achieve the uniformly low

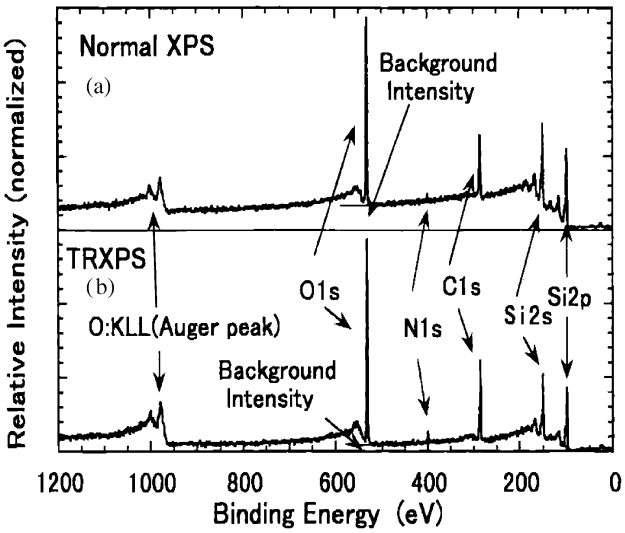


Fig. 3. Experimental data illustrating the reduction in elastic background that has been achieved in an XPS measurement on a Si surface with 1.5 keV excitation energy. (a) Normal XPS with a high X-ray incidence angle of 10°. (b) Total reflection XPS with a grazing incidence angle of 1° that is very close to the critical angle [14].

average angles required. As some indication of how this might be achieved, Fig. 4 shows calculations for 10 keV photons incident on Au [15], and it is clear that the mean depth of excitation can be reduced to values that are comparable with the expected mean electron emission depth by going to incidence angles of 1° or less. Furthermore, as long as the mean depth of X-ray excitation is much greater that the mean emission depth of the photoelectrons, the full degree of bulk sensitivity can be achieved, but still with what should be spectra with much lower inelastic background intensity. This latter condition implies working somewhat above the critical angle. For the example in Fig. 4, an incidence angle of 1° that is about 2.5 times the critical angle would still yield an X-ray attenuation length about 10$x$ larger than the estimated mean emission depth of the photoelectrons.

## 5. Standing wave studies of valence electronic structure and buried interfaces

Closely related to the X-ray optical effect discussed above is using Bragg reflectivity from a

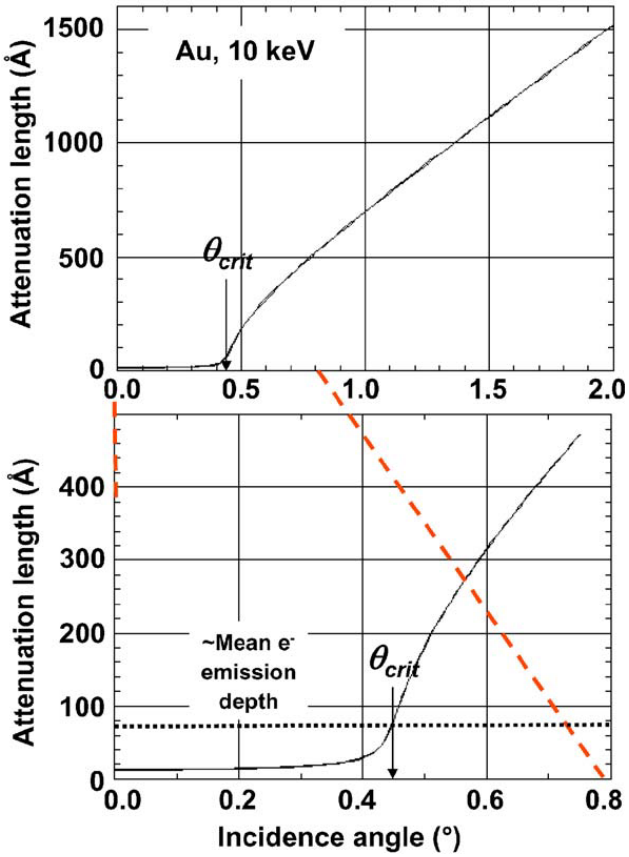


Fig. 4. Calculated X-ray attenuation lengths for 10 keV X-rays normal to a Au surface (via Ref. [15]), with the critical angle indicated, together with an estimate of the mean emission depth for 10 keV photoelectrons from this surface (dotted line, extrapolated from results of Ref. [9]). Dashed lines indicate the region in (a) that is expanded in (b).

set of crystal planes so as to set up a strong standing-wave modulation of the exciting electric field strength, and then rocking the crystal so as to move the standing wave with respect to the atomic positions. This has permitted Woicik and co-workers to study the site-specific valence-band structure of metal oxides, with obvious implications for future applications to other materials, especially if the photon energy is taken to higher values in the 5–15 keV regime [16]. This pioneering work is discussed in a separate article in this volume [17].

Beyond such crystal-plane Bragg reflections, it should also be possible to use reflections from synthetic multilayer structures to selectively tune the sensing depth in HXPS so as to study buried interfaces. To illustrate this, Fig. 5 shows a particular sample configuration which has recently been used in conjunction with soft X-ray excitation at about 1 keV to successfully study a buried interface between Fe and Cr that is of relevance to the giant magnetoresistance effect [18,19]. Here, the sample is grown on top of a synthetic multilayer mirror composed of 40 bilayers of $B_4C$ and W, with a periodicity of 40 Å that will also be the period of the soft X-ray standing wave above the surface of the multilayer. The sample consists of a wedge of Cr and an overlayer of Fe of constant thickness. Since the focused X-ray spot is much smaller than the sample and the wedge slope is very small, it is possible to effectively scan the standing wave through the interface by scanning the sample in position along the direction of the slope of the wedge. By combining such sample scanning measurements with rocking curve measurements of Fe and Cr core photoelectron intensities, as well as with magnetic circular dichroism measurements for both Fe and Cr and comparing the data with X-ray optical calculations [19], it has been possible to determine the concentration profiles and magnetization profiles for both species through the buried interface, with final results as shown in Fig. 6 [18].

Standing-wave measurements of both types (crystal planes and multilayer structures) should be of considerable interest for HXPS studies. As one illustration of the strength of such standing wave effects in multilayer work, Figs. 7(a)–(b) show the reflectivity from a synthetic multilayer exactly like that used in the soft X-ray studies of Figs. 5 and 6, but at two incident energies of 1.0 and 10.0 keV, respectively. The reflectivity for soft X-rays is 0.28, while that for hard X-rays is a very high 0.80, which should yield much stronger modulations with depth than in the soft X-ray measurements. More quantitatively, if the X-ray reflectivity is denoted by $R_{hv}$, an approximate estimate of the total fractional modulation of the square of the standing-wave electric field intensity will be $4\sqrt{R_{hv}}$, as normalized to an incident wave field of unit strength. The bottom panels of Fig. 7 show the actual standing-wave modulation for these two energies as calculated with a program

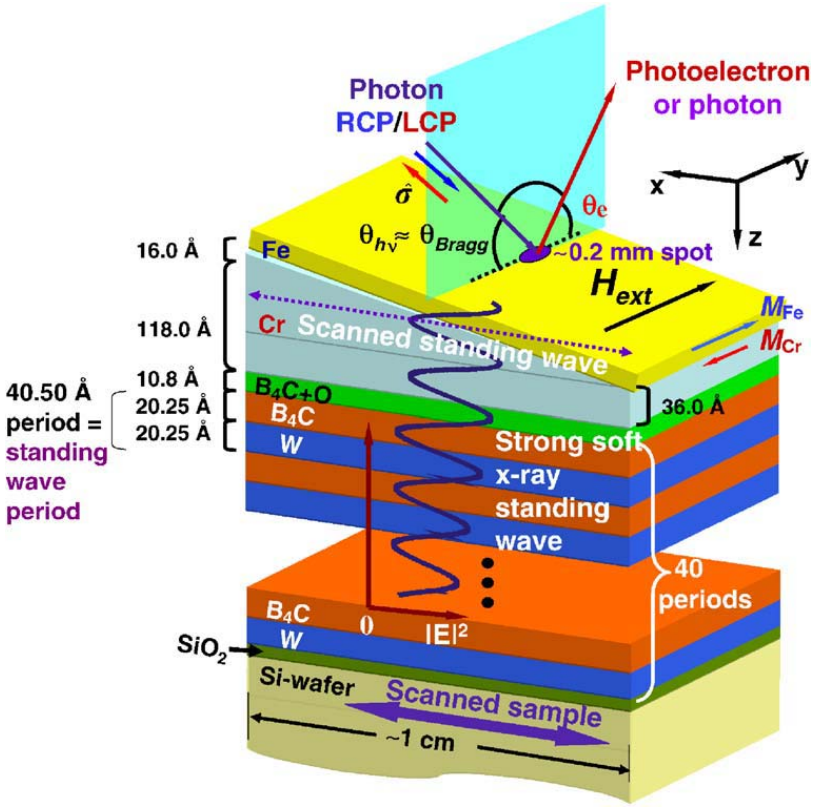


Fig. 5. Basic geometry for an experimental method that has recently been developed in the soft X-ray regime for probing buried interfaces [18]. Reflection from a multilayer mirror creates a strong standing wave above the mirror. One layer in a multilayer sample is grown in a wedge profile, permitting the scanning of the standing wave through various interfaces via the movement of the sample relative to the focused synchrotron radiation beam [18].

written by Yang [19] which includes the depth-dependent calculation of photoelectron intensities. For 1.0 keV, the overall modulation is 1.9 (compared with 2.1 from the simple $4\sqrt{R_{h\nu}}$ estimate) and for 10.0 keV it is 3.6 (compared with 3.6 from the simple estimate). For 10.0 keV, the standing wave minima are also very near zero, which should provide maximum contrast in deriving depth-dependent effects. Such studies with hard X-rays are thus most promising for the future.

## 6. Photoelectron diffraction

X-ray photoelectron diffraction (XPD) is by now a standard surface structure technique [20], so one can now ask what advantages and disadvantages would be associated with carrying it out at excitation energies of 5–15 keV. Fig. 1(a) illustrates the basic physics involved. An X-ray of polarization $\hat{\varepsilon}$ excites a photoelectron wave which propagates as a distorted spherical wave out to some scattering atom $j$ located at position $\vec{r}_j$. A scattered-wave component proportional to the scattering factor $f_j(\theta_j)$ (with $\theta_j$ the scattering angle) then interferes with the unscattered component to produce the diffraction pattern. This interaction is summed over all the atoms in a suitable cluster neighboring a given type of emitter. Inelastic scattering acts to attenuate all wave components. It is also crucial to include multiple scattering of the photoelectron, with various programs now available for calculating such patterns at up to about ~2 keV kinetic energy [21].

Of course, one immediate benefit of going to much higher energy is that the probing depth would be increased, in principle allowing for the

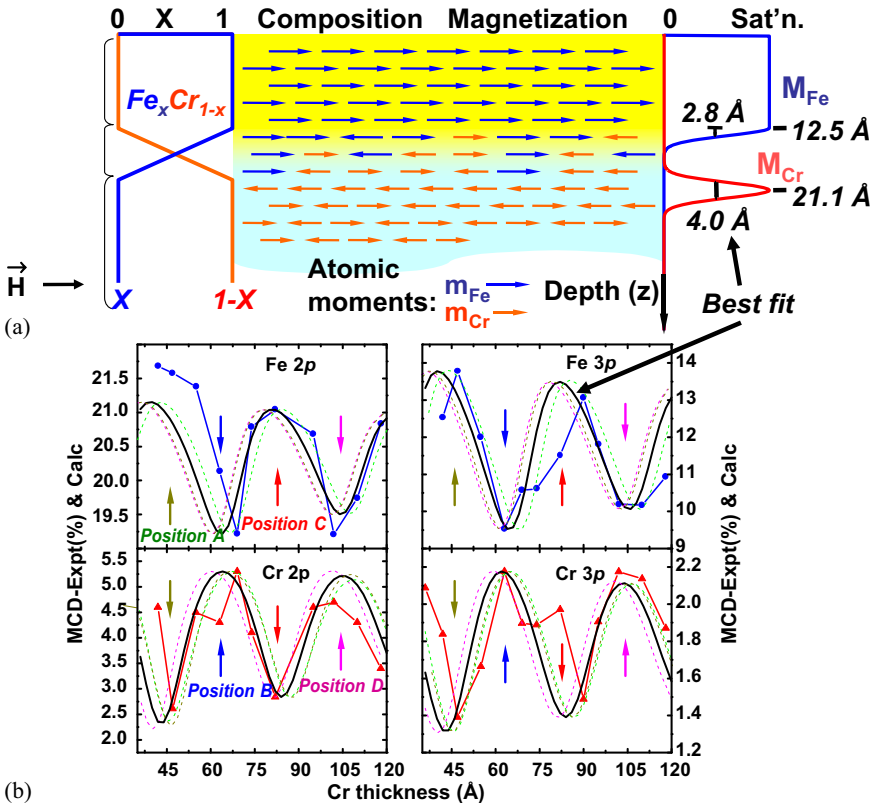


Fig. 6. Soft X-ray experimental results at 825 eV photon energy from the standing wave-wedge method introduced in Fig. 5. By fitting both rocking curve data of Fe/Cr intensity ratios (not shown) and magnetic circular dichroism (MCD) data for Fe and Cr (panel (b)), to depth-resolved X-ray optical calculations [19], the concentration and magnetization profiles through the Fe/Cr interface have been derived [18].

element-specific study of local atomic structure in the bulk of a material, including for example, that around dilute dopant species in more complex materials. But beyond this are other pluses and minuses.

Thompson and Fadley some time ago [22] carried out theoretical simulations in order to compare XPD at 1 and 10 keV, and some of their results are shown in Fig. 8. Here, the simple case of C 1s emission from a vertically oriented CO molecule, which should result in a forward scattering peak (0th order diffraction) and higher-order diffraction features, as shown in Fig. 8(a), is treated. Fig. 8(b) shows that the forward scattering peaks typical of XPD data are clear for both energies, and that the predicted anisotropies in the absence of any vibrational motion of the molecule are about the same for both energies, but the forward peak is significantly narrower at 10 keV. Thus, forward scattering diffraction features are in general expected to be sharper at higher energies. The higher-order diffraction features are, however, weaker at 10 keV. Beyond this, the total scattering cross-section falls off as the energy increases [22], and as a result, the presence of any vibrational broadening tends to quickly reduce the fractional anisotropies in diffraction patterns. Further discussions of the pros and cons of XPD at 10 keV appear in this earlier paper.

Beyond such intramolecular arguments, Fig. 1(b) illustrates another important aspect of HXPD: Bragg-like reflections from crystal planes which produce Kikuchi lines and patterns. The core photoelectron emitter acts like a point source inside the crystal, and for a given set of planes $\{h\,k\,\ell\}$ Bragg reflection can occur over two cones, at $\pm$ the Bragg angle $\theta_{hk\ell}$ with respect to the planes. Bands of enhanced and deenhanced intensity thus arise for

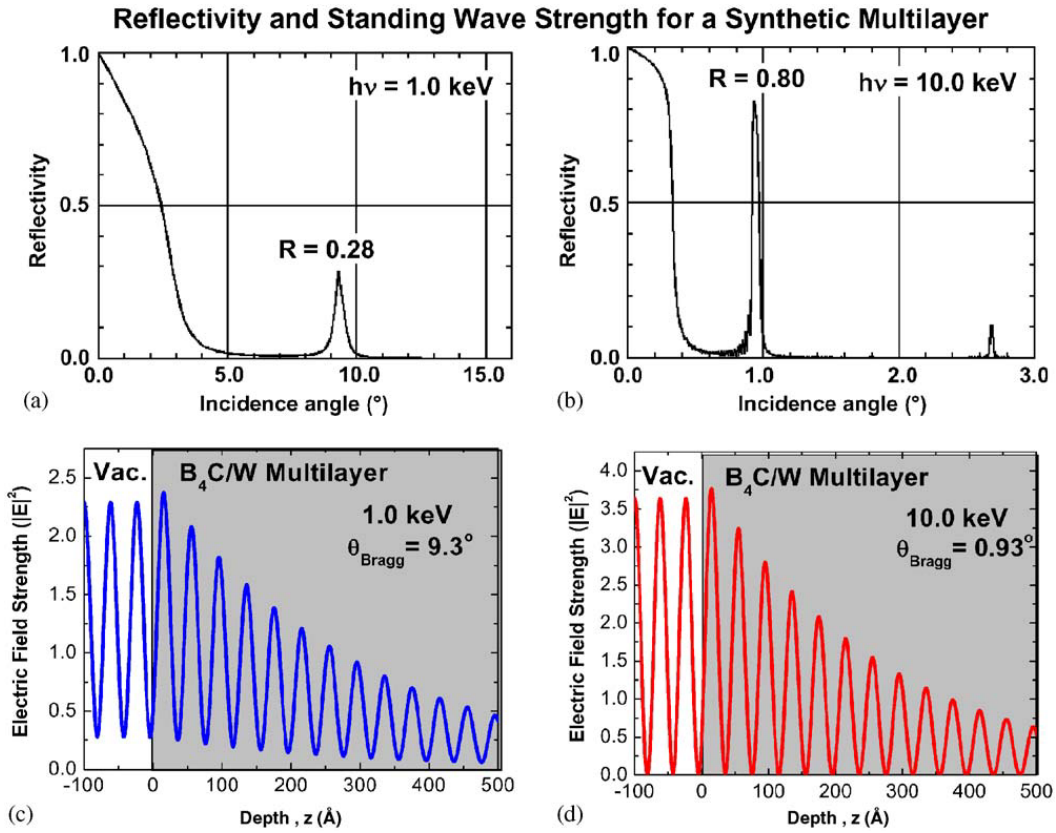


Fig. 7. Theoretical calculations comparing the reflectivity ((a) and (b)) and standing wave modulations ((c) and (d)) above a $B_4C$/W multilayer mirror consisting of 40 bilayers of [$B_4C$-20 Å/W-20 Å] for 1 and 10 keV incident radiation. Calculations in (c) and (d) are due to Yang [19].

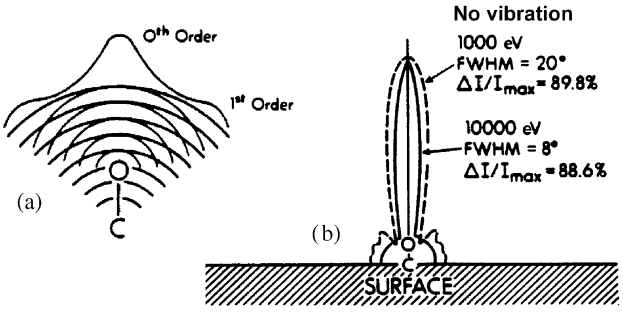


Fig. 8. (a) The fundamental process involved in photoelectron diffraction, illustrated here for C 1s emission in a vertically aligned CO molecule. (b) Comparison of the diffraction profiles expected for emission with electrons of 1000 and 10 000 eV kinetic energy, illustrating the narrowing of the forward scattering (0th order) peak, and the weakening of the higher-order features at the higher energy [22].

each set of low-index planes, with spacings of $\pm\theta_{hk\ell} = \pm\sin^{-1}(\lambda_e/2d_{hk\ell})$, as shown schematically in Fig. 9(a). Such bands are already evident in XPD measurements at about 1 keV, as shown in Figs. 10(a)–(b) based on work by Osterwalder et al. [23] Here, bands of enhanced intensity adjacent to darker side bands are clearly evident in photoemission from both diamond(1 1 1) and Si(1 1 1), with the expected narrowing based on the different lattice constants and thus planar spacings in these two materials. For comparison, we also show data of Pronin et al. [24] from Si(1 1 1) that were obtained with a standard LEED system, with an incident energy of 2 keV. It is clear that the same effects are seen in XPD as in high-energy LEED patterns, in which small inelastic scattering events act to produce the same sort of localized source of outgoing electrons in the LEED experiment as the photoemission process does in XPD. Trehan et al. [25] have also pointed out via model calculations that these Kikuchi-band effects can be described via a typical cluster-based photoelectron diffraction calculation, thus emphasizing that inelastic

scattering is not an essential element of such effects in XPD, except in the attenuation of outgoing waves. Some of their results are shown in Fig. 9(b),

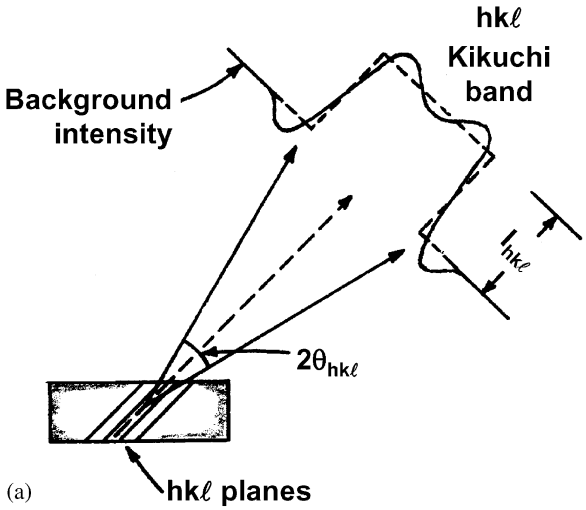


(a)

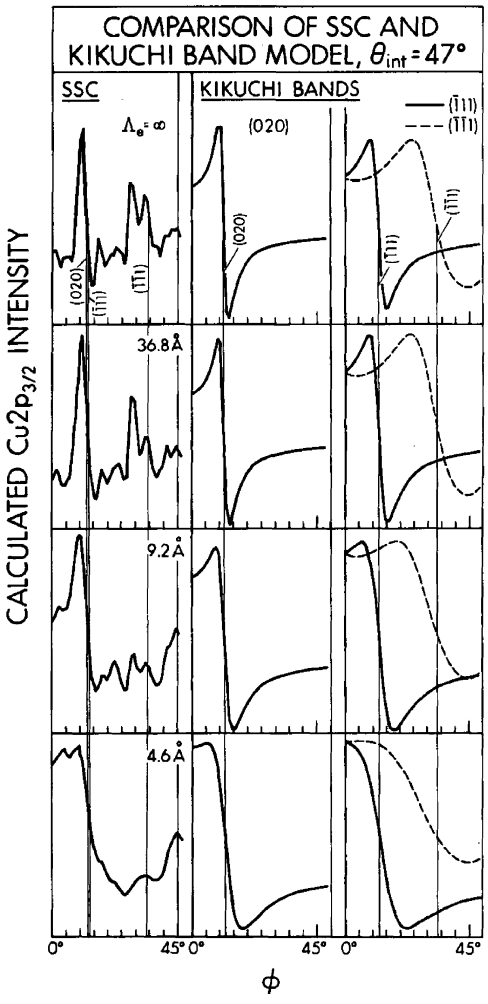


(b)

in which single-scattering cluster XPD calculations for Cu $2p_{3/2}$ emission at 555 eV kinetic energy are compared with the results of simple two-beam Kikuchi-band calculations, with different electron inelastic attenuation lengths. As the attenuation length is increased in theory, the Kikuchi-like features sharpen in both types of calculation, as expected since scattering from a greater number of planes is involved.

Thus, one expects to see even sharper, more bulk-sensitive Kikuchi-like bands in XPD from bulk samples at 5–15 keV, and these should provide element-specific information on the local atomic environments of each type of atom present. The sensitivity of such features to vibrational motion also should provide a useful element-specific measure of atomic displacements as a function of temperature. However, a final caveat regarding such measurements is in that, in order to obtain sufficient intensity for conveniently short measuring times, the electron optical system may have an acceptance angle that will average over some of the finest structure in these patterns. Compensating this somewhat is the fact that core levels will have much larger cross-sections in the hard X-ray regime than valence levels (see also discussion below), so that reducing the solid angle acceptance of the spectrometer might still be consistent with reasonable intensity.

## 7. Valence-level studies, photon momentum, phonons, and Brillouin-zone averaging

It is also well known that, on taking the photon energy up to the keV range, one can, for solids

Fig. 9. (a) Qualitative form of the Kikuchi-band profiles expected as photoelectron kinetic energy is increased. (See also Fig. 1(b)). (b) Calculations of azimuthal diffraction profiles based on two models: a single-scattering cluster (SSC) approach to XPD and a simple two-beam Kikuchi-band theory [25]. The case treated is Cu 2p emission with 1487 eV excitation from Cu(0 0 1), at a kinetic energy of 555 eV. The Kikuchi bands are separately calculated for different low-index planes. In both sets of calculations, the inelastic attenuation length $\Lambda_e$ is systematically varied, so as to illustrate the sharpening of the features for larger values of this parameter, and the equivalence of the two models.

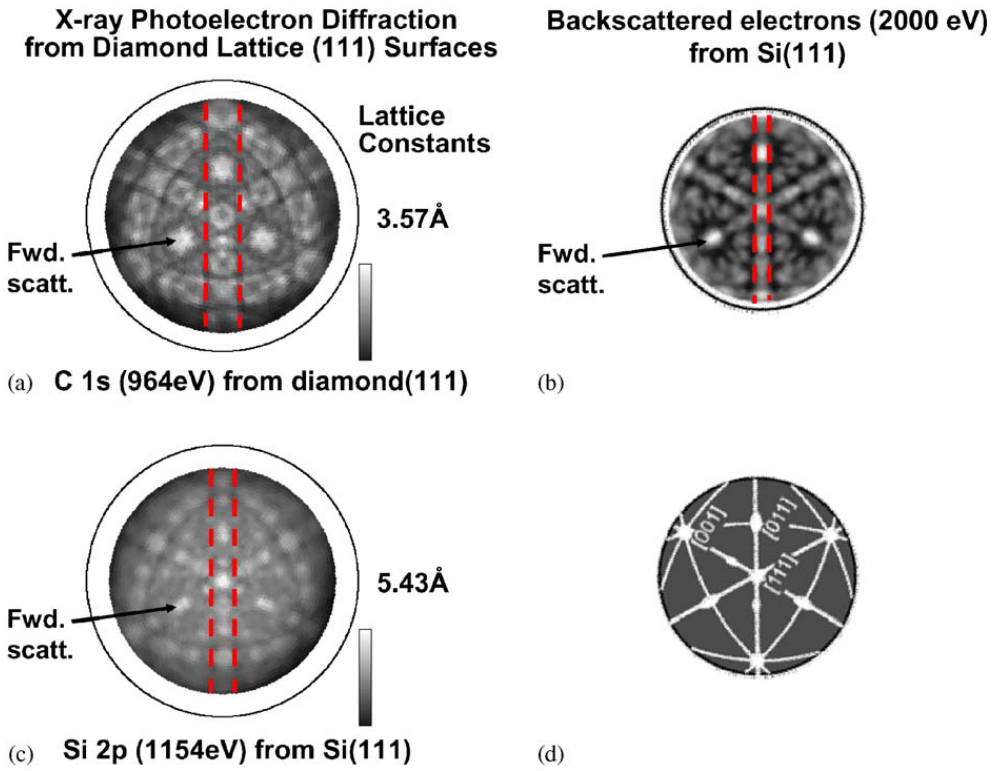


Fig. 10. Experimental XPD patterns from (a) diamond at 964 eV and (b) Si(1 1 1) at 1154 eV [23] , illustrating the presence of forward scattering features along low-index directions (shown in (d)), as well as Kikuchi-band-like features (highlighted by dashed lines), with narrowing of the latter at higher energy, as expected from Fig. 9(a). Also shown in (c) is a backscattering intensity pattern from Si(1 1 1) at 2 keV [24], with obvious close similarity.

with sufficiently high atomic vibrational amplitudes and/or at sufficiently high temperatures and/or with sufficient angular averaging reach what has been called the "XPS limit" in studying valence levels [26]. This limit implies complete averaging of the spectrum over the valence bands $E(\vec{k})$ of a solid (i.e. Brillouin-zone (BZ) averaging) so as to yield spectra that represent a matrix-element-weighted density of states (DOS). To illustrate the degree to which XPS spectra converge to the density of states, Fig. 11 shows spectra from Ag and Au obtained recently by Siegbahn [27] using monochromatized Al Kα excitation at 1.5 keV, in comparison the theoretical densities of states; the agreement here in fine structure and peak positions, even if not totally in intensity due to residual matrix element effects, is striking.

That many XPS valence spectra at ca. 1 keV excitation are in fact a mixture of the DOS-weighted XPS limit and a "UPS limit" in which wave-vector-conserving direct transitions (DTs) are important and each emission direction corresponds to sampling some region of the BZ was first discussed in detail by Hussain et al. [26], who carried out angle-resolved temperature-dependent measurements on W, a metal of sufficient vibrational rigidity that its XPS spectra at room temperature are estimated to retain roughly 50% wave-vector conserving character. To illustrate the strong influence of vibrational motion on such spectra, Fig. 12 shows spectra obtained from tungsten at two close-lying emission directions that are markedly different at room temperature due to wave-vector conservation and incomplete BZ averaging, but converge to nearly the same DOS-dominated form by 1000 K. We return below to a more quantitative consideration of such phonon-associated effects.

It is also worthwhile to consider the basic one-electron matrix elements involved in the absence of

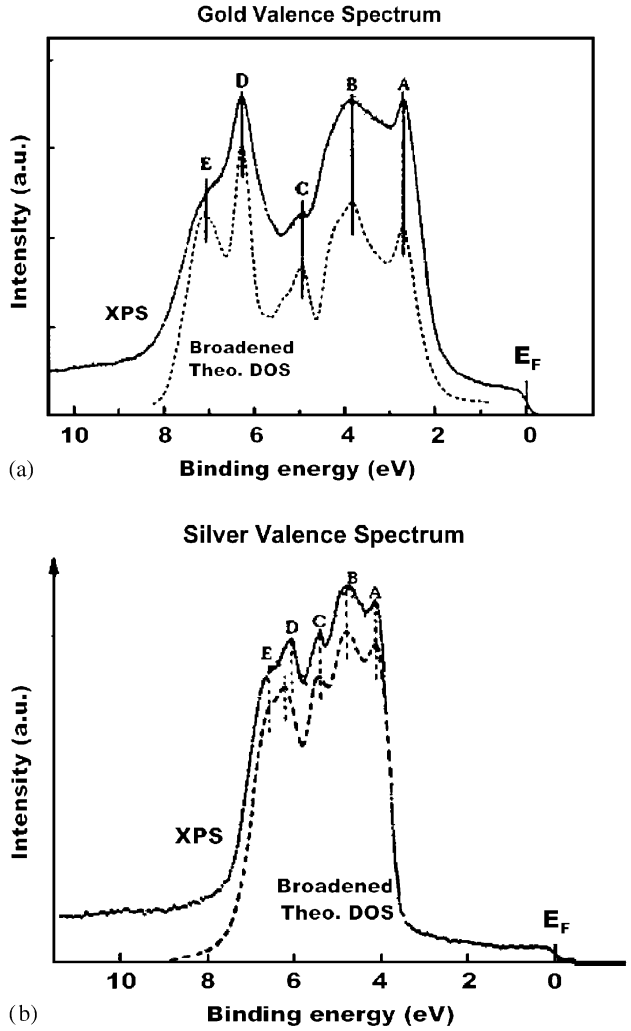


Fig. 11. Valence-band XPS spectra of Ag and Au, obtained with monochromatic X-rays at 1.5 keV by Siegbahn [27], are compared with theoretical densities of states.

any phonon contributions. From time-dependent perturbation theory and Fermi's Golden Rule, the intensity at a given final energy $E^{\mathrm{f}}$ and wave-vector $\vec{k}^{\mathrm{f}}$ resulting from an excitation at $E^{\mathrm{i}}$ and $\vec{k}^{\mathrm{i}}$ will be given by

$$I(E^{\mathrm{f}},\vec{k}^{\mathrm{f}}) \propto |\hat{\varepsilon}\cdot\langle E^{\mathrm{f}},\vec{k}^{\mathrm{f}}|e^{i\vec{k}_{hv}\cdot\vec{r}}\hat{p}|E^{\mathrm{i}},\vec{k}^{\mathrm{i}}\rangle|^2 \quad (6)$$

where $\hat{\varepsilon}$ is the polarization vector of the photon; $k_{hv}=2\pi/\lambda_{hv}$ is the wave vector associated with the photon momentum, with direction fixed by the experimental geometry; and $\hat{p}$ is the momentum operator. If $\vec{k}_{hv}$ is small with respect to the

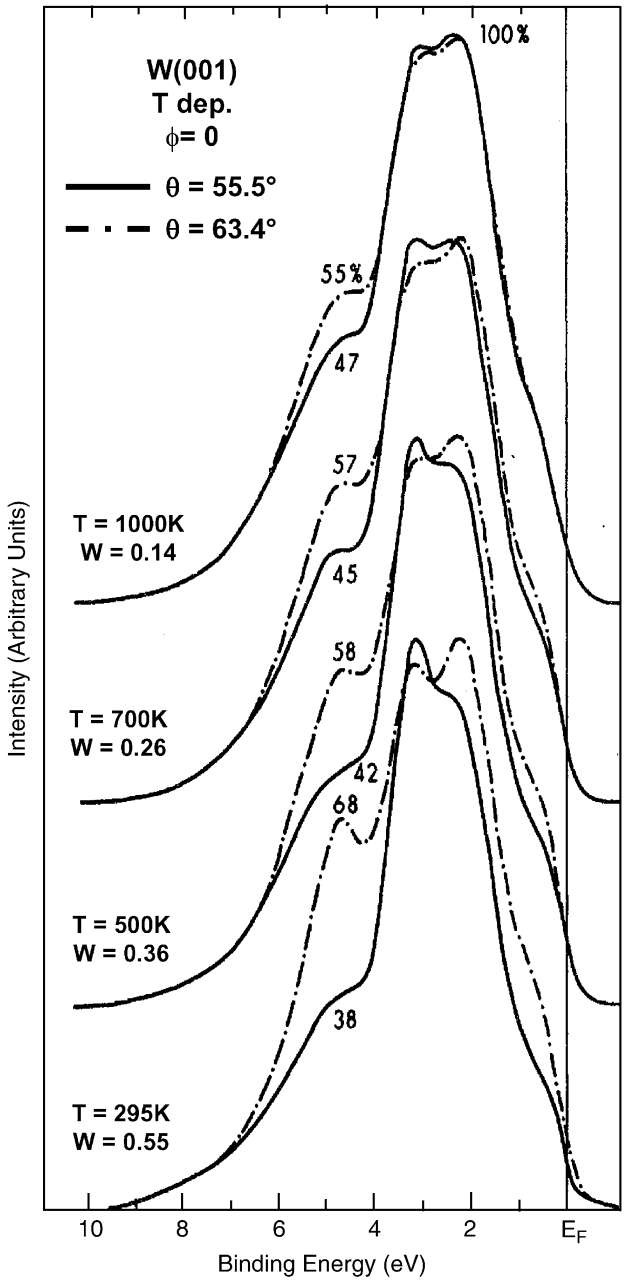


Fig. 12. Experimental illustration of the effect of phonons in producing Brillouin zone averaging in valence-band XPS [26]. With 1.5 keV excitation from W(0 0 1), two close-lying emission directions show distinct differences in their spectra at room temperature due to wave-vector-conserving (direct) transitions, but this difference systematically disappears as temperature is raised to 1000 K, and the density-of-state "XPS limit" is approached. Also shown here are the Debye–Waller factors appropriate to each temperature as a rough estimate of the fraction of transitions which are still direct.

dimensions of the BZ, which are typically $2\pi/a$ if $a$ is the lattice constant, the dipole approximation is valid, and the exponential inside the matrix element can be assumed constant over the integration. The actual matrix element can then be expressed alternatively in momentum, length, or acceleration forms. However, this approximation is not valid for photon energies of ~500 eV or more, as we now illustrate more quantitatively.

Fig. 13(a) schematically shows a typical transition in tungsten in wave-vector space with a photon energy of 1.25 keV, with the relevant wave-vector selection rule which results from Eq. (6) being

$$\vec{k}^{i} + \vec{g} + \vec{k}_{h\nu} = \vec{k}^{f}. \tag{7}$$

Here, $\vec{k}^{i}$ is the initial electron wave vector inside the BZ; $\vec{g}$ is some reciprocal lattice vector associated with the crystal; and $\vec{k}^{f} = \vec{p}^{f}/\hbar$ is the wave vector associated the final photoelectron momentum. For the specific case treated in Fig. 13(a), $\vec{g} = 10(2\pi/a)\hat{y}$, where $\hat{y}$ is a unit vector along the [0 1 0] direction, and $\vec{g}$ will always be that which finally projects $\vec{k}^{f}$ back into some $\vec{k}^{i}$ within the BZ.

As a first key point illustrated by this figure, $\vec{k}_{h\nu}$ cannot be neglected in comparison with the size of $\vec{k}^{i}$ inside the BZ, even at 1.25 keV excitation energy, and it must be allowed for in interpreting spectra. This is really no more than one consequence of being required to go beyond the dipole approximation in describing the photon-electron interaction at such high energies. The experimental effect of the photon wave vector on spectra is illustrated in Fig. 14, in which it has been found necessary to shift one set of spectra obtained in symmetry-equivalent directions above a W(0 0 1) crystal by about 6° in polar angle in order for the two sets to sample the same regions in the BZ, that is to look essentially identical in pairs. The expectation from simple theory is a shift of about 5° that is in excellent agreement with experiment. Such effects will become much more important in HXPS studies of valence bands, provided that any sort of BZ selectivity is still present, and we illustrate this in Fig. 13(b) for the same W emission geometry, but with 10 keV excitation energy. In the XPS limit of complete BZ averaging, the photon momentum will only serve to introduce non-dipole contributions to the basic matrix elements which modulate the DOS, but again, these will need to be considered.

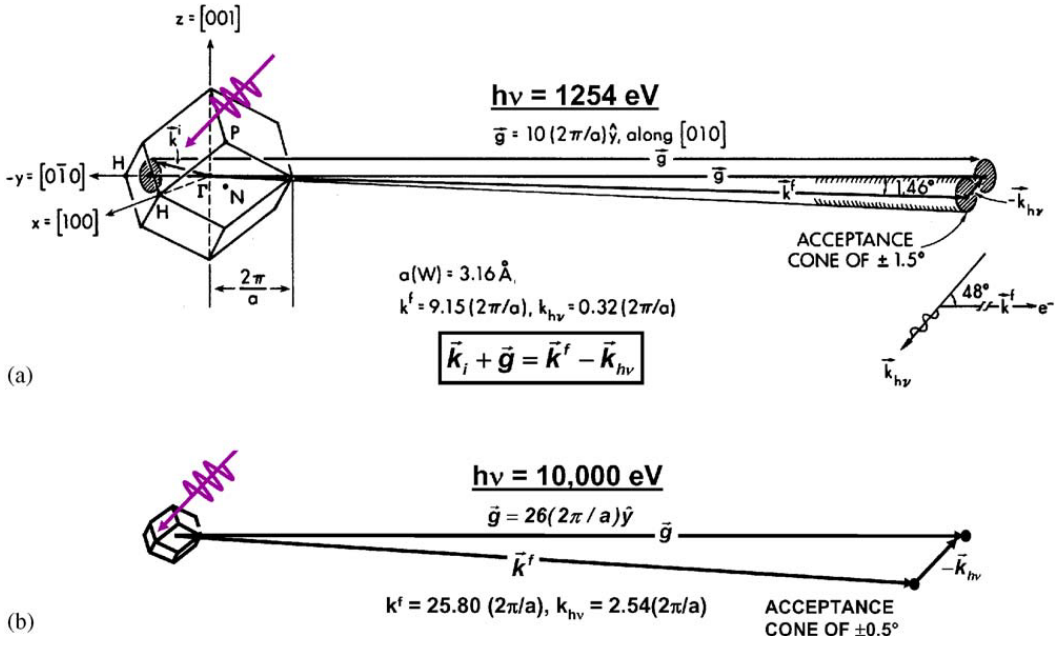


Fig. 13. Illustration of the wave-vector conservation involved in valence-band excitation from W, for (a) 1.25 keV excitation energy and (b) 10.0 keV excitation energy.

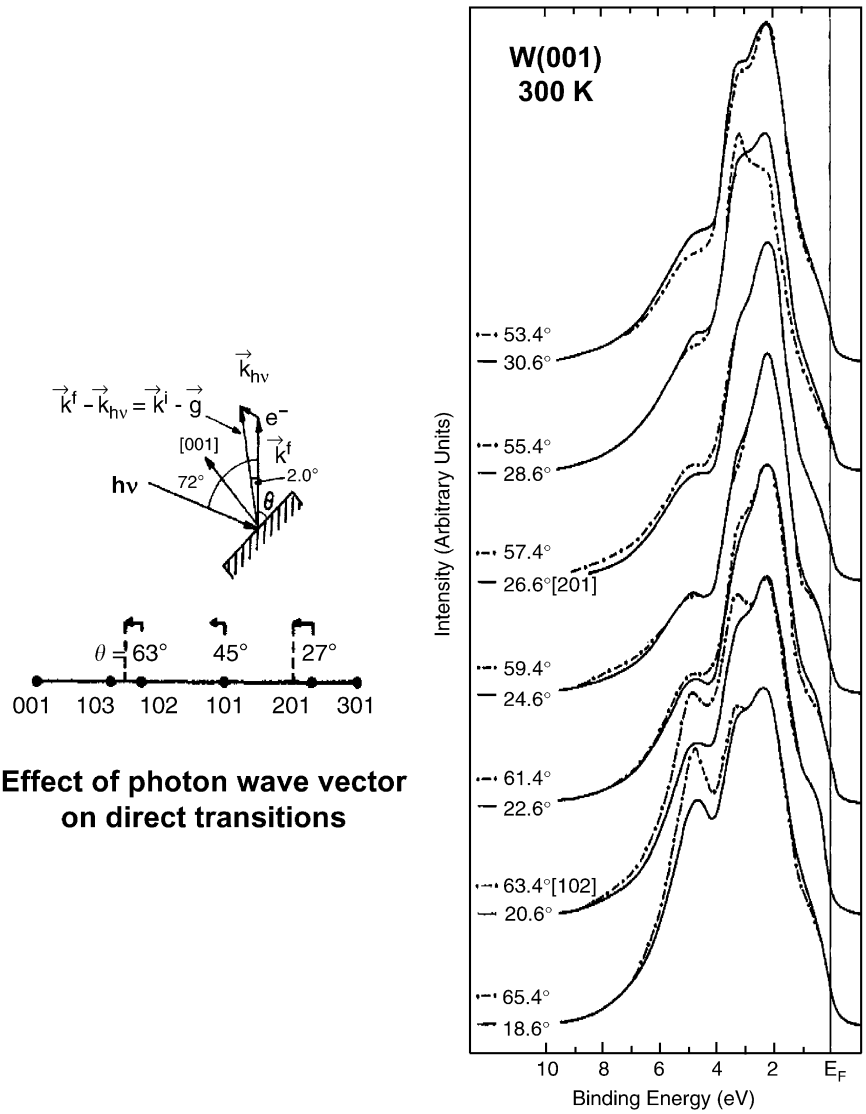


Fig. 14. Experimental verification of the importance of photon wave vector in valence-band XPS, for the case of photoemission from W(0 0 1) with 1.5 keV excitation energy [26]. The photon wave vector correction leads to a shift of about 6° in those symmetry-equivalent emission directions which sample the same region in the Brillouin zone, with the matching shifted pairs of spectra shown at right.

A second effect leading to BZ averaging is the angular acceptance of the analyzer (cf. the shaded discs in Fig. 13), which by itself smears out the set of $\vec{k}$ values sampled via direct transitions. Going to higher excitation energy will enhance this effect further, leading to a requirement of smaller solid angle acceptances if any residual direct-transition effects are to be observed.

One must also ask whether the XPS limit will always be reached in valence-band studies at 5–15 keV simply due to phonon effects. Certainly experiment must be the final test, with strong directional and temperature variations of features being qualitative indicators of residual direct transition effects, and cryogenic cooling being of likely benefit in the future in sorting such effects out. But prior studies [26] permit making approximate estimates of this, and suggest that excitation at 5–15 keV will yield rather complete BZ averaging, even before allowance is made for additional averaging effects due to angular resolution. At the most approximate level, the fraction of

transitions that remain $\vec{k}$-conserving has been estimated by computing the temperature-dependent Debye–Waller factors $W(T)$ associated with the particular $\vec{g}$ vector involved in the transition

$$W(T) = \exp\left[-\tfrac{1}{3}\langle U^2(T)\rangle\, g^2\right] \quad (8)$$

where $\langle U^2(T)\rangle$ is the three-dimensional mean-squared vibrational displacement, which can be estimated from the Debye model or other more accurate correlated models. The $W$ values obtained from such an analysis are, for example, shown in Fig. 12 for tungsten, which is expected to be among the elements with the highest retention of direct transitions at any temperature [26]. The spectra in Fig. 12 clearly show the convergence of spectral shapes for two close-lying directions as photon effects cause increased BZ averaging. Now applying this type of analysis to excitation of tungsten with 10 keV photons, for which the $\vec{g}$ vector magnitude increases to about $26(2\pi/a)$, yields estimated direct-transition retentions of only 1% at 300 K, 16% at 77 K, and 21% at 4 K. Thus, it is expected that most materials will be very close to the XPS limit when excited with 5–15 keV photons, but perhaps with some residual direct-transition effects still visible via cryogenic cooling.

More accurate models of such phonon effects in angle-resolved photoemission have also been discussed previously [28,29] and Vicente-Alvarez et al. in particular have performed numerical calculations for valence-band photoemission from Al at various photon energies from 105 to 1250 eV which clearly demonstrate the transition from direct-transition-dominated behavior to DOS behavior. Some of their results are shown in Fig. 15, where the polar angular dependence of peak intensities for three different points A, B, and C in $\vec{k}$ but at the same binding energy are plotted for three photon energies. Note the strong direct-transition peaks at 105 eV, where there is also very different behavior of the three points, and the convergence of behavior for 1250 eV. The high-energy behavior of all three $\vec{k}$ points, for which the spectra converge to DOS behavior, is furthermore simply that connected with XPD-like effects that are identical for all states at that energy.

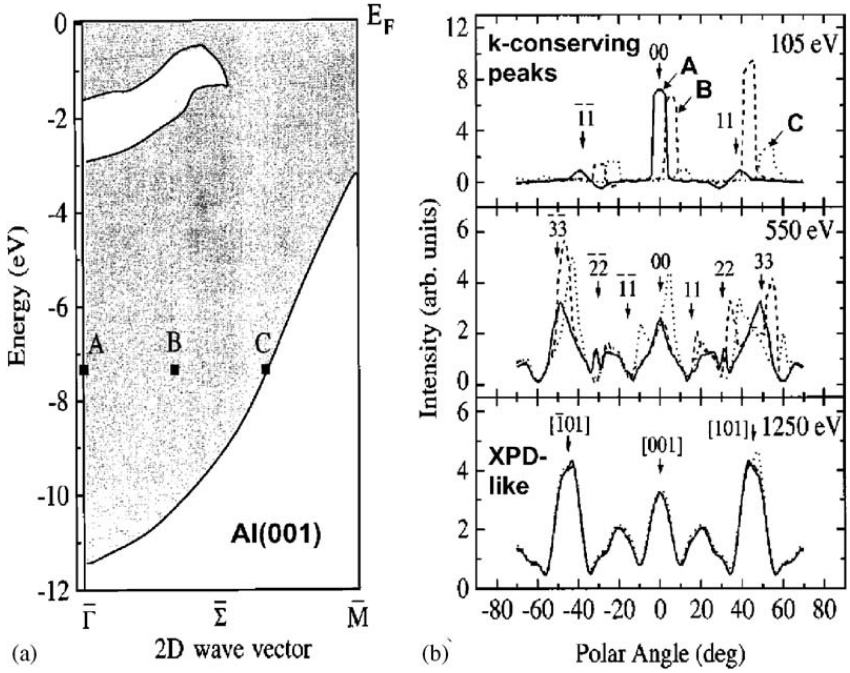


Fig. 15. Theoretical calculations of phonon effects on valence-band photoemission from Al, illustrating the gradual transition from direct-transition behavior to density-of-states behavior [29]. (a) The projected bulk bands of Al, with three $\vec{k}$ points $A$, $B$, and $C$ at the same energy $E^i$ for which calculations were carried out. (b) Azimuthal scans of intensity for emission from those $\vec{k}$ points, at photon energies of 105, 550, and 1250 eV.

These results can be compared to a parallel, and prior, experimental studies that led to what can be termed valence photoelectron diffraction (VPD)[30,31]. To illustrate the connection of this theoretical analysis with the experiment, Fig. 16 shows core and valence XPS spectra from aluminum obtained by Osterwalder et al. [30], together with an azimuthal scan of the energy-integrated VB intensity and the Al 2s core intensity. Both VB and core intensities exhibit essentially the same angular distribution, which is describable in terms of XPD. Similar results have also been found by Herman et al. [31] for Ge valence and core spectra in XPS.

No calculations of vibrational effects on XPS valence spectra at the level of accuracy of those of Vicente-Alvarez et al. have been carried out for other elements or for energies as high as 5–15 keV, but further analyses of this type would certainly be very desirable. One expectation would nonetheless be that, once the XPS limit is reached, the integrated valence-band intensities, or even intensities at a fixed binding energy in a spectrum (cf. Fig. 15) would exhibit HXPD effects such as those discussed in Section 6: forward scattering peaks along low-index directions and Kikuchi bands.

Finally, we consider the nature of the matrix elements in Eq. 6, in terms of the region in space that is primarily involved, as discussed also by Solterbeck et al. [32] In general, because of the high energy of the photoelectron, its oscillations in space, with wavelength $\lambda^f = 2\pi/k^f$, which is only about 0.10–0.15 Å for 5000–10,000 eV energies, are very short in scale relative to those of outer valence electronic states. Thus, there tends to be a net cancellation in matrix element contributions from the positive and negative portions of the photoelectron wave that are multiplied by the much more slowly varying valence wave function. This is the reason core levels, which oscillate much more rapidly in radius, maintain larger cross-sections as photon energy increases. A further implication of this kind of argument for valence band studies is that HXPS spectra should be much more sensitive to those portions of valence electron wave functions that are nearest the nucleus, as discussed by Woicik in another article in this volume [17].

In summary, from prior XPS work on valence levels, it seems likely that HXPS in the 5–15 keV

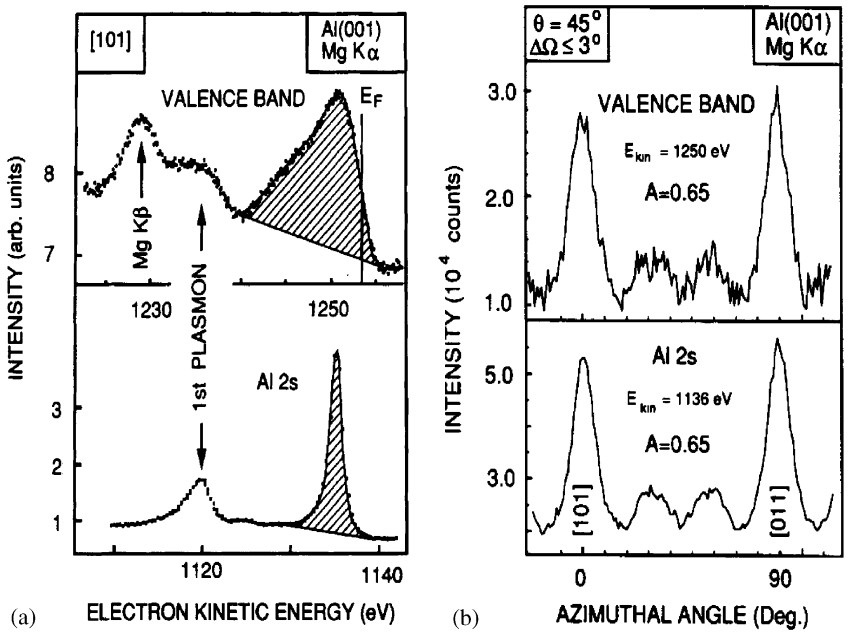


Fig. 16. Azimuthal-scan experimental data for valence-band and core photoemission from Al [30]: Valence-band (a) and core Al 2s (b) spectra, and the azimuthal dependence of the energy-integrated valence-band intensity (c) and the core intensity (d).

range will for many, if not most, cases yield spectra in the XPS limit of zone-averaged densities-of-states with matrix element modulation. Variable-temperature studies going to the lowest possible temperatures, as well as more accurate theoretical modeling, would certainly be of interest in sorting out the phonon contributions to zone averaging. Beyond this, analyzer angular acceptance, also leading to zone averaging, represents another major factor which would be difficult to avoid without reducing intensities too much for practical spectroscopy. Finally, non-dipole effects need to be considered, both via the contribution of the photon wave vector to the conservation equation and other more subtle factors in the matrix elements themselves. Even if all such data is found to be in the XPS limit however, such density-of-states information should be extremely useful, especially in view of the greater bulk sensitivity at these higher energies. Beyond this, single crystal or multilayer standing wave effects such as those discussed in Section 5 should be most interesting in deriving element-specific contributions to the valence electronic structure [17], as well as the variation with depth of densities of states, e.g. through multilayer structures.

## 8. Concluding remarks

By suitable instrumentation improvements in SR sources, electron optical systems, and detectors, HXPS in the 5–15 keV regime has now become a feasible experiment, including both core and valence-level measurements.

Going to such high excitation energies permits measurements that are much more bulk in nature, with mean excitation depths in the 50–100 Å range. The necessity for careful surface preparation is thus much reduced, but not completely eliminated for more sensitive materials.

Varying the degree of surface sensitivity by changing the electron takeoff angle should be more easily quantifiable than at lower energies, due to more forward peaked elastic electron scattering and the reduced influence of the inner potential at the surface.

Using grazing X-ray incidence, at or somewhat above the onset of total reflection should be of use in reducing the inelastic backgrounds underneath spectra.

X-ray standing waves, created by Bragg reflection from either crystal planes or synthetic multilayer mirrors, constitute a very powerful position-resolved probe of element-specific densities of states [17], or composition and magnetization near buried interfaces.

Core-level angular distributions above single-crystal samples will exhibit photoelectron diffraction effects, including both a sharpening of forward scattering features and the presence of Kikuchi-band fine structure due to Bragg reflection of photoelectrons from crystal planes. These effects should provide element-specific local structure information, provided that the solid angle of acceptance of the spectrometer can be reduced sufficiently to see them clearly.

Valence-level studies at such high excitation energies will tend toward the ''XPS limit'' for which initial states over the entire BZ are sampled, and spectra are matrix-element-modulated densities of states. This is due to a combination of phonon effects and the angular acceptance of the spectrometer. The photon momentum and other non-dipole effects in matrix elements will need to be considered in analyzing such data. Nonetheless, much useful information on bulk densities of states should be derivable.

## References

[1] K. Siegbahn, et al., ESCA-Atomic, Molecular, and Solid-State Structure Studied by Means of Electron Spectroscopy, Almqvist and Wiksells AB, Stockholm, 1967 (and earlier papers cited therein).
[2] P. Pianetta, I. Lindau, Nature 250 (1974) 214.
[3] C. Dallera, L. Duo, L. Braicovich, G. Panaccione, G. Paolicelli, B. Cowie, J. Zegenhagen, Appl. Phys. Lett. 85 (2004) 4532;
P. Torelli, et al., Rev. Sci. Inst. 76 (2005) 023909 (and other articles in this issue).
[4] S.B.M. Hagstrom, C.S. Fadley, in: L. Azaroff (Ed.), X-ray Spectroscopy, McGraw-Hill Publishing Co., New York, 1974 (Chapter 8, including a detailed discussion of the interplay of retardation, resolution, and intensity);
C.S. Fadley, in: C.R. Brundle, A.D. Baker (Eds.), Electron

Spectroscopy: Theory, Techniques, and Applications, vol. II, Academic Press, London, 1978 (Chapter 1).
[5] (a) A. Jablonski, C.J. Powell, J. Vac. Sci. Tech. A 21 (2003) 274 and earlier references therein; (b) C.J. Powell, Private communication.
[6] (a) S.T. Manson, Private Communication; (b) J.H. Scofield, Lawrence Livermore Laboratory Report UCRL-51326 (1973), also available for download at http://electron.lbl.gov/software/software.html
[7] M.B. Trzhaskovskaya, V.I. Nefedov, V.G. Yarzhemsky, Atom. Data Nucl. Data Tables 82 (2002) 257.
[8] J.-M. Bussat, C.S. Fadley, Z. Hussain, A.W. Kay, G. Lebedev, B.A. Ludewigt, G. Meddeler, A. Nambu, M. Press, H. Spieler, B. Turko, M. West, G. Zizka, AIP Conf. Proc. 705 (2004) 945.
[9] S. Tanuma, C.J. Powell, D.R. Penn, Surf. Interf. Anal. 21 (1994) 165;
S. Tanuma, C.J. Powell, D.R. Penn, Surf. Interf. Anal. 35 (2003) 268 (results of the TPP-2M model extrapolated to higher energies as $E_{\mathrm{kin}}^{0.75}$).
[10] W.S.M. Werner, L. Kover, J. Toth, D. Varga, J. Electron. Spectrosc. 122 (2002) 103
C.J. Powell, W.S.M. Werner, Private communication.
[11] C.S. Fadley, in: S. Davison (Ed.), Progress in Surface Science, vol. 16, Pergamon Press, New York, 1984 p. 275.
[12] B.L. Henke, Phys. Rev. A 6 (1972) 94.
[13] J. Kawai, M. Takami, M. Fujinami, Y. Hashiguchi, S. Hayakawa, Y. Gohshi, Spectrochim. Acta B 47 (1992) 983;
M.J. Chester, T. Jach, Phys. Rev. B 48 (1993) 17262;
T. Jach, E. Landree, Surf. Interf. Anal. 31 (2001) 768.
[14] Y. Iijima, K. Miyoshi, S. Saito, Surf. Interf. Anal. 27 (1999) 35È42.
[15] Center for X-Ray Optics, Lawrence Berkeley National Laboratory, website http://www.cxro.lbl.gov/optical_constants/
[16] C.-Y. Kim, M.J. Bedzyk, E.J. Nelson, J.C. Woicik, L.E. Berman, Phys. Rev. B 66 (2002) 85115;
J.C. Woicik, E.J. Nelson, L. Kronik, M. Jain, J.R. Chelikowsky, D. Heskett, L.E. Berman, G.S. Herman, Phys. Rev. Lett. 89 (2002) 077401.
[17] J. Woicik, Nucl. Instr. and Meth. A, this volume.
[18] S.-H. Yang, B.S. Mun, A.W. Kay, S.-K. Kim, J.B. Kortright, J.H. Underwood, Z. Hussain, C.S. Fadley, Surf. Sci. Lett. 461 (2000) L557;
S.-H. Yang, B.S. Mun, N. Mannella, S.-K. Kim, J.B. Kortright, J. Underwood, F. Salmassi, E. Arenholz, A. Young, Z. Hussain, M.A. Van Hove, C.S. Fadley, J. Phys. Condens. Matter 14 (2002) L406.
[19] S.-H. Yang, Computer program for simulating standing-wave excited spectroscopy, to be published.
[20] C.S. Fadley, in: R.Z. Bachrach (Ed.), Chapter in Synchrotron Radiation Research: Advances in Surface and Interface Science, Plenum Press, New York, 1992.
[21] Two X-ray photoelectron diffraction programs are available for online usage or as freeware at: http://electron.lbl.gov/~edac/ or http://electron.lbl.gov/mscdpack/mscdpack.html. These are limited to about 2 keV in maximum energy, however.
[22] K.A. Thompson, C.S. Fadley, J. Electron. Spectrosc. 33 (1984) 29.
[23] J. Osterwalder, R. Fasel, A. Stuck, P. Aebi, L. Schlapbach, J. Electron. Spectrosc. 68 (1994) 1.
[24] I.I. Pronin, D.A. Valdaitsev, N.S. Faradzhev, M.A. Gomoyunova, P. Luches, S. Valeri, Appl. Surf. Sci. 175 (2001) 83.
[25] R. Trehan, J. Osterwalder, C.S. Fadley, J. Electron. Spectrosc. 42 (1987) 187.
[26] Z. Hussain, S. Kono, C.S. Fadley, Phys. Rev. 22 (1980) 3750.
[27] K. Siegbahn, J. Electron. Spectrosc. 137–140 (2004) 3.
[28] R.C. White, C.S. Fadley, M. Sagurton, P. Roubin, D. Chandesris, J. Lecante, C. Guillot, Z. Hussain, Phys. Rev. B 35 (1987) 1147.
[29] M.A. Vicente Alvarez, H. Ascolani, G. Zampieri, Phys. Rev. B 54 (1996) 14703.
[30] J. Osterwalder, T. Greber, S. Hüfner, L. Schlapbach, Phys. Rev. Lett. 64 (1990) 2683.
[31] G.S. Herman, T.T. Tran, K. Higashiyama, C.S. Fadley, Phys. Rev. Lett. 68 (1992) 1204.
[32] C. Solterbeck, W. Schattke, J.-W. Zahlmann-Nowitzki, K.-U. Gawlik, L. Kipp, M. Skibowski, C.S. Fadley, M.A. Van Hove, Phys. Rev. Lett. 79 (1997) 4681.